Pacific Northwest National Laboratory

Operated by Battelle for the U.S. Department of Energy

Annual Report 1996

Chemical Structure and Dynamics

William R. Wiley

Environmental Molecular Sciences Laboratory

PACIFIC NORTHWEST NATIONAL LABORATORY
operated by
BATTELLE
for the
UNITED STATES DEPARTMENT OF ENERGY
under Contract DE-AC06-76RLO 1830

Printed in the United States of America

Available to DOE and DOE contractors from the Office of Scientific and Technical Information, P.O. Box 62, Oak Ridge, TN 37831; prices available from (615) 576-8401.

Available to the public from the National Technical Information Service, U.S. Department of Commerce, 5285 Port Royal Rd., Springfield, VA 22161

PNNL-11537
UC-400

Annual Report 1996
Chemical Structure and Dynamics

Prepared by
Steven D. Colson, Associate Director
Robin S. McDowell, Program Manager
and the Staff of the Chemical Structure and Dynamics Program

March 1997

Prepared for the U.S. Department of Energy
under Contract DE-AC06-76RLO 1830

Pacific Northwest National Laboratory
Operated for the U.S. Department of Energy
by Battelle Memorial Institute

Contents

1. Introduction 1-1

2. Reaction Mechanisms at Interfaces

Experimental and Theoretical Study of Oxyanion Chemistry on Mineral Surfaces[a]
S. A. Joyce, B. J. Roop, M. A. Henderson, and J. R. Rustad 2-1

Structure and Energetics of the Water/NaCl (100) Interface[b]
D. P. Taylor, W. P. Hess, and M. I. McCarthy 2-3

Molecular Beam–Surface Scattering and Kinetics Instrumentation[b,c]
G. A. Kimmel, M. A. Covert, S. E. Barlow, R. S. Smith, and B. D. Kay 2-6

Kinetic Processes in Nanoscale Films of Amorphous Solid Water[b]
R. S. Smith, C. Huang, and B. D. Kay 2-9

Chemisorption on Oxide Surfaces[b]
M. J. Stirniman, C. Huang, R. S. Smith, S. A. Joyce, and B. D. Kay 2-14

Synthetic Ionic Interfaces via Ion-Beam and Ice Epitaxy[b]
A. A. Tsekouras, G. B. Ellison, J. P. Cowin, and M. J. Iedema 2-19

Transport of Molecules across the Liquid/Vapor Interface of Water[b,c]
D. S. Karpovich, A. G. Joly, G. R. Holtom, J. L. Daschbach, and D. Ray 2-21

Single-Molecule Spectroscopy and Dynamics at Room Temperature[b]
H. P. Lu, J. D. Chesko, and X. S. Xie 2-22

Single-Molecule Studies of Flavoenzymes[a]
X. S. Xie, H. P. Lu, and L. Xun 2-24

Nonlinear Optical Imaging[d]
E. D. Sanchez, L. Novotny, G. R. Holtom, and X. S. Xie 2-26

3. Radiation and Other High-Energy Processes at Environmental Interfaces

Photostimulated Desorption of CO from Geologic Calcite Following 193-nm Irradiation[b,e]
K. M. Beck, D. P. Taylor, and W. P. Hess 3-1

Mass Spectrometry of Low-Molecular-Weight Solids by Matrix-Assisted Laser Desorption/Ionization[b,e]
S. C. Goheen, K. L. Wahl, J. A. Campbell, and W. P. Hess 3-3

Infrared Polarization Study of the Ultraviolet Photolysis of Condensed-Phase Acetyl Chloride[b]
B. Rowland and W. P. Hess 3-7

Plasma and Materials Chemistry Approach to Treatment of Automotive Exhaust[d]
R. G. Tonkyn, S. E. Barlow, M. L. Balmer, D. Goulette, and T. M. Orlando 3-9

Mechanisms of Radiolytic Decomposition of Complex Nuclear Waste Forms[a]
T. M. Orlando, K. D. Keefer, K. Knutsen, N. Petrick, Y. Su, and D. P. Taylor 3-11

Mechanistic Studies of Radiation (Low-Energy Electron) Damage of $NaNO_3$ Surfaces and Interfaces[f]
K. Knutsen, D. M. Camaioni, and T. M. Orlando 3-12

Decomposition of Hexafluoroethane in a Packed-Bed Corona Reactor[g]
W. O. Heath and R. G. Tonkyn 3-13

Nonthermal Interfacial Processes: Electron- and Photon-Stimulated Desorption, Dissociation, and Surface/Interface Chemistry[b]
T. M. Orlando, M. T. Sieger, W. C. Simpson, R. G. Tonkyn, and G. A. Kimmel 3-15

Photon-Stimulated Desorption of O (^3P) and NO ($^2\Pi$) from $NaNO_3$ Single Crystals[b]
K. Knutsen and T. M. Orlando 3-18

4. Cluster Models of the Condensed Phase

Cluster Model Studies of the Structure and Bonding of Environmentally-Important Materials[b]
L. S. Wang, J. B. Nicholas, S. D. Colson, S. R. Desai, H. Wu, S. Li, and C. M. Rohlfing 4-1

Photoelectron Spectroscopy and Electronic Structure of Metal Clusters and Chemisorbed Metal Cluster Complexes[h]
L. S. Wang, H. Wu, C. F. Ding, and X. Li 4-3

Study of Transition-Metal–Carbon Mixed Clusters[h]
L. S. Wang, S. Li, C. F. Ding, and X. Li 4-5

High-Resolution IR Spectroscopy of Molecules and Clusters[b,c]
S. W. Sharpe, T. A. Blake, R. L. Sams, and R. S. McDowell 4-7

Spectroscopy and Dynamics of Clusters[b]
A. G. Joly and D. Ray 4-8

Intrinsic Affinity and Selectivity of Crown Ethers for Alkali-Metal Cations[b,h]
M. B. More, P. B. Armentrout, and D. Ray 4-9

5. Miscellaneous

Near-Infrared Spectroscopy for Trace Atmospheric Monitoring[b,c]
S. W. Sharpe, T. A. Blake, and R. L. Sams 5-1

Laser-Based Detection of Chemical Contraband[i]
S. W. Sharpe, R. G. Clemmer, J. F. Kelly, S. W. Martin, and G. M. Mong 5-1

Disease Diagnosis and Laser-Based Breath Analysis[a]
S. W. Sharpe, J. J. Toth, R. L. Sams, and K. D. Thrall 5-3

Asymmetric RF Ion Trap and Simultaneous Anion/Cation Detection[b]
S. E. Barlow, M. L. Alexander, and J. C. Follansbee 5-6

Near-Field Optical Tweezers[a]
L. Novotny, R. X. Bian, and X. S. Xie 5-10

6. Appendix

Chemical Structure and Dynamics Staff 6-1
Publications and Presentations
- Publications 6-5
- In Press and Submitted 6-7
- Patents 6-8
- Presentations 6-9

Awards and Recognition 6-15
Collaborations
- External Collaborations 6-16
- Collaborations within PNNL 6-17

Acronyms and Abbreviations 6-19
Where CS&D Fits in PNNL 6-20

Funding Support

[a] Pacific Northwest National Laboratory (PNNL) Laboratory Directed Research and Development (LDRD).
[b] DOE Office of Basic Energy Sciences, Chemical Sciences Division, Fundamental Interactions Branch.
[c] Instrument development under the Environmental Molecular Sciences Laboratory (EMSL) Project.
[d] Cooperative Research and Development Agreement (CRADA).
[e] Strategic Environmental Research and Development Program (SERDP).
[f] DOE Environmental Management Science Program (EMSP).
[g] Battelle Memorial Institute Institutional Research and Development funds.
[h] National Science Foundation.
[i] PNNL National Security Directorate.

1. Introduction

Purpose

The Chemical Structure and Dynamics (CS&D) program is a major component of the William R. Wiley Environmental Molecular Sciences Laboratory (EMSL) developed by Pacific Northwest National Laboratory (PNNL) to provide a state-of-the-art collaborative facility for studies of chemical structure and dynamics. We respond to the need for a fundamental, molecular-level understanding of chemistry at a wide variety of environmentally important interfaces by (1) extending the experimental characterization and theoretical description of chemical reactions to encompass the effects of condensed media and interfaces; (2) developing a multidisciplinary capability for describing interfacial chemical processes within which the new knowledge generated can be brought to bear on complex phenomena in environmental chemistry and in nuclear waste processing and storage; and (3) developing state-of-the-art analytical methods for characterizing waste tanks and pollutant distributions, and for detecting and monitoring trace atmospheric species.

This research effort was initiated in 1989 and will continue to evolve over the next few years into a program of rigorous studies of fundamental molecular processes in model systems, such as well-characterized surfaces, single-component solutions, clusters, and biological molecules; and studies of complex systems found in the environment (multispecies, multiphase solutions; solid/liquid, liquid/liquid, and gas/surface interfaces; colloidal dispersions; ultrafine aerosols; and functioning biological systems).

The success of this program will result in achieving a quantitative understanding of chemical reactions at interfaces and, more generally, in condensed media, comparable to that currently available for gas-phase reactions. This understanding will form the basis for the development of *a priori* theories for predicting macroscopic chemical behavior in condensed and heterogeneous media, which will add significantly to the value of field-scale environmental models, predictions of short- and long-term nuclear waste storage stabilities, and other areas related to the primary missions of the United States Department of Energy (DOE).

CS&D has developed research programs in the following areas:

Chemical structures, reaction dynamics, and kinetics in solution and at interfaces, to support DOE needs for
- — characterization, processing, and storage of mixed wastes
- — remediation of contaminated soils and groundwater
- — understanding global change
- — ensuring nuclear nonproliferation.

Structure/function research on molecular systems, especially on problems associated with
- — surface chemistry and catalysis
- — bioremediation
- — high-energy processes.

Establishment and operation of a portion of EMSL for the study of
- — surface/interface structure and reactions
- — chemical structure and reaction dynamics (clusters, reactive species, and model systems)
- — time-resolved spectroscopy.

Development of state-of-the-art analytical methods for characterizing tanks and plumes, and for detecting and monitoring trace atmospheric species.

Background

Studies of the surface chemistry at interfaces requires measurements of many chemical and physical properties within 5 to 10 Å of the interface boundary. An understanding of the interfacial chemistry can be achieved only by combining measured quantities, such as chemical dynamics, structure, and bonding, with theoretical analysis, to produce models consistent with the observations. This interdisciplinary approach is the heart of the EMSL concept, in which a wide variety of experimental and theoretical approaches are combined to address complex problems of importance to DOE.

We have targeted condensed-phase phenomena that are relevant to chemical processes in natural and contaminated systems, including those related specifically to environmental restoration and

waste storage issues at DOE sites. For example, systems have been selected to model the sorption and abiotic transformations of solutes on mineral surfaces in soil and groundwater. Sorption and surface-catalyzed abiotic transformations are widely recognized contributors to the natural filtration capacity of soil and porous aquifers for contaminants, and are therefore of central importance in governing contaminant transport rates and persistence. Mechanistically valid models of such phenomena at the microscopic and macroscopic scales are critically needed to predict contaminant migration on DOE sites, but are unavailable because the responsible surface chemical reactions are not completely understood.

Chemical reactivity at environmental solid–liquid interfaces is controlled by the effects of substrate structure on the interactions between solvent and adsorbate solute molecules. To observe chemical changes at these interfaces, experimental methods are needed to measure the changes in molecular structure and dynamics that are induced by natural and man-made surfaces. Reactions and thermodynamic properties that are enhanced at environmental interfaces include: (1) proton transfer reactions, such as solute hydrolysis and acid dissociation; (2) electron transfer transformations; and (3) stability constants for adsorbate-substrate complexes. These interfacial phenomena strongly impact contaminant dynamics in soil and groundwater. However, the responsible molecular phenomena are not well understood, thereby precluding development of rigorous descriptive models. We anticipate that targeted experiments, relevant to DOE sites, on model systems containing oxides, carbonates, and silicates in contact with solvent and solute molecules can resolve much of the scientific ambiguity regarding interfacial reactions in geochemical systems. Such studies of interfacial chemistry will also have obvious and perhaps far-reaching consequences for understanding processes that affect waste chemistry and waste-form integrity when combined with the specific studies of energetic reaction mechanisms contained in the scope of this work.

A quantitative understanding of chemical reaction dynamics at interfaces in condensed media is an important goal for chemical physics research, and a challenging and demanding scientific problem requiring an understanding of the solid substrate, the solvent, and their combined effect upon the chemical reaction dynamics. It is now possible to bring together diverse expertise and technology to study complex interfacial chemistry. Such a study requires integration of state-of-the-science experimental capabilities for studying primary chemical processes with advances in computational technology and sophisticated new theoretical models for predicting molecular structure and potential energy surfaces. Essential for the success of this program is the creation of a stimulating and interactive intellectual environment, where concepts and ideas from theoretical and experimental disciplines can be integrated to produce a comprehensive approach to the study of complex phenomena. The EMSL organization and laboratory structure are designed to provide the development of this environment through internal and external collaborations.

The CS&D group has particular expertise in the preparation and spectroscopic analysis of molecular clusters (S. D. Colson, D. Ray, S. W. Sharpe, and L. S. Wang); ultrafast and nonlinear optical spectroscopies (D. Ray, G. R. Holtom, and X. Xie); ultrahigh resolution spectroscopy for measurements of electronic and geometric structures and dynamics (S. W. Sharpe and R. S. McDowell); surface and interface structure, chemical reaction dynamics, and kinetics (J. P. Cowin, W. P. Hess, S. A. Joyce, B. D. Kay, and T. M. Orlando); and ion-molecule traps and storage technology (S. E. Barlow).

Approach

Experimental studies of molecular and supramolecular structures and thermodynamics are key to understanding the nature of matter, and lead to direct comparison with computational results. Kinetic and mechanistic measurements, combined with real-time dynamics measurements of atomic and molecular motions during chemical reactions, provide a molecular-level description of reaction processes. The anticipated results of this work are the achievement of a quantitative understanding of chemical processes at complex interfaces, the development of new techniques for the detection and measurement of species at such interfaces, and the interpretation and extrapolation of the observations in terms of models of interfacial chemistry.

Our methodology dissects complex interfacial problems into components that are subject to quantitative investigation and interpretation. Target solvent–reactant-surface systems have been selected for study because of their theoretical interest and applicability to DOE's environmental problems. The theoretical basis for understanding such systems starts with the literature data base, augmented by new measurements on synthetic interfaces of controlled composition and structure. The interpretations are supported by the understanding of molecular processes obtained by molecular dynamics and structural measurements of gas-phase clusters, of macroscopic solid surfaces, and of solutions.

Structural and kinetics studies of phenomena at model oxide surfaces will elucidate mechanisms of the complex interfacial chemistry of the subsurface environment. This work focuses on the epitaxial growth of doped water (as amorphous ice) layers on metal-oxide surfaces, where direct measurements can be made of diffusion, dissolution, bimolecular reactions, and electrochemistry. Extrapolation of these findings to more complex natural systems is facilitated by theoretical models and through the results of direct liquid-phase and liquid–solid interface measurements. Using the near-field optical microscope, for example, the fate of a single molecule in solution or at an interface can be probed without averaging over spatially and temporally inhomogeneous environments of all molecules in the sample.

Many of the interfacial chemistry problems facing the DOE involve mixed organic/inorganic/radioactive materials. Thus, we need to address high-energy processes unique to this type of waste form, including the primary molecular processes of ionization and dissociation, and resulting reactions of high-energy species. Particular attention is given to the complex mechanisms of radiolytic (gamma ray, X ray, and electron)-induced degradation of current and future high-level nuclear waste forms: solidified waste, glasses, and ceramics. The emphasis here is on understanding the underlying physical and chemical mechanisms responsible for the formation of byproducts and loss of integrity in composite matrix materials.

Studies of the structure and bonding of organic ligands at oxide/water interfaces provides insight into geologically important mineral surfaces and environmentally significant ligand/complexant interactions. Isolated, gas-phase clusters of atoms that compose the actual surface are being synthesized to mimic surface structures. Spectroscopic determination of these structures is important to the evaluation of theoretical models of their chemical properties. Solvent–solvent and solvent–surface interactions are studied in a similar manner. Studies of both pure solvent and mixed solvent–substrate clusters help delineate the relative importance of the forces required to model the solvent effects. Likewise, reactant–substrate, reactant–solvent and solvent–reactant-substrate systems can be modeled as isolated clusters. Our approach to these very complex systems is to use the common practice of experimental extrapolation: small, simpler systems are subjected to quantitative theoretical and experimental analysis, which forms the basis for understanding more complex systems. For instance, while it may not be possible to obtain detailed structural data on solvent-reactant-substrate clusters, measurements of chemical reaction dynamics in these clusters can be modeled using approximate theories tested by previous application to simpler systems. Furthermore, we can deposit selected chemical species (including clusters) designed to mimic reactive sites on inert substrates and study their chemical activity. This work also has the potential for producing *designer surfaces* that may be valuable as chemical sensors or for development of unique materials for chemical separations.

Our activities in calendar year 1996 are summarized in this report.

2. Reaction Mechanisms at Interfaces

Experimental and Theoretical Study of Oxyanion Chemistry on Mineral Surfaces

*S. A. Joyce, B. J. Roop,**
M. A. Henderson,† and J. R. Rustad§

Supported by Laboratory Directed Research and Development (LDRD).

*AWU Visiting Scientist.
†EMSL Interfacial and Processing Science.
§Earth Systems Sciences Department, Thermodynamic and Molecular Geochemistry Group.

Adsorption, desorption, and diffusion of oxyanions on surfaces are important phenomena that occur during the transport of contaminants through soils. This study involves the application of experimental ultrahigh-vacuum (UHV) surface chemical and structural techniques combined with theoretical molecular mechanics to investigate the heterogeneous chemistry of oxyanions on mineral surfaces. Particular emphasis is placed on addressing the role of surface structure, both on the atomic and mesoscopic level, in the adsorption and subsequent chemistry of the adsorbed species. Both UHV surface science and geoscience are well established disciplines with many common scientific interests; however, historically there has been limited overlap between the practitioners. This work brings together the collaborative efforts of scientists in chemical physics, materials science and geochemistry.

In the first year of this project (calendar 1996), efforts were begun to: (1) develop efficient theoretical algorithms for dealing with large-scale simulations necessary for modeling complex geochemical interfaces; (2) establish procedures for attaining clean, well-characterized single crystalline samples; and (3) develop *in-situ* ultrahigh-vacuum synthetic routes for complex adsorbates such as the chromates. Progress in each of these areas will be described below.

Realistic atomic-scale simulations of geochemical interfaces typically require large numbers of atoms because of the large unit cells of most mineral crystals. Due to the scaling for exact methods, computations quickly become inefficient for large systems. A clear and rigorous derivation of the Ewald-like method was developed for calculating the electrostatic energy of the systems infinitely periodic in two dimensions and of finite size in the third dimension (slabs). The method, originally developed by Rhee *et al.*[1] to account for charge–dipole and dipole–dipole interactions, has been generalized, making it suitable for treatment of polarizable systems. It has the advantage over exact methods of being significantly faster, and therefore appropriate for large-scale molecular dynamics simulations. These simulations were applied to the surface relaxation of the nonhydroxylated, hydroxylated, and solvated surfaces of Fe_2O_3. Our nonhydroxylated structures and energies are found to be in close agreement with previous local density calculations on corundum (Al_2O_3) by Manassidis et al.[2] Using the results of molecular dynamics simulations of solvated interfaces, end-member hydroxylated-hydrated states are defined for the surfaces, which are then used in energy minimization calculations. Hydration has a small effect on the surface structure, but hydroxylation has a significant effect. Our calculations, both for gas-phase and solution-phase adsorption, predict a greater amount of hydroxylation for the hematite (012) surface than for the (001) surface and indicate the presence of four-fold coordinated iron ions on the (001) surface.

Large high-quality single crystals of many mineral materials are not generally available. Hematite is an exception, and several samples of α-Fe_2O_3 were acquired. These include synthetic single crystals of both (001) and (012) orientations, and two natural single-crystal specimens. One of the natural specimens has been indexed using X-ray diffraction and has been oriented along the (001) direction. The (012)-oriented synthetic sample was cleaned in ultrahigh vacuum to remove impurities (primarily sulfur and chlorine). A procedure for producing well-ordered surfaces has been developed. After annealing the sample in a background of oxygen at 900°C, a 1×1 low-energy electron diffraction (LEED) pattern shows that the surface has the same unit cell as the bulk, suggesting that the surface is a bulk-terminated structure. When the sample is annealed in vacuum, a 2×1 LEED pattern is observed as shown in Fig. 2.1. Vacuum annealing generally removes oxygen from oxide materials, resulting in a lower coordination and reduc-

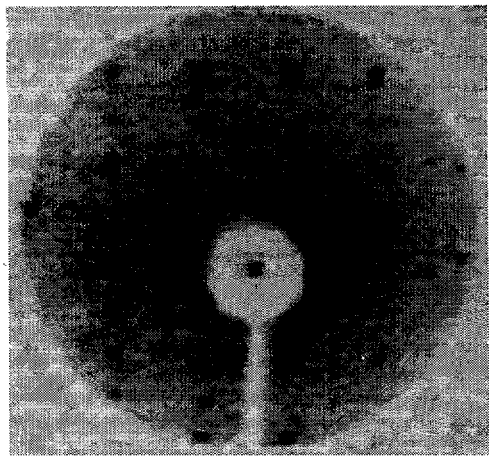

Figure 2.1. Structure of the 2×1 phase of the hematite (012) surface: low-energy electron diffraction acquired at 57 eV.

tion of the cationic species. The 2×1 surface unit cell is twice the size of the bulk cell, presumably due to ordering of the oxygen vacancies. This surface has been examined with scanning tunneling microscopy (STM); a representative image is shown in Fig. 2.2. The observed rows are separated by two unit cell lengths, consistent with the diffraction. Note also the large steps, several atomic heights, on the sample; such defect structures are not observed with diffraction techniques, and can only be directly determined using STM. The straightforward "recipe" for conversion between the 1×1 and 2×1 surface phases will be useful for chemical studies to determine the influence of surface coordination and charge state on heterogeneous reactions.

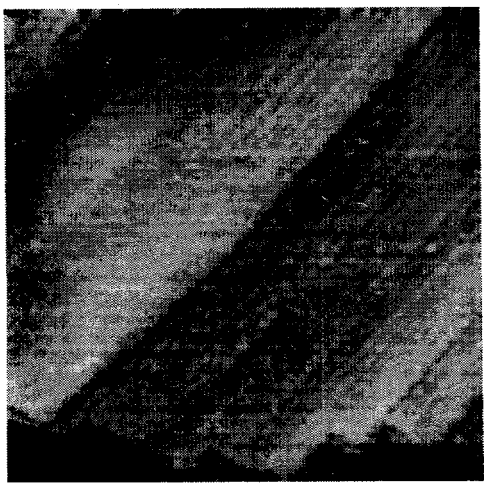

Figure 2.2. Structure of the 2×1 phase of the hematite (012) surface: scanning tunneling microscope image acquired with a 4-volt bias.

Many of the targeted probe molecules can be routinely dosed onto the hematite surfaces. Water and many of the organic acids have sufficiently high vapor pressures to allow for direct gas exposures. Direct exposure to phosphates and chromates is, however, problematic and requires *in situ* synthesis from suitable precursors. We have explored suitable analog molecules for the chromates that can be introduced into vacuum where a broad range of molecular-level spectroscopic techniques can be employed. As a result, we have conducted preliminary experiments using chromyl chloride (CrO_2Cl_2) in an effort to find a suitable analog of chromium oxyanions found in solution. The TiO_2(110) surface, although not of direct geochemical importance to the Hanford Site, is well-understood from a surface chemistry perspective, and thus was used in these preliminary experiments before initiating studies on Fe_2O_3. Temperature-programmed desorption studies reveal that CrO_2Cl_2 binds to the TiO_2(110) surface in a variety of adsorption states and decomposes to CrO_x and a Cl impurity. The limited amount of background adsorption of water inherent in UHV results in some removal of Cl as HCl. A significant amount of Cl can be removed by coadsorbing CrO_2Cl_2 with water, with an accompanying increase in the amount of deposited CrO_x species. These results provide promise that the chromium oxyanion–Fe_2O_3 interaction can be modeled using a coadsorbed layer of water and chromyl chloride.

References

1. Y.-J. Rhee, J. W. Halley, J. Hautman, and A. Rahman, *Phys. Rev. B* **40**, 36 (1989).
2. I. Manassidis, A. De Vita, and M. J. Gillan, *Surf. Sci.* **285**, L517 (1993).

Structure and Energetics of the Water/NaCl (100) Interface

*D. P. Taylor, W. P. Hess, and M. I. McCarthy**

Supported by DOE Office of Basic Energy Sciences.

*EMSL Theory, Modeling, and Simulation.

The problem of how water interacts with sodium chloride and other salt surfaces is an active topic of research in surface physics and environmental chemistry. Sodium chloride surfaces play a key role in heterogeneous chemical reactions that occur in the troposphere over the Earth's oceans.[1] Much of the earth is covered with saltwater, and ocean sprays carry sodium chloride, as well as water, into the atmosphere in large amounts. Airborne nitric oxide pollutants (NO_2, N_2O_5, $ClONO_2$) readily react with sodium chloride particles in the troposphere to form sodium nitrate and photochemically reactive chlorinated species.[2] Understanding the structure, energetics, and reactivity of water on salt surfaces is key to modeling these environmental phenomena.

Chemical reactivity of ionic crystal surfaces can be significantly altered by the presence of water.[3] Determining the properties of specific salt/water interfaces is complicated because these materials tend to be "structure sensitive"; that is, the interface chemistry and physics are very dependent on the local geometry of individual surface sites. Different sample preparation techniques can produce variations in the atomic-scale surface topology, which can result in dramatic changes in the observed structure and reactivity of the interfaces. Experimental[4,5] and theoretical[6] probes have been used to examine the water/NaCl (100) interface. These studies have reported two different types of structures for water adsorbed on NaCl (100). One proposed geometry is a (1×1) "monolayer," in which there is one water for each surface NaCl unit, with the water oxygen atoms located in the vicinity of the surface sodium and all of the water dipoles oriented in the same direction. Another proposed geometry is a hexagonal (4×2) "bilayer" structure.[4,5] The present work uses periodic Hartree-Fock (PHF) and correlation-corrected PHF theory as implemented in the program CRYSTAL[7] to investigate the energetics of (1×1) monolayer and (4×2) bilayer geometries. The (1×1) geometries contain one water molecule per NaCl unit cell. The (4×2) structures required supercells containing 12 waters. A mixed split valence basis set, optimized for NaCl bulk,[8] was used to describe the NaCl slab, of the form 8-511 on sodium and 86-311 on chlorine, and the standard Pople 6-31d set was used for water. Full analytic geometry optimizations are not possible using CRYSTAL92, so single energy point calculations (along selected coordinates) were used to probe the potential energy surface in the vicinity of local minima.

An example (1×1) monolayer structure is shown in Figs. 2.3–4. The monolayer structures contain one distinct water molecule for every surface NaCl unit. The binding energies and equilibrium distances are shown in Table I. In these configurations, the water oxygens are either located directly over a sodium site (Table I a,b) or one or both hydrogens are directly over a chlorine site (Table I c–e), respectively. The energetically favorable configuration occurs when the molecular dipole is aligned parallel to the surface plane, with the oxygens over the sodium sites (Table I a).

The recent He scattering measurements of Bruch *et al.*[5] obtain a fitted isosteric heat of adsorption for the 2D condensed phase of 14 ± 1 kcal/mol, and a single-molecule heat of adsorption of 15 ± 1 kcal/mol. Our calculated binding energies are analo-

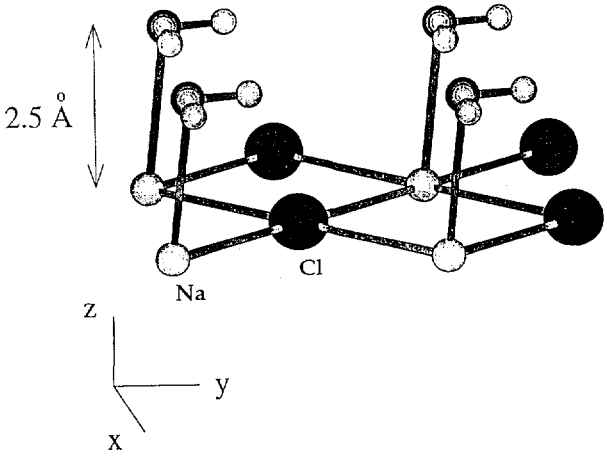

Figure 2.3. A (1×1) monolayer structure depicted in three-dimensional perspective. The water dipole is parallel to the surface plane with the oxygen atom located above the sodium atom but shifted by 0.2 Å in both x and y coordinates. The separation between the surface plane and the oxygen atom center is 2.5 Å.

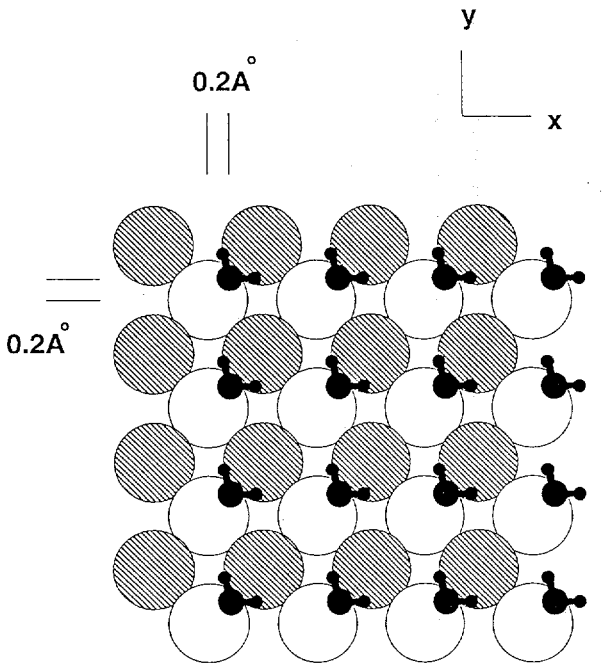

Figure 2.4. Top view of the monolayer structure depicted in Fig. 2.3

gous to fitted isosteric heat of adsorption values, because they include both water–water and water–surface contributions to the binding energy. Bruch *et al.*[5] assign the 2D condensed phase to be a (1×1) structure, with the water dipoles nearly parallel to the surface plane and the water oxygens moved off the sodium centers by 0.8 Å as shown in Fig. 2.5. Our *ab initio* calculations confirm that displacing the water oxygen from the sodium centers lowers the energy. The computed minimum occurs when the waters are displaced by 0.6 Å, corresponding to a binding energy of 10.4 kcal/mol at the PHF level and 13.5–15.6 kcal/mol with correlation (Table II).

The adsorption of water on thin films of NaCl (100) grown on Ge (100) substrates was probed with UPS, XPS, and LEED.[4,9] These experiments indicate a c(4×2) bilayer structure, with the waters' oxygens arranged in a hexagonal net on the surface with six symmetry-distinct waters per NaCl supercell (consisting of four NaCl units). The bilayer consists of a tightly packed net with the waters arranged in two "layers" with different oxygen–surface distances. Bilayer structures all contain 12 water molecules for every eight NaCl surface units (corresponding to 150% of the 1×1 coverage). We constructed (4×2) geometries based on the proposed models and computed the *ab initio* energetics. We fixed the "upper" and "lower" oxygen–surface distances at 3.5 Å and 2.5Å, respectively; these values were determined independently from the equilibrium positions computed for the corresponding monolayer structures.

Table I. Geometries (PHF) and calculated adsorbate/surface binding energies and interaction energies of the water nets without the surface present (PHF and with correlation corrections). Negative binding energies denote attractive interactions and positive numbers indicate repulsive interactions. PHF equilibrium distances ($R_{w\text{-}surf}$) are defined between the water oxygen and the plane of the surface. All calculations were run using a three-layer slab NaCl (100).

Geometry	Binding Energy (kcal/mol)	Water-Water Interaction Energy (kcal/mol)
a 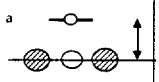	$R_{w\text{-}surf}$ =2.5 Å over Na	
	PHF = -9.8	PHF = -3.4
	PHF+ CS = -13.4	PHF+CS = -3.6
	PHF + P86 = -12.3	PHF+P86 = -3.4
	PHF+ P91 = -11.6	PHF+P91 = -3.4
b 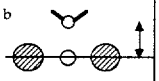	$R_{w\text{-}surf}$ = 2.3 Å over Na	
	PHF = -3.4	PHF = +3.5
	PHF + CS = -7.5	PHF + CS = +3.5
	PHF + P86 = -6.2	PHF + P86 = +3.8
	PHF+ P91 = -5.3	PHF + P91 = +3.7
c 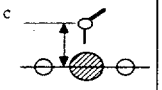	$R_{w\text{-}surf}$ = 3.7 Å over Cl	
	PHF = -2.5	PHF = -0.6
	PHF + CS = -3.7	PHF + CS = -0.7
	PHF + P86 = -3.3	PHF + P86 = -0.6
	PHF + P91 = -3.2	PHF + P91 = -0.6
d 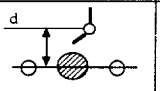	$R_{w\text{-}surf}$ = 3.4 Å (oxygen to surface plane)	
	PHF = -1.7	PHF = -0.6
	PHF + CS = -2.8	PHF + CS = -0.7
	PHF + P86 = -2.3	PHF + P86 = -0.6
	PHF + P91 = -2.1	PHF + P91 = -0.6
e 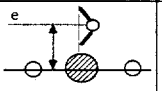	$R_{w\text{-}surf}$ = 3.5 Å (oxygen to surface plane)	
	PHF = -3.7	PHF = -1.8
	PHF + CS = -5.1	PHF + CS = -1.9
	PHF + P86 = -4.7	PHF + P86 = -1.8
	PHF + P91 = -4.5	PHF + P91 = -1.8

These calculations indicate several energetically favorable arrangements for water on NaCl (100). The most stable monolayer geometry occurs with the molecular dipole aligned nearly parallel to the surface plane, and the water bound in the vicinity of the sodium site with binding energies of 10–11 kcal/mol at the PHF level and 12–16 kcal/mol with correlation corrections, in close agreement with the experimental values.[5] Much weaker interactions occur in monolayer structures with the waters "hydrogen bonded" to the chloride sites. Small changes in the binding energy were observed when the in-plane angular orientation of the water was changed. This implies that there may be multiple local minima on the water/NaCl

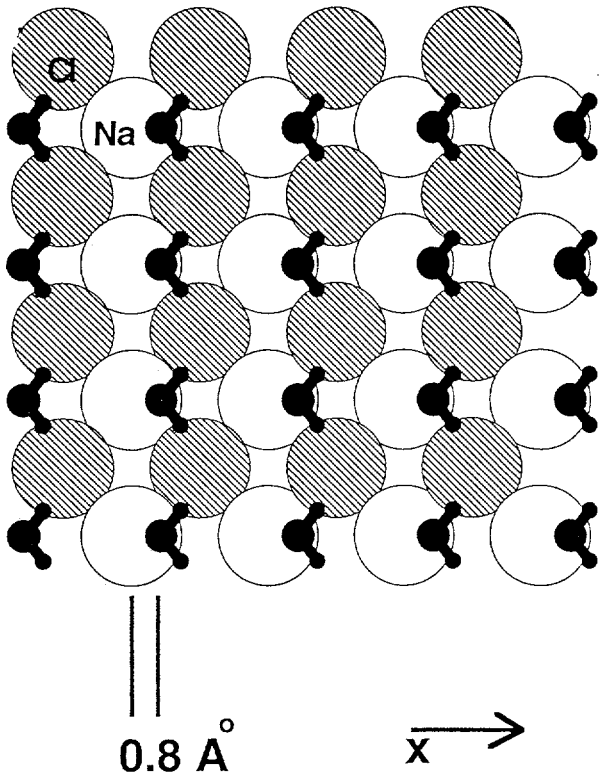

Figure 2.5. The (1×1) structure determined by Bruch *et al.*[5] using helium scattering as a probe (top view). The water dipoles are aligned parallel to the *x* coordinate and nearly parallel to the NaCl (100) surface plane. The oxygen atoms are located above the sodium atom centers, shifted by 0.8 Å.

potential energy surface corresponding to similar (1×1) monolayer geometries. These structures could exist as separate domains on the surface.

The (4×2) bilayers can be viewed (approximately) as a combination of two monolayer geometries: water parallel to the surface over sodium sites and water "hydrogen-bonded" to chloride sites. The calculated binding energies for several proposed (4×2) bilayer geometries ranged from 5.6–9.6 kcal/mol at the PHF level to 8.0–14.5 kcal/mol with correlation corrections. These are similar to the experimental values reported by Folsch[4] and to the computed (1×1) monolayer geometries. However, the (4×2) structures have 150% higher packing density, and hence the formation energy per unit area is greater for the (4×2) structures. The increase in the water–water attraction energy at the higher (4×2) packing density (relative to the monolayer) stabilizes these structures. Based on the computed energetics, it is reasonable to expect

Table II. Comparison of monolayer adsorbate/surface binding energies. Negative binding energies denote attractive interactions and positive numbers indicate repulsive interactions. All of these calculations were run using a one-layer slab NaCl (100). All calculations for 1×1 monolayer geometry.

Structure	Binding energy (kcal/mol)	Water–water interaction energy (kcal/mol)
Optimized planar water over sodium (Figs. 2.3–4)		
PHF	–10.8	–3.4
PHF + CS	–15.1	–3.6
PHF + P86	–14.0	–3.4
PHF + P91	–13.1	–3.4
Planar water over sodium (in optimized "Bruch")		
PHF	–10.4	–1.5
PHF + CS	–15.6	–1.6
PHF + P86	–14.5	–1.4
PHF + P91	–13.5	–1.5

that domains of (1×1) and (4×2) structures could coexist on NaCl(100), with their relative concentrations being dependent on sample conditions such as surface preparation technique, coverage, and temperature. The (4×2) geometries may become more stable as the coverage is increased, but the mechanism (reaction path) for converting between (1×1) and (4×2) geometries is yet undetermined.

References

1. J. M. Laux, J. C. Hemminger, and B. J. Finlayson-Pitts, *Geophys. Res. Lett.* **21**, 1623–1626 (1994).
2. W. C. Keene, A. A. Pszenny, D. J. Jacob, R. A. Duce, J. N. Galloway, J. J. Schultz-Tokos, H. Sievering, and J. F. Boatman, *Global Biogeochem. Cycles* **4**, 407–429 (1990).
3. V. E. Henrich and P. A. Cox, *The Surface Science of Metal Oxides* (Cambridge University Press, New York, 1994).
4. S. Folsch, A. Stock, and M. Henzler, *Surf. Sci.* **264**, 65 (1992).
5. L. W. Bruch, A. Glebov, J. P. Toennies, and H. Weiss, *J. Chem. Phys.* **103**, 5109 (1995).
6. S. Picaud and C. Girard, *Chem. Phys. Lett.* **209**, 340 (1993).
7. R. Dovesi, V. R. Saunders, and C. Roetti. *CRYSTAL92 Users Manual* (Universita di Torino, Italy, and SERC Daresbury Laboratory, U.K., 1992).

8. E. Apra, M. Causa, M. Prencipe, R. Dovesi, and V. R. Saunders, *J. Phys.: Cond. Mat.* **5**, 2969 (1993).
9. S. Folsch and M. Henzler, *Surf. Sci.* **247**, 269 (1991).

Molecular Beam Surface Scattering and Kinetics Instrumentation

G. A. Kimmel, M. A. Covert, S. E. Barlow, R. S. Smith, and B. D. Kay

Supported by DOE Office of Basic Energy Sciences and the EMSL Project.

Molecular beam scattering from surfaces is a powerful experimental tool for studying the dynamics and kinetics of the interaction of molecules with surfaces. The coupling of surface science, molecular beam, and laser technologies makes possible the measurement of total energy disposal and redistribution in gas–surface scattering. Previously these experimental methods were employed to acquire detailed surface kinetics and state-to-state scattering measurements of molecules interacting with metallic substrates. Such experiments resulted in a fairly detailed understanding of surface chemistry on metals. Unfortunately, we have no similar understanding of the elementary dynamical and kinetic processes occurring on ice and oxide surfaces. Such interactions are clearly important from an environmental viewpoint, because they form the molecular-level basis for the complex physiochemical processes that take place on the surface of atmospheric aerosols, at the aqueous–mineral geochemical interface, and at the vapor–liquid interface. Our goal is to apply and extend molecular beam surface scattering techniques to these systems in an effort to elucidate the relevant interactions. Toward this goal we have designed and are currently constructing three new state-of-the-art molecular beam-surface scattering and kinetics instruments. This unique set of instrumentation will allow us to investigate the dynamics and kinetics of surface interactions in unprecedented detail. These instruments are expected to become operational in the summer of 1997.

EMSL Molecular Beam Surface Scattering Facility

As part of the EMSL project, we have designed two molecular beam scattering machines (ICS-1 Instruments I and II) and a low-energy ion beam line. A plan view of the EMSL Molecular Beam Surface Scattering Facility is displayed in Fig. 2.6. These ultrahigh vacuum (UHV) machines will have a base pressure of 1×10^{-10} Torr in the scattering chambers. Both Instruments I and II are equipped with three coplanar molecular beam lines which intersect at the sample target location within the scattering chamber. The two outer beams are at an angle of ±15° with respect to the central beam. Each beam can be independently controlled and can be run as a continuous or pulsed effusive or supersonic beam. The three beams can be synchronously modulated via computer-controlled high-speed chopper wheels with microsecond time resolution. The primary difference between Instruments I and II is the distance the beam sources reside from the scattering target. Instrument I has an increased source-to-target distance that allows direct backscattering geometries to be examined. The source-to-target distance on Instrument II is much shorter, allowing for more intense beams to be generated.

In each instrument the surface scattering target is mounted on a 4-axis manipulator and placed at the intersection point of the three molecular beams. The sample is cooled with a closed-cycle helium refrigerator and will attain a base temperature of 20 K. The sample stage is designed to allow rapid thermal cycling between 25 K and 1200 K. The sample's temperature is maintained by a programmable temperature controller.

Both the incident and scattered molecular beams can be detected via a differentially pumped neutral atom/molecule detector. This detector is mounted on a large rotary flange assembly whose axis of rotation is perpendicular to the plane defined by the molecular beams and passes through the intersection point of the beams. The detector consists of an electron impact ionizer, an electrostatic quadrupole bender, and a quadrupole mass spectrometer. The detector is mounted inside a double differentially pumped manifold to significantly increase the signal to background ratio for the desorbed/scattered flux of atoms or molecules. With this detector we will be able to

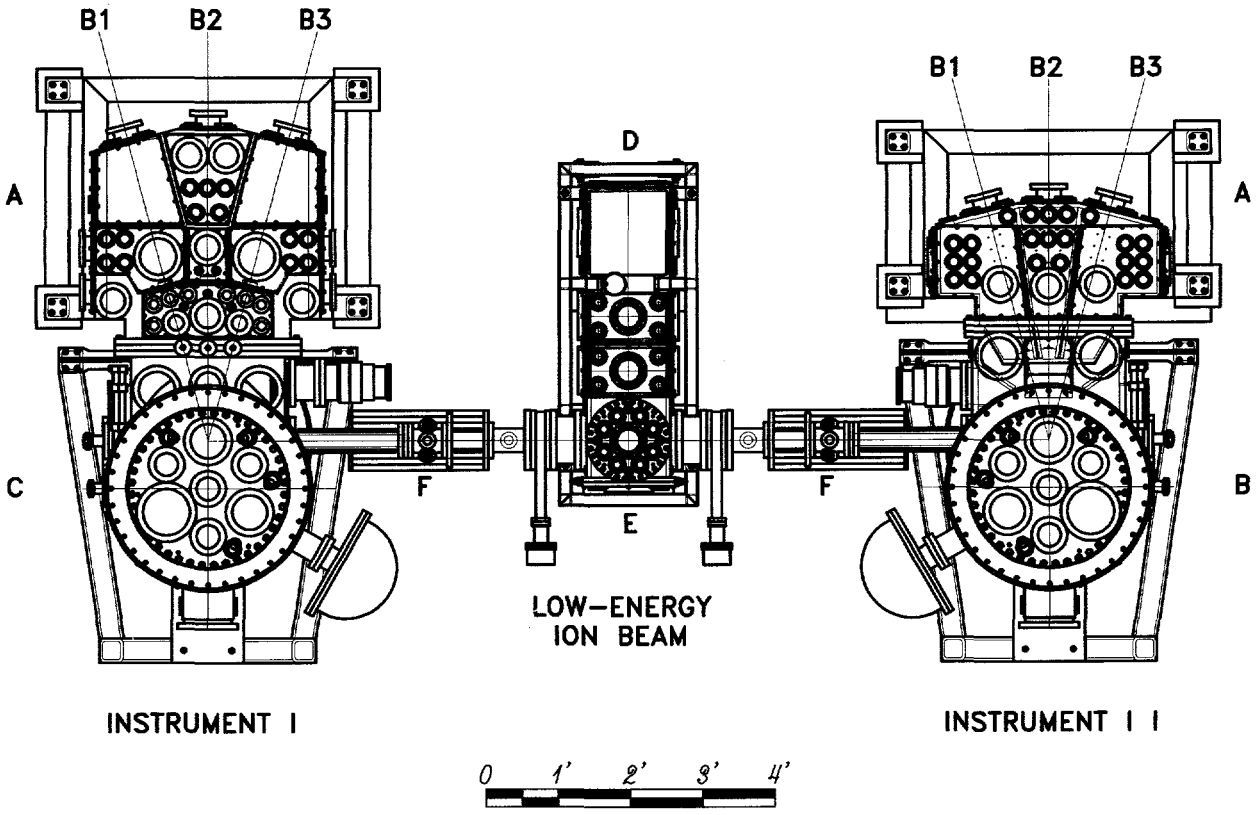

Figure 2.6. Plan view of EMSL Molecular Beam Surface Scattering Facility, comprised of ICS Instrument I, Instrument II, and the Low-Energy Ion Beam. (A) Triply differentially pumped beam source vacuum chambers; (B1–3) molecular beam lines; (C) doubly differentially pumped UHV surface scattering chambers; (D) differentially pumped ion beam source and mass filter; (E) electrostatic quadrupole ion beam bender; (F) retractable ion beam focusing and deceleration lens assembly.

measure velocity and angular distributions of the desorbed/scattered flux. In addition, the detector is designed to allow the incident beam to pass through it so that it can measure the directly backscattered flux in Instrument I.

The target sample manipulator is also mounted on a large rotary flange assembly, allowing the sample to be positioned either at the intersection point of the molecular beams or in front of a number of surface preparation and characterization instruments. Both instruments are equipped with a sputter ion gun for sample cleaning and an Auger electron spectrometer (AES) and a low-energy electron diffraction (LEED) spectrometer for monitoring surface composition and order, respectively. The UHV chamber also houses a number of effusive beam evaporators. These evaporators will be employed to synthesize compositionally tailored nanoscale oxide and ice surfaces.

In addition to the dedicated surface analytical instrumentation described above, Instruments I and II share a suite of specialized instrumentation comprised of an X-ray photoelectron spectrometer (XPS), a Fourier-transform infrared (FTIR) spectrometer, a Kelvin probe, a six-axis sample manipulator, and a low-energy ion beam line.

The ion beam line can produce mass-selected, monoenergetic ion beams with energies ranging from 10 eV to 3000 eV. The ion beam line can be operated in two different modes, depending on the final energy of the ions. For high-energy beams ($E_i \geq 400$ eV), the ions are transported through the beam line at their final energy. However, due to space-charge spreading of the ion beam, this approach does not work for low-energy beams. Therefore, for $E_i < 400$ eV, the ions are transported through the beam line at 400 eV and decelerated to their final energy just prior to striking the sample. An electrostatic quadrupole

bender can be used to direct the ion beam into either Instrument I or II. The ion beam is focused onto the target using a retractable deceleration lens assembly. This assembly can also be employed to deposit very low energy (<5 eV) ions onto the target. The scattered ion flux can be detected with a rotatable electrostatic energy analyzer and/or quadrupole mass spectrometer.

Beam Surface Kinetics Instrument

Supported by DOE Office of Basic Energy Sciences.

We have designed a state-of-the-art molecular beam surface scattering instrument for examining surface kinetics. The design of this instrument enables the simultaneous detection of both gaseous and surface species while the target is exposed to a flux of two reagents. The instrument has a modular design to facilitate interchangeability and adaptability for collaborative research. A plan view of the Beam Surface Kinetics instrument (BSK) is displayed in Fig. 2.7. In this instrument two molecular beams intersect at 90° on a target surface residing within a UHV scattering chamber.

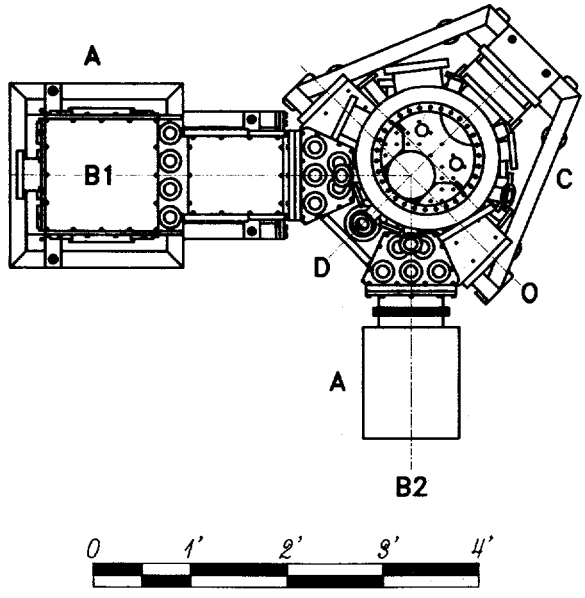

Figure 2.7. Plan view of the Beam Surface Kinetics instrument. The instrument is comprised of (A) triply-differentially-pumped beam source vacuum chamber; (B1 and B2) molecular beam lines; (C) UHV surface scattering and analysis chamber; (D) fixed-angle differentially-pumped detector; and (O) optical access for FTIR and REMPI studies.

Each beam can be independently controlled and can be run as a continuous or pulsed effusive or supersonic beam. Both beams can be synchronously modulated via computer-controlled high-speed chopper wheels with microsecond time resolution. Each beam line is independently triply differentially pumped while maintaining a source-to-target distance sufficiently short to enable use of intense beams having fluxes in excess of 100 monolayers/sec. A differentially pumped stationary neutral atom/molecule detector resides between the two incident beams and can detect particles scattering or desorbing along the surface normal. Other geometries can be examined by rotating the target surface. The detector is an electron impact quadrupole mass spectrometer whose axis lies within the principal scattering plane. This detector can also be used to detect ions issuing from the surface or generated via laser photoionization.

The surface scattering target is mounted on a 4-axis manipulator and placed at the intersection point of the two molecular beams. The sample is cooled with a closed-cycle helium refrigerator and will attain a base temperature of 20 K. The sample stage is designed to allow rapid thermal cycling between 25 K and 1200 K. The sample's temperature is maintained by a programmable temperature controller. The target sample manipulator is also mounted on a large rotary flange assembly that allows the sample to be positioned either at the intersection point of the molecular beams or in front of a number of surface preparation and characterization instruments. The instrument is equipped with a sputter ion gun for sample cleaning, and an AES and a LEED spectrometer for monitoring surface composition and order, respectively. The UHV chamber also houses a number of effusive beam evaporators. These evaporators will be employed to synthesize compositionally tailored nanoscale oxide and ice surfaces. In addition to the dedicated surface analytical instrumentation described above, the instrument has an FTIR spectrometer and a secondary ion mass spectrometer (SIMS) that can be employed while the sample target is being exposed to reagent fluxes from the two molecular beams. This novel feature enables both the gaseous and surface species to be simultaneously monitored under actual reaction conditions.

Kinetic Processes in Nanoscale Films of Amorphous Solid Water

R. S. Smith, C. Huang, and B. D. Kay*

Supported by DOE Office of Basic Energy Sciences.

*Postdoctoral Research Associate.

Amorphous materials are important in a variety of scientific disciplines, including chemistry, physics, materials science, and biology. Amorphous solid water (ASW) is of special importance for many reasons, including the open question over its applicability as a model for liquid water, and fundamental interest in the properties of glassy materials. In addition to the properties of ASW, understanding the microscopic intermolecular interactions between ASW and an adsorbate is important in such diverse areas as solvation in aqueous solutions, cryobiology, and desorption phenomena in cometary and interstellar ices.

Evaporation Rate, Free Energy, and Entropy of Amorphous Water at 150 K

The residual entropy of glassy water is of considerable theoretical significance. For supercooled and amorphous water to be connected by a reversible isobaric path, the residual entropy of glassy water must satisfy strict bounds imposed by thermodynamic consistency. If these are not satisfied, continuity is impossible, and glassy water is a distinct phase. Although this question has been discussed theoretically, the key quantity, the residual free energy of glassy water, has not been measured. We measure the evaporation rate of amorphous water and ice at 150 K. From this measurement we calculate the residual free energy of the glass and discuss the implications for the continuity problem.[1]

There is still debate about whether glassy water becomes a liquid before it freezes to ice near 150 K. From spectroscopic studies of the rates of isotope exchange processes in the glass, Fisher and Devlin[2] conclude that the very weak glass transition reported near 130 K is a manifestation of the onset of molecular rotation in the glass, rather than transformation to a diffusing liquid, and that the glass freezes directly to ice near 150 K without passing through an intermediate liquid state.

The Gibbs free energy difference between two condensed phases, 1 and 2, of the same substance is related to the ratio of their vapor pressures, when the vapor is ideal, by

$$\Delta_1^2 G = RT \ln(p_2/p_1). \quad (1)$$

In our experiments we measure the rate of evaporation under a vacuum of 10^{-10} Torr, which prevents recondensation. The sticking coefficient of water on ice is unity over the range of temperature of our experiments.[3] A sticking coefficient of unity means that all molecules that impinge on the ice surface lose sufficient energy to become trapped in a bound state. Under this condition, the adsorption rate is equal to the surface collision rate, which from elementary kinetic theory is directly proportional to the pressure p above the surface. At equilibrium, the adsorption and evaporation rates are equal, and p is the vapor pressure. Consequently, the evaporation rate r_e is proportional to the equilibrium vapor pressure. Assuming that it makes sense to speak of the equilibrium vapor pressure of the amorph, p_a, we have $r_{e,a}/r_{e,i} = p_a/p_i$. The free energy difference between the amorph and ice is then given by

$$\Delta_i^a G = RT \ln(r_{e,a}/r_{e,i}). \quad (2)$$

Amorphous films 30 to 1000 molecular layers thick were grown by vapor deposition at a rate of 0.05 monolayer/s onto the Ru (001) substrate at 85 K. The evaporation rate was measured as the sample was heated or cooled at a linear rate of 0.6 K/s. At the highest temperature, the desorption rate of ~1 ML/s corresponds to a vapor pressure of $\sim 10^{-6}$ Torr, so only 1 desorbing molecule in $\sim 10^4$ can readsorb. Under these conditions, the experiment measures the free desorption rate, which for a sticking coefficient of unity is directly proportional to the vapor pressure. The amorphous deposits freeze at 155–165 K. Other studies show that glassy water freezes to cubic ice.

Experimentally determined desorption rates for both the H_2O amorph and crystalline ice are shown in Fig. 2.8(A). In this experiment a 100-molecular-layer–thick film is deposited on an 85-K substrate. The film is then heated from 85 K to 163 K, immediately cooled back to 85 K, and then reheated to 200 K to desorb the entire film. The initial heating/cooling cycle exhibits a pronounced hysteresis in which the desorption rate is higher upon heating than cooling. This hysteresis is absent in subsequent heating/cooling cycles and arises from the irreversible transformation of the amorph into crystalline ice during the initial

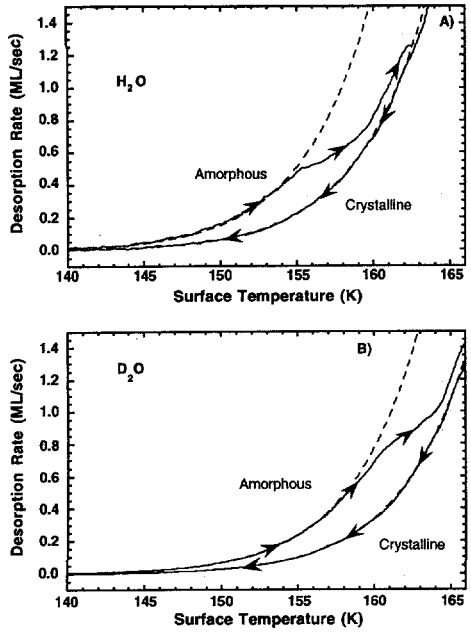

Figure 2.8. The desorption rate from 100-ML-thick films of amorphous H_2O (A) and D_2O (B) as they are heated and cooled at a rate of 0.6 K/s. The hysteresis is due to the freezing of the films to cubic ice, which is more stable and evaporates slower. The arrows on the curves indicate the direction of the temperature ramp. The dashed lines are Arrhenius fits to the desorption rates.

heating. The higher desorption rate for the amorph is a manifestation of the excess free energy of the metastable phase. As the amorph crystallizes, the measured desorption rate approaches that of the crystalline ice phase in the temperature range 155–163 K. The kinetics of the crystallization are discussed in detail elsewhere.[4]

The dashed lines displayed in Figure 2.8(A) represent Arrhenius fits to the desorption rates for the amorph and crystalline ice films. Figure 2.8(B) shows analogous results obtained for D_2O. These experiments have been repeated many times for a variety of incident beam fluxes and film thicknesses, and the results are reproducible.

The difference in free energy between crystalline ice and the amorph was calculated from Eq. (2). The solid lines in Fig. 2.9 are the free energy differences calculated directly from the experimentally measured rates at each temperature for both H_2O and D_2O; the dashed lines are calculated from the constrained Arrhenius fits. The slopes of the

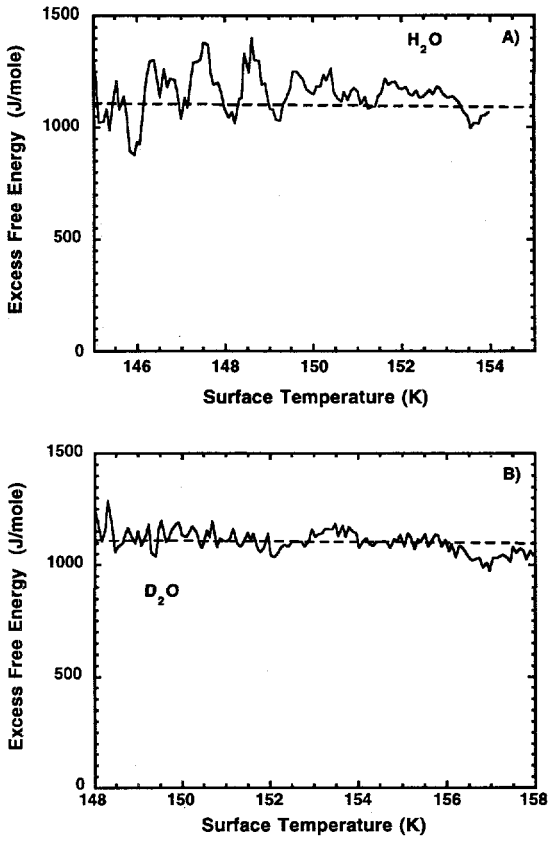

Figure 2.9. The excess Gibbs free energy of the amorphous films of H_2O and D_2O relative to cubic ice, calculated from Eq. (2). The solid line is a point-by-point ratio of the experimental data and the dashed line is calculated from the Arrhenius parameters.

lines give the entropy difference,

$$\Delta_i^a S = -(\partial \Delta_i^a G / \partial T).$$

The free energy difference, $\Delta_i^a G$ (150 K) = 1100 ± 100 J/(K mol), which, together with the known enthalpy difference and heat capacity data, suggest a residual entropy difference of $\Delta_i^a S$ (0) = –0.7 ± 2.2 J/(K mol) at absolute zero. Previous theoretical estimates of $\Delta_i^a S$ (0) are much larger, but do not allow the amorph to be connected with normal liquid water by a reversible thermodynamic path at atmospheric pressure. The present value allows such a connection.

Diffusivity of Amorphous Water

We developed a computer-based mathematical model that couples our previous mean-field description of the desorption/crystallization kinet-

ics[4] to a one-dimensional representation of the diffusive motion between layers. This combined model enables us to extract the temperature-dependent diffusion coefficient for the amorphous phase. Knowledge of the diffusivity as a function of temperature is requisite to determining if ASW is a metastable extension of supercooled liquid water or a distinct thermodynamic phase. Analysis of our experimental results strongly suggest that the diffusivity of ASW is consistent with a metastable extension of supercooled liquid water. This is an important finding, for it demonstrates that studies of nanoscale thin films of ASW in the temperature range 140–160 K are germane to physical and chemical processes occurring in normal liquid water.

Figure 2.10 displays a temperature-programmed desorption (TPD) experiment for 17 layers of $H_2{}^{16}O$ deposited on top of 16 layers of $H_2{}^{18}O$. The symbols are the experimental data and the solid lines are the model simulation. If the isotopically tailored layers did not exhibit diffusive intermixing, all of the $H_2{}^{16}O$ molecules would desorb prior to the onset of $H_2{}^{18}O$ desorption. This would be expected if the ASW phase had the diffusivity of crystalline ice. The experiment clearly shows that nearly complete mixing is observed above 154 K, and that the mixing process occurs in concert with the crystallization of ASW. The four illustrations in the bottom of the figure display the vertical spatial distribution of the isotopes. At 146 K the isotopes are vertically separated, by 152 K significant intermixing has occurred, and by 158 K the layers have completely mixed and film has crystallized. As the temperature is raised further the sample desorbs congruently.

Figure 2.11 shows TPD spectra as a function of increasing film thickness. As the film thickness increases, the films exhibit departures from complete mixing. This is a combined result of the finite value the ASW diffusivity and the fact that upon crystallization the diffusive motion becomes effectively frozen out. For all thicknesses, the model simulation is in excellent agreement with the experiment. This agreement enables the temperature-dependent diffusivity of ASW to be determined between 150 and 160 K. At 160 K the diffusivity is roughly 10^6 times larger than that of solid crystalline ice.

Figure 2.12 shows the temperature dependence of the ASW diffusivity (open symbols) in the temperature range 150–160 K. Also displayed are tabulated data for the diffusivity of liquid water and crystalline ice (solid symbols). The solid lines are Arrhenius extrapolations of the liquid and crystalline diffusivities, respectively.

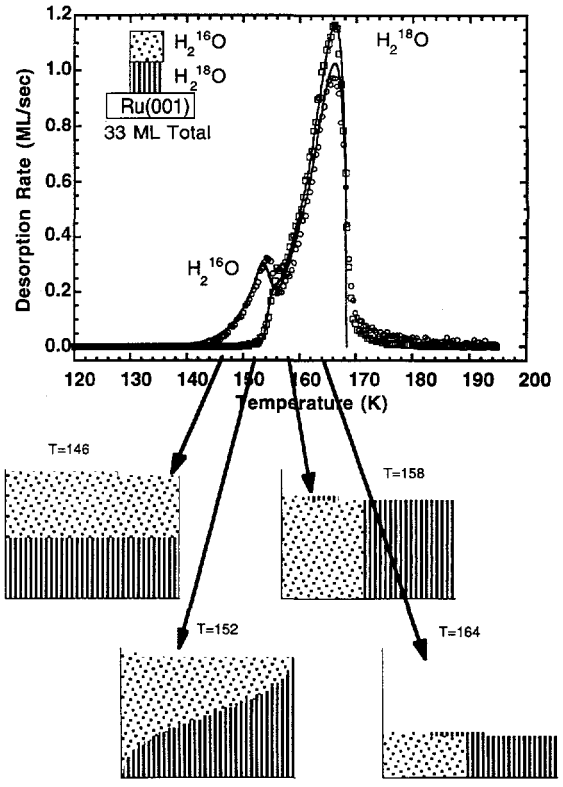

Figure 2.10. TPD experiment for 17 layers of $H_2{}^{16}O$ deposited on 16 layers of $H_2{}^{18}O$. The symbols are the experimental data and the solid lines are the model simulation. The graphs below the spectra show the extent of mixing of the two isotopes at the given temperature.

The TPD results are inconsistent with both Arrhenius extrapolations, exhibiting a much stronger temperature dependence with an apparent activation energy of ~60 kcal/mole over the 10 K temperature range of our experiment. Glass-forming liquids exhibit markedly non-Arrhenius behavior as they are supercooled below their freezing point. As the temperature is further lowered toward the glass temperature, the diffusivity effectively vanishes due to a divergence in the viscosity of the supercooled liquid. The temperature dependence of this phenomenon is well represented by the Vogel-Fulcher-Tamann (VFT) equation. The solid line in Fig. 2.12 is a simultaneous fit of the diffusivities of liquid water, supercooled liquid

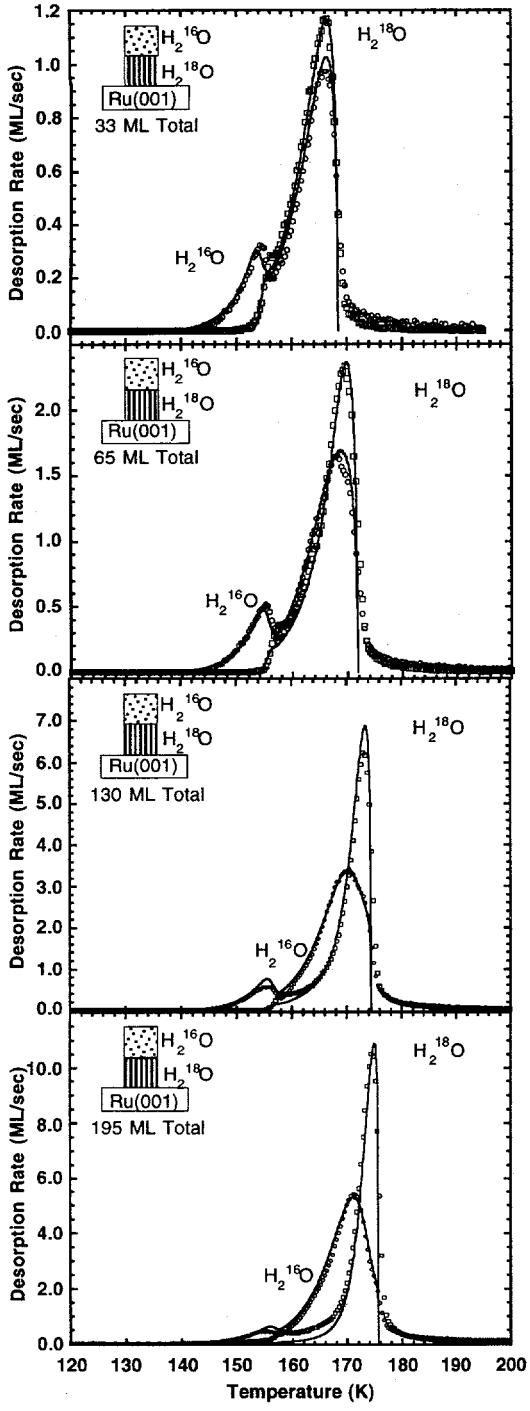

Figure 2.11. TPD spectra as a function of increasing film thickness. The symbols are the experimental data, and the solid lines are the model simulation.

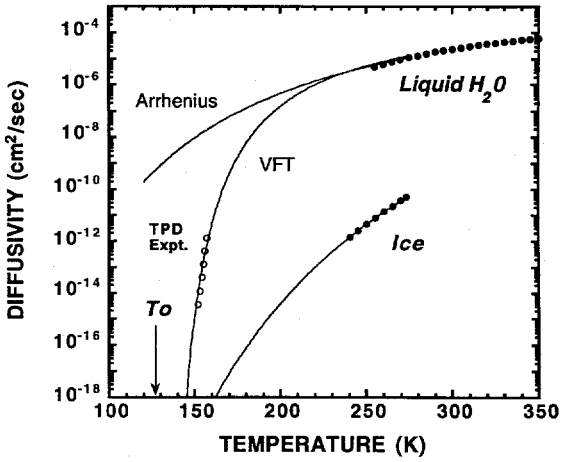

Figure 2.12. Temperature dependence of the ASW diffusivity (open symbols) in the temperature range 150–160 K. Also displayed are tabulated data for the diffusivity of liquid water and crystalline ice (solid symbols). The solid lines are Arrhenius extrapolations of the liquid and crystalline diffusivities.

water, and our results for ASW. It is evident that the VFT equation fits all the data extremely well. Furthermore, the ideal glass temperature T_0 of 128 K from the global fit is in close agreement with the experimentally determined calorimetric glass transition temperature for ASW.

Analysis of these results strongly suggest that the diffusivity of ASW is consistent with a metastable extension of supercooled liquid water. This important finding demonstrates that studies of nanoscale thin films of ASW at 140–160 K are germane to physical and chemical processes in normal liquid water. Near 160 K the diffusivity of ASW reaches ~10^{-12} cm^2/sec, roughly 10^{-7} times the diffusivity of normal liquid water at room temperature. Such a diffusivity would be nearly impossible to observe with a macroscopic sample—a 1-cm-thick film would require ~10^5 years to mix!

Structural Thresholds During the Amorphous-to-Crystalline Water Ice Phase Transition

Water and CCl_4 are immiscible, and are thus an ideal model system for studying hydrophobic interactions. We use molecular beams with high spatial resolution to create ultrathin (<1000 Å) films and TPD to study the desorption kinetics of the layered interfaces. The desorption kinetics for multilayer films of CCl_4 and amorphous water ice have been studied.

Figure 2.13 displays TPD spectra for films composed of CCl_4 and amorphous water. The upper

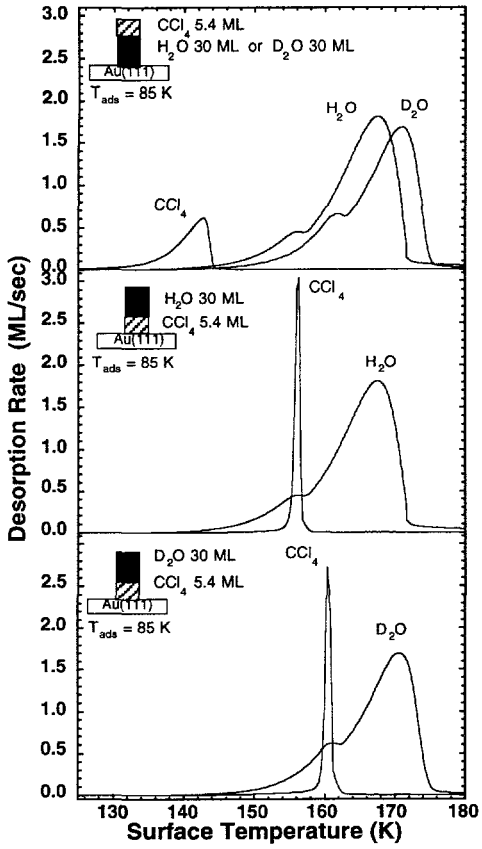

Figure 2.13. (Top) TPD spectra for nanoscale films of 5.4 ML CCl_4 grown on 30 ML of either H_2O or D_2O amorphous water ice. The CCl_4 desorption from either water substrate is the same. The "bump" in the water desorption spectra (~156 K for H_2O and ~162 K for D_2O) arises from the irreversible phase transformation of the amorphous solid into crystalline ice. (Middle) TPD spectra for nanoscale films of ~30 ML of H_2O amorphous solid grown on ~5.4 ML CCl_4. (Bottom) TPD spectra for nanoscale films of ~30 ML of D_2O amorphous solid grown on ~5.4 ML CCl_4. The lower two spectra show that the CCl_4 is trapped beneath the amorphous water deposit and then desorbs abruptly in concert with the phase transition.

panel shows the TPD spectra for films where CCl_4 is grown on top of amorphous H_2O or D_2O. These TPD spectra are indistinguishable from samples in which CCl_4 and amorphous water are deposited in spatially separate columns. Because the CCl_4 desorption rate is much greater than the water desorption rate, the CCl_4 film is completely desorbed prior to significant water desorption. The "bump" in the water desorption spectra (~156 K for H_2O and ~162 K for D_2O) arises from the irreversible phase transformation of the amorphous solid into crystalline ice.[1] The bump is observed during the transformation to the more stable crystalline phase. For the purpose of this study the bump in the TPD spectrum is the hallmark of crystallization. The desorption spectra for H_2O and D_2O are shifted by ~6 K due to zero-point energy differences.

The lower two panels of Fig. 2.13 show TPD spectra for films where an amorphous water multilayer of H_2O or D_2O is grown on a CCl_4 film. The overlayer impedes CCl_4 desorption until the temperature range for amorphous water crystallization. At this higher temperature, abrupt CCl_4 desorption occurs completely over a narrow temperature range prior to the desorption of the majority of the water film. The CCl_4 desorption peak shifts with the temperature of the phase transition bump for both H_2O and D_2O, suggesting that the CCl_4 desorption through the water overlayer is directly correlated with the amorphous-to-crystalline phase transition.

Figure 2.14 shows an Arrhenius plot of the CCl_4 desorption rate data in Fig. 2.13. The solid lines correspond to desorption from a film with no overlayer, one with a 30-ML H_2O overlayer, and one with a 30-ML D_2O overlayer. The dashed line is an Arrhenius fit to the multilayer desorption part of the CCl_4 desorption curve with no water overlayer, and hence is equal to the free evaporation rate. The two desorption curves with water overlayers show similar behavior. At low temperatures the desorption rates are 100-fold lower than the ice desorption rate, but exhibit roughly the

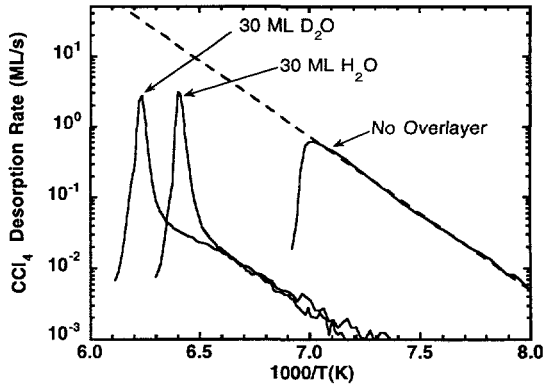

Figure 2.14. An Arrhenius plot of the CCl_4 desorption rate data in Fig. 2.13.

same apparent activation energy. At higher temperatures there is an abrupt increase in the slope of both curves, indicating a rapid increase in the desorption rate. The onset of rapid desorption is shifted by 6 K for the two curves, and is consistent with the temperature difference between H_2O and D_2O phase-transition kinetics. The extreme change in slope indicates a dramatic change in the CCl_4 desorption mechanism.

Figure 2.15 shows an Arrhenius plot of the CCl_4 desorption rate from nanoscale films with various amorphous D_2O overlayers (0, 15, 30, 60 ML). The dashed line is a fit to the curve with no D_2O overlayer. The abrupt change in slope shifts to higher temperature with increasing thickness of the D_2O overlayer, reaching a thickness-independent value for overlayers thicker than 60 ML. This is consistent with the thickness dependence of the amorphous-to-crystalline phase transition kinetics.[4] Also note that the desorption rate in the leading-edge region decreases with increasing overlayer thickness, and for the 60-ML overlayer there is no observed desorption. This indicates that as the thickness of the overlayer increases, the probability of finding a connected desorption pathway through the entire overlayer decreases. At the phase transition, however, structural changes in the amorphous overlayer create numerous connected pathways through the water overlayer.

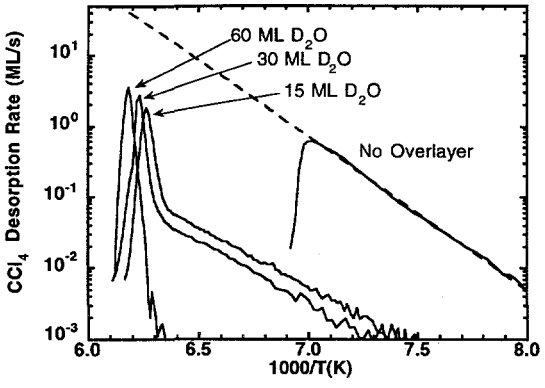

Figure 2.15. An Arrhenius plot of the CCl_4 desorption rate from nanoscale films with various amorphous D_2O overlayers. The dashed line is a fit to the curve with no D_2O overlayer. The abrupt change in slope shifts with the thickness of the D_2O overlayer, consistent with the thickness dependence of the amorphous-to-crystalline phase transition kinetics.

The above experiments clearly demonstrate that the CCl_4 is trapped beneath the ice until the phase transition occurs, and that desorption occurs in a dramatic fashion in concert with the crystallization of amorphous ice. Detailed modeling of the phase transition kinetics show that the rapid CCl_4 desorption occurs when a threshold fraction of the amorphous solid water has crystallized. Further details about the structural dynamics occurring in the amorphous material can be obtained by studying the CCl_4 desorption as a function of the water overlayer thickness and substrate temperature.

References

1. R. J. Speedy, P. G. Debenedetti, R. S. Smith, C. Huang, and B. D. Kay, *J. Chem. Phys.* **105**, 240–244 (1996).
2. M. Fisher and J. P. Devlin, *J. Phys. Chem.* **99**, 11584 (1995).
3. D. E. Brown, S. M. George, C. Huang, E. K. L. Wong, K. B. Rider, R. S. Smith, and B. D. Kay, *J. Phys. Chem.* **100**, 4988–4993 (1996).
4. R. S. Smith, C. Huang, E. K. L. Wong, and B. D. Kay, *Surf. Sci. Lett.* **367**, L13–L18 (1996).

Chemisorption on Oxide Surfaces

M. J. Stirniman, C. Huang,**
R. S. Smith, S. A. Joyce, and B. D. Kay

Supported by DOE Office of Basic Energy Sciences.

*Postdoctoral Research Associate.

The objective of this program is to examine chemical phenomena occurring at model oxide surfaces. Oxide interfaces are important in the subsurface environment; specifically, molecular-level interactions at mineral surfaces are responsible for the transport and reactivity of subsurface contaminants at Hanford. Unfortunately, our molecular-level understanding of oxide surface chemistry is severely lacking. Initial experiments will focus on the dissociative chemisorption dynamics of halogenated hydrocarbons (CCl_4, $CHCl_3$, CH_2Cl_2, CH_3Cl), H_2O, CH_3OH, NH_3, and HCl on model oxide surfaces (MgO, SiO_2, Al_2O_3). These studies employ variable-energy supersonic molecular beams to determine energy-, angle-, and coverage-dependent trapping and/or dissociation probabilities. In addition to using bulk single-crystal

samples, techniques such as molecular beam epitaxy and/or chemical vapor deposition will be explored to grow epitaxial thin oxide films on single-crystal metallic substrates. The successful synthesis of such crystalline thin oxide films will enable the entire arsenal of electron-based surface analytical techniques to be applied to the characterization of these nonconducting materials.

Chemisorption of H_2O, CH_3OH, and NH_3 on Single-Crystal MgO (100)

Adsorption at surfaces of metal oxides has recently been the focus of considerable experimental attention, in part due to the wide-ranging importance of these materials in environmental and industrial processes. Metal oxides are often used as catalysts or as supports for catalysts, making the interaction of adsorbates with their surfaces of much interest. In addition, metal oxides are increasingly being used in other industrial applications, such as materials for gas sensors and electronic devices. Due to the presence of charge separation, adsorption at an ionic oxide surface can be intrinsically different from adsorption at a metal surface, in that it allows the possibility of acid–base and electron donor–acceptor types of interactions. Polar molecules can be useful probes of these surfaces, yielding information on the nature of the adsorption sites, as well on the energetics of adsorption and desorption. In fact, ammonia is often used as a basic probe molecule to infer the acid–base properties of catalysts. Unfortunately, these catalysts are usually well-dispersed powders with strongly heterogeneous, high-area surfaces, which complicates the interpretation of the TPD results. As a result, there is a need for more basic studies of polar molecule–ionic surface interactions, using well-characterized single-crystal oxide surfaces. As one of the best-studied oxide surfaces, MgO (100) has been described as a model of such interfaces and is in many ways ideally suited to these types of investigations. MgO has a single valence state cation, a simple cubic rocksalt structure, and only one thermally stable surface, the (100) plane.

Adsorption of water, ammonia, and methanol on MgO has been of considerable recent interest, and a great deal of progress has been made in understanding the nature of the surface adsorption sites and the bonding of such polar molecules at those sites. However, questions remain as to the absolute coverage, adsorption mechanism, and desorption kinetics. Recent results from our laboratory have shown that the absolute coverage of water in the monolayer (ML) on MgO (100) is approximately one water molecule per surface unit cell, that the desorption activation energy is on the order of 15 kcal/mol, and that the adsorption kinetics are precursor mediated.[1] We have extended our studies to include experiments using calibrated molecular-beam dosing in conjunction with TPD that similarly quantify the coverage of ammonia and methanol in the surface monolayer on MgO (100). In addition, molecular beam reflection techniques are used to obtain information on the mechanism of the adsorption process, and TPD on the energetics and kinetics of the desorption process. The differences in desorption activation energy for the three adsorbates lend insight into their bonding interactions with the ionic MgO (100) surface, and individual trends in desorption activation energy as a function of coverage provide information on the interadsorbate interactions in the surface-adsorbed layers.

Figure 2.16 shows results obtained from a beam reflection experiment. In this experiment, the molecular beam is incident on the sample, and the fraction of the incident beam that is reflected or desorbs is detected by the quadrupole mass spectrometer. Using the known flux of the beam, the data are easily inverted to yield the condensation coefficient versus coverage shown in the figure. The top panel shows data obtained from our earlier study on the adsorption and desorption of D_2O from the MgO (100) surface,[1] while the center and bottom panels are equivalent results for CH_3OH and ND_3. Because of the differences in coverage at saturation of the monolayer for each adsorbate, the coverages are reported in terms of adsorbates per surface unit cell of the substrate MgO (100) lattice. These data demonstrate the markedly non-Langmuirian adsorption kinetics for these three molecules on this surface. In each case, the apparent sticking coefficient is very nearly unity, independent of coverage, almost to saturation of the adsorbate monolayer. This behavior is usually attributed to the adsorption of the incident molecule into a mobile precursor state prior to chemisorption, and these results show that precursor-mediated adsorption may be a general mechanism for polar adsorbates on ionic surfaces.

In contrast to water, the saturation coverages for CH_3OH and ND_3 are less than one adsorbate

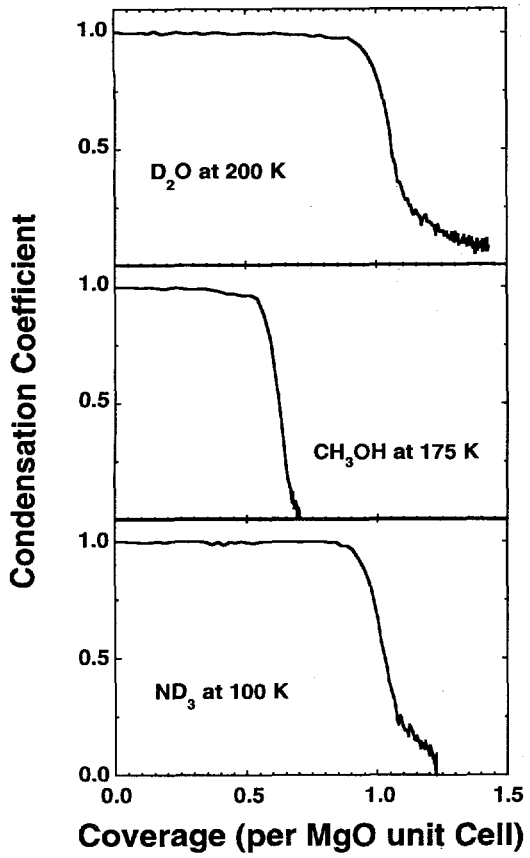

Figure 2.16. Experimental condensation coefficients for the three adsorbates vs. the surface coverage at the temperatures indicated, determined using the molecular beam reflection method. The coverages are reported in absolute terms, referenced to the MgO (100) substrate unit cell.

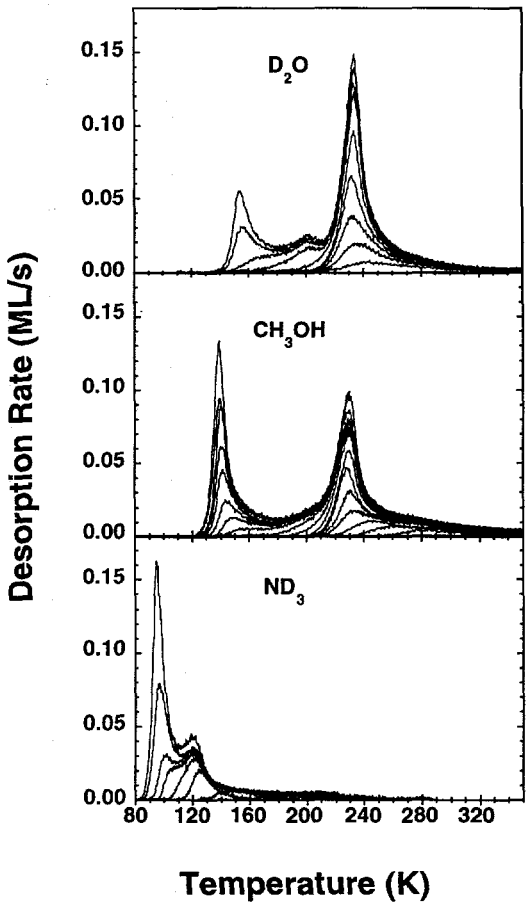

Figure 2.17. Families of TPD curves for the three adsorbates for varying initial coverages.

molecule per surface unit cell, and in the case of ND_3 the monolayer coverage is somewhat arbitrary. The adsorbate coverages were determined from TPD experiments in which the sample was dosed to varying initial coverages. In general, for each adsorbate there is a sufficiently low temperature below which the condensation coefficient remains unity indefinitely. Subsequent desorption of the adsorbate will typically result in two or more peaks in the TPD spectrum, with the lowest-temperature peak corresponding to sublimation of the adsorbate multilayer, and higher-temperature peaks to desorption from the monolayer adsorbed directly on the substrate. Figure 2.17 shows a family of TPD curves for each of the adsorbates, for varying initial coverage. In the case of D_2O and CH_3OH, the multilayer peaks and monolayer peaks are well separated, and the monolayer peak is observed to saturate before the multilayer peak begins to form. This allows the coverage in the adsorbate monolayer at saturation to be determined from the two initial coverage curves just before and just after the multilayer peak appears. As reported in our earlier study,[1] for water this coverage is approximately 1.00 ± 0.10 water molecule per surface unit cell, and a similar determination for CH_3OH yields a monolayer saturation coverage of 0.58 ± 0.03 molecules per surface unit cell. The monolayer coverage of ND_3, on the other hand, is slightly less clear. As can be seen in the bottom panel of Fig. 2.17, the monolayer and multilayer desorption features are partially overlapped. Despite this complication, we have chosen to define the monolayer saturation coverage in the same manner as for D_2O and CH_3OH, which results in a value of 0.70 ± 0.08 molecules per surface unit cell for ND_3.

The differences in saturation coverage for monolayers of D_2O and CH_3OH can be rationalized by a simple steric argument. In going from a hydrogen to a methyl group, the size of the adsorbate would be expected to approximately double, and the saturation coverage should be halved. On the other hand, the lower absolute coverage in the ND_3 monolayer is probably more a result of repulsive intermolecular interactions. A qualitative understanding of the strengths of the adsorbate-substrate interactions can be obtained from simple inspection of the TPD curves in Fig. 2.17. TPD of D_2O and CH_3OH results in almost identical curves, indicating that the desorption activation energies for these two adsorbates are very similar in both the multilayers and in the monolayers. Zero-order leading edge analysis of the multilayer peaks yields desorption activation energies of 11.8 and 10.4 kcal/mol for D_2O and CH_3OH, respectively. The corresponding heats of sublimation (at standard pressure) for bulk crystalline water and bulk methanol are 11.15 and 9.18 kcal/mol, respectively. Quantitative analysis of the TPD spectra yield first-order desorption activation energies of about 15 kcal/mol for both the CH_3OH and D_2O monolayers. In contrast, both the multilayer and monolayer peak for ND_3 occur at a much lower temperature than for the other two adsorbates. Quantitative analysis of the ammonia multilayer peak yields a desorption activation energy consistent with the heat of sublimation of ammonia. The fact that the monolayer of ammonia is bound significantly less strongly than water or methanol is somewhat more informative. This is in marked contrast to elementary chemical intuition based on the concept of Lewis acidity/basicity. Numerous recent theoretical studies indicate that the ammonia–MgO interaction does not involve the electron donation from nitrogen lone pairs to the Mg^{2+} site that would be expected in a Lewis acid-base reaction. In all three systems the binding is dominated by electrostatic interactions involving minimal charge transfer between the adsorbate and substrate. This type of bonding is characteristic of physisorption rather than molecular chemisorption.

Kinetics of Incipient Rehydration of MgO

In aqueous environments, many metal oxides are thermodynamically unstable with respect to the formation of metal hydroxides. Such rehydration may play an important role in the dissolution of minerals and glassy and ceramic waste forms. Understanding the mechanism and kinetics of the dissolution process are requisite to determining the suitability of materials targeted for the long-term storage of radioactive waste. The MgO–water system is an excellent model system for examining the rehydration process, because $Mg(OH)_2$ (brucite) is thermodynamically favored over MgO (periclase). Despite the favorable thermodynamics, the kinetics of brucite formation are sluggish and poorly understood. During the course of our previous studies on the water–MgO (100) system,[1] we observed that the desorption kinetics were sensitive to surface defects, and that the sticking coefficients determined by the beam reflectivity technique did not vanish for water coverages above surface saturation.

Apparent sticking coefficients as a function of surface coverage and temperature are displayed in Fig. 2.18. The data clearly demonstrate that the adsorption kinetics on this surface are markedly non-Langmuirian. The apparent sticking coefficient remains near unity up to the temperature-dependent saturation coverage, consistent with precursor-mediated adsorption. At temperatures below 150 K, extended dosing results in the formation of a nonsaturable multilayer ice film. Above 170 K, it is not possible to form multilayer ice with the beam fluxes employed. The maximum water coverage prior to the onset of ice formation is 1.3 ± 0.1 ML, where we define 1 ML as the coverage necessary to occupy every surface

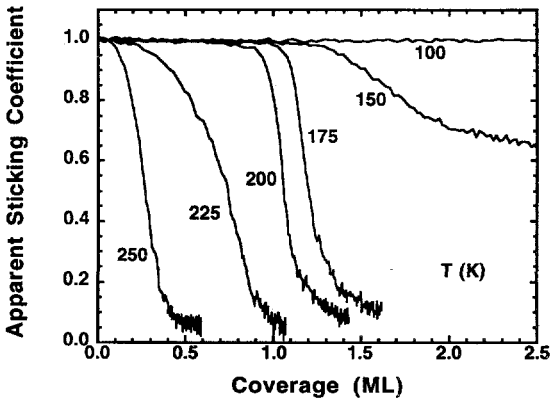

Figure 2.18. Apparent sticking coefficient versus coverage from beam reflectivity experiments on a sample that had been sputtered and annealed at 1100 K. The sample was dosed at each temperature for 60 seconds at a flux of ca. 6×10^{13} molecules/cm^{2}sec.

unit cell on MgO (100) (1.13×10^{15} cm^{-2}) with a single water molecule. At temperatures above 300 K, the apparent sticking coefficient is close to zero. However, it has been shown that an apparent sticking coefficient that decreases with increasing surface temperature can result from the competition between adsorption and desorption, and we believe this to be the case in the present study. Note that at 175 K and above, the apparent sticking coefficients displayed in Fig. 2.18, while decreasing rapidly, do not go to zero. We believe this is due to the incipient stage of the hydration of bulk MgO (periclase) to form the thermodynamically favored $Mg(OH)_2$ (brucite).

We have determined that this nonzero apparent sticking coefficient persists for dose times up to three hours, the longest dose attempted, and further, that the magnitude of the apparent sticking coefficient is dependent upon the sample preparation procedures; *i.e.*, the apparent sticking is greater on samples that had been sputtered than on samples that had been cleaned only by high-temperature annealing in oxygen. With this in mind, further experiments were performed using the molecular beam to dose the sample at temperatures above those at which the monolayer was observed to desorb. Figure 2.19 shows representative TPD spectra obtained after extended dosing at a surface temperature of 250 K, compared to the desorption trace obtained from a 1-ML dose of water at 100 K. At 250 K and with this incident flux, the steady-state surface coverage of water should be on the order of 0.2–0.3 ML.

Figure 2.20 is a plot of the integrated area of the TPD curves from the doses at 250 K as a function of the dose time, showing that a 30-minute dose at this flux results in the desorption of the equivalent of 6–7 ML of water. Numerous control and blank experiments were run to confirm that the observation was not due to adsorption of background water on other surfaces (*e.g.*, the sample manipulator or sample heater leads). Simple geometric arguments and an estimation of the extent of surface diffusion during the time of the experiments preclude the possibility that this is purely a surface desorption phenomenon. The fact that the desorption features appear to be nonsaturable, and that the desorption temperature of these features is a function of the dosing temperature also argue against the possibility of extensive surface diffusion. This evidence leads us to the conclusion that water is absorbed into the bulk of the oxide sample during these experiments.

The solid line in Fig. 2.20 is a nonlinear least squares fit to the data using a function proportional to the square root of the dose time. The dependence of the uptake on the square root of the exposure time suggests that the uptake of water in this regime is in fact a diffusion-limited process. As shown in Fig. 2.20, the uptake rate also increases as the surface defect concentration increases, suggesting that the surface defect sites provide the kinetic doorway leading to bulk

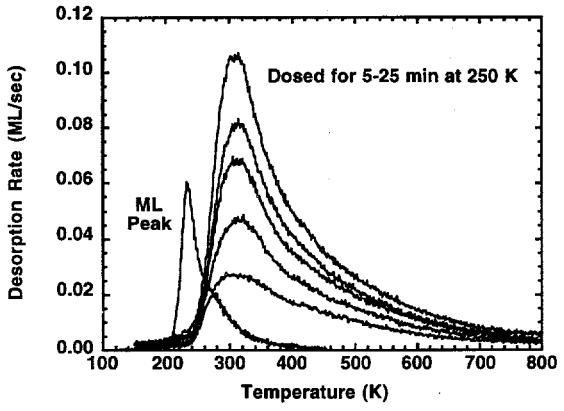

Figure 2.19. Water TPD spectra resulting from extended dosing of the MgO (100) sample at 250 K. The area under the TPD curves increase monotonically with increasing dose time, yielding coverages vastly in excess of 1 ML. A TPD trace corresponding to a 100-K dose of 1 ML is shown for comparison.

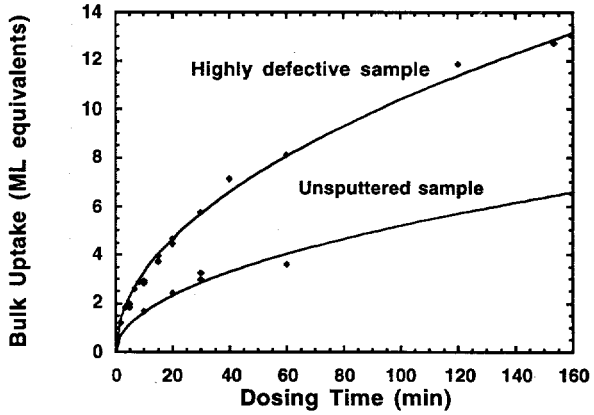

Figure 2.20. Bulk water uptake as a function of dosing time. The uptake yields a $t^{1/2}$ dependence on dose time and is enhanced by the presence of surface defects.

hydroxylation. An Arrhenius analysis of the uptake as a function of the sample temperature for constant dose times yields an apparent activation energy of –2.7 kcal/mol. An apparent negative activation energy can be interpreted as a competition between two elementary steps: the rate of desorption from the defect sites and the rate of the initial entry into the bulk of the oxide. In this temperature regime the uptake rate scales linearly with the incident beam flux. Such a relationship indicates that if the defect sites are indeed the channel responsible for the uptake of water into the bulk of the crystal, they remain unsaturated at the fluxes and temperatures employed here.

Taken as a whole, the data presented above lead to a consistent picture of diffusion-mediated absorption of water into the bulk of the MgO single crystal. This bulk diffusion is responsible for the high-temperature tails observed during desorption of water from sputtered MgO samples,[1] as well as for the anomalous nonzero sticking coefficients observed during beam reflection experiments at surface temperatures above the desorption temperature of the monolayer. The question of the nature of the absorbed water remains, however. We are currently modeling the coupled surface, defect, and bulk-diffusion kinetics. Based on thermochemical data, we believe we are forming brucite, $Mg(OH)_2$. The enthalpy of formation of $Mg(OH)_2$ from solid MgO and gas-phase water is exothermic by 19 kcal/mol, whereas our TPD results indicate that the adsorption of water on the surface of MgO is exothermic by about 15 kcal/mole, assuming a desorption prefactor of 10^{13}/sec. If one assumes a desorption prefactor of 10^{16}/sec, however, the formation of the surface-adsorbed species and the hydroxide become nearly isoenergetic. Further experiments aimed at verifying this hypothesis will be performed on new instrumentation currently under construction. This instrumentation enables the vibrational spectrum of the adsorbed and absorbed species to be monitored during beam dosing and thermal processing.

Reference

1. M. J. Stirniman, C. Huang, R. S. Smith, S. A. Joyce, and B. D. Kay, "The Adsorption and Desorption of Water on MgO (100): The Role of Surface Defects," *J. Chem. Phys.* **105**, 1295–1298 (1996).

Synthetic Ionic Interfaces via Ion-Beam and Ice Epitaxy

A. A. Tsekouras, G. B. Ellison,† J. P. Cowin, and M. J. Iedema*

Supported by DOE Office of Basic Energy Sciences.

*Visiting Scientist.
†University of Colorado.

The majority of contaminants at DOE sites are in ionic form (salts), and their transport in soils, separations from tanks, or remediation involve ionic reactions at surfaces of minerals or other materials. An approach has been developed to re-create these interfaces under laboratory control to elucidate reaction mechanisms. A very low energy ion beam, with high brightness, mass selection, and capability for both positive and negative molecular ions, has been built in collaboration with Professor G. B. Ellison of the University of Colorado.[1] This beam, combined with ice–epitaxial methods, allows tailor-making water–solid interfaces with ions.

Ice interfaces have been demonstrated to be a good model for liquid water reactions, because most of the chemical interactions are much stronger than the melting/freezing energies of water, and transport is not a problem for the 10–1000-nm ice films used in these studies. The ion source must deliver 10 nA or more of ions at no more than a few eV of kinetic energy to prevent high-energy damage to the ions or the aqueous interface under construction. The source must be mass-selected so one can choose just the ions or isotopes desired for study, and it must supply important aqueous-type ions, such as hydronium (H_3O^+), ammonium (NH_4^+), simple metal ions such as cesium or sodium, anions like OH^-, Cl^-, OCl^-, HCO_3^-, NO_3^-, and such ions with waters of hydration attached. A Wien mass filter was coupled to a novel short ion decelerator, and to a versatile supersonic jet electron-impact ion source, with superb differential pumping. We have demonstrated hydronium and ammonium ions, and a similar source at the University of Colorado has produced bright molecular anions, including several of those listed above.

A simple experiment showing the importance of the low-energy capability was conducted for water ions (D_2O^+) impacting on a clean Pt (111) surface.[2]

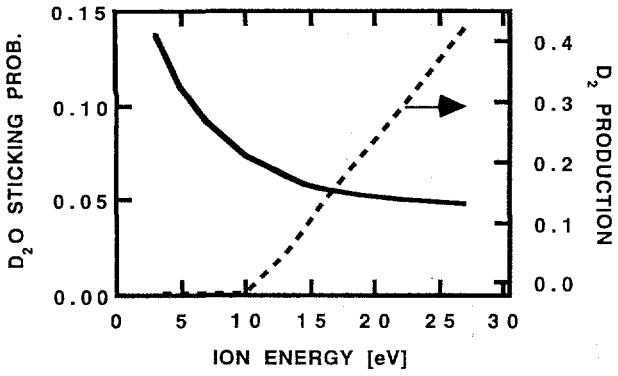

Figure 2.21. D_2O^+ deposition and D_2 production vs. beam energy.

Figure 2.21 shows the probability of the ion adsorbing intact instead of simply bouncing (solid curve) or dissociating on impact to eventually produce deuterium molecules (dashed curve). At 3 eV, the probability of intact adsorption is 0.14, and the impact-induced damage is zero. By 10 eV, the ion intact adsorption probability drops dramatically, and damage (dissociation) commences. This is a simple demonstration that for controlled ion deposition, ion beams with at most a few eV of kinetic energy are crucial, and this new apparatus has this capability.

The impact-induced dissociation of the water ion at the surface commencing above 10 eV is *not* accompanied by oxygen adsorption. We understand this in terms of an impulsive collision with the surface, whereby the oxygen atom bounces off the stiff Pt lattice with high probability, oblivious to the fate of the light deuteriums. Above 10 eV, enough internal energy is produced in the impulsive collision to break the deuterium–oxygen bonds and form new ones with the surface.

Studies in progress explore adding ions into and onto solvent ice films to simulate the ionic processes and charge transfer in aqueous and organic systems. For a "simple" system, we chose to drop Cs^+ ions on frozen hexane films. This is relevant to DOE needs, for radioactive cesium is a major problem in nuclear waste management, and extraction into organic solvents like hexane (though typically via a complexing agent) is an established method of separating Cs from aqueous wastes. The Cs^+ energy is kept at or below 2 eV, slowly ramping the sample bias to compensate for charging of the hexane film. We measure the charging (and thus the charge-weighted average height of the ions in the films) using a Kelvin probe to measure work function changes. We find that at 30 K, films from 12 to 125 monolayers act like nearly perfect capacitors, with a dielectric constant not too different from the 1.9 value seen for liquid hexane. The "capacitor" can be charged up to only 3 V for the thinnest film, and as much as 14 V for the thickest. A sharp voltage threshold exists for the charge transfer, and we are working to determine if this process is electron transfer or some sort of irreversible field-triggered ion diffusion.

Once these films have been made, we can follow the charge transfer as a function of temperature. This is shown in Fig. 2.22 for two films of 38 monolayers of hexane, one amorphous and one probably crystalline (annealed at 120 K for 2 minutes). The Cs^+ charge is 0.4 μA on about 1 cm^2, or about 0.002 monolayer of Cs^+. The temperature is ramped at 0.333 K/s. The results are shown in terms of the net work function of the sample (which is bare work function minus film potential drop). Note that the work function can initially be near zero or even negative. We find that visible light causes measurable electron emission from these systems, a possible topic for future studies.

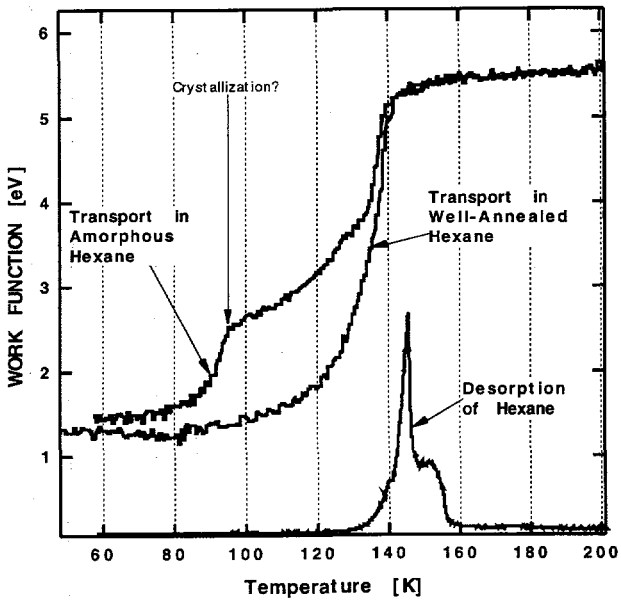

Figure 2.22. Charge transport in 38-monolayer-thick hexane ices. Cs^+ ions (0.002 ML) on top of the film initially bias it, measured by a work function probe. Amorphous hexane conducts much better than crystalline.

As the film is heated, eventually the hexane will desorb, near 150 K. Before it desorbs, charge flow occurs. We see that amorphous hexane allows charge flow much more easily than crystalline hexane. Near 95 K, the amorphous hexane makes a transition to a crystalline-like state with lower charge transfer rates.

We find that the charge flow does not depend on the generated electric field strength in at least the crystalline hexane for thicker coverages (work in progress). This indicates that simple field-assisted ion diffusion (ion mobility) does not apply. We are probing the charge-transfer mechanism with additional experiments in progress.

We are planning experiments involving hydronium on/in water. Proton-tunneling effects on diffusion will be explored using normal and deuterated water. For water, the structural and temperature behavior of its dielectric constant also are of interest and will be measured.

References

1. J. P. Biesecker, G. B. Ellison, H. Wang, M. J. Iedema, A. A. Tsekouras, and J. P. Cowin, *Rev. Sci. Instrum.*, to be submitted.
2. H. Wang, J. P Biesecker, M. J. Iedema, G. B. Ellison, and J. P. Cowin, *Surf. Sci.*, in press.

Transport of Molecules Across the Liquid/Vapor Interface of Water

D. S. Karpovich,* A. G. Joly, G. R. Holtom, J. L. Daschbach,† and D. Ray

Supported by DOE Office of Basic Energy Sciences and the EMSL Project.

*Postdoctoral Research Associate.
†EMSL Interfacial and Processing Science.

The goal of this work is the direct spectroscopic measurement of the thermochemistry and kinetics of mass transfer across the liquid water/vapor interface. The detailed, molecular-level data obtained from these experiments, along with molecular-scale simulations performed by staff in the Theory, Modeling, and Simulation program, will provide improved understanding of the uptake of gases by aqueous solutions, and may furnish an alternative method to determine mass accommodation coefficients of atmospherically important species.

The basic experimental approach is to measure the orientation, the adsorption isotherm, and the solvation kinetics of selected adsorbates on liquid water surfaces. These measurements will be made by surface second-harmonic generation spectroscopy, using a high repetition rate femtosecond laser and a photon-counting detection system, or by surface sum-frequency generation using a tunable picosecond infrared optical parametric generator.

The transport of dimethyl sulfoxide (DMSO) across the liquid/vapor interface is currently under study. At equilibrium (*e.g.*, in the closed static cell used in these experiments), the partitioning of DMSO between the gas phase, the liquid phase, and the liquid/vapor interface is completely determined by the solvation energy and the adsorption energy. The solvation energy can be determined from the previously measured Henry's Law constant.[1] The adsorption energy has been determined in our experiments.

Calculation of the transport properties on a potential energy surface that reproduces the thermochemical data is underway. Additional interface-specific measurements are also in progress, and will allow critical examination of models proposed for the uptake of gases by liquid surfaces.

Reference

1. S. F. Watts and P. Brimblecombe, *Env. Tech. Lett.* 8, 483 (1987).

Single-Molecule Spectroscopy and Dynamics at Room Temperature

H. P. Lu, J. D. Chesko, and X. S. Xie*

Supported by DOE Office of Basic Energy Sciences.

*Postdoctoral Research Associate.

Chemists rely on spectroscopic measurements on large ensembles of molecules to identify molecular species and to monitor chemical changes. While the ensemble-averaged measurements are essential, they often preclude detailed information, especially in the case of condensed media where there exists heterogeneity of molecular environments and constant fluctuations of molecular properties. In the wake of recent advances in single-molecule fluorescence microscopy and spectroscopy,[1] the complication of spectral inhomogeneity can be avoided and single-molecule spectral fluctuation can be monitored in real time.[2,3] Figure 2.23 shows a sequence of emission spectra of a single sulforhodamine 101 molecule on a quartz surface, recorded with 170-ms collection times at room temperature. The surprisingly large spectral shifts at the rather long time scale contain detailed information regarding the intramolecular and intermolecular interactions and dynamics.[2]

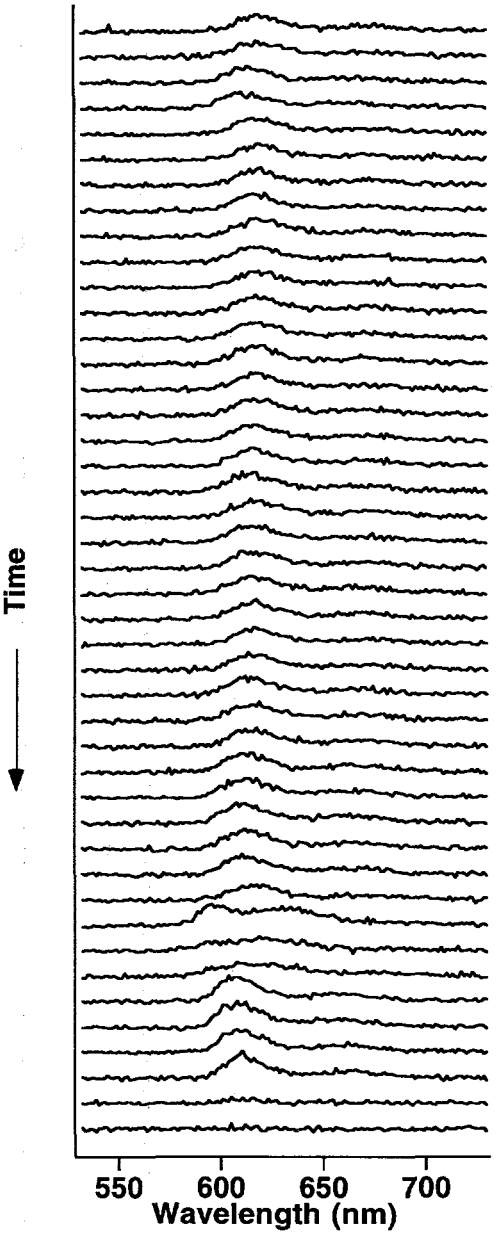

Figure 2.23. Emission spectra of a single sulforhodamine 101 molecule taken sequentially with 532-nm excitation and 170-ms data collection times before it is finally photobleached. Significant spectral shifts are evident during the course of measurement (from Ref. 2).

To analyze the spectral fluctuations on a statistical basis, we evaluated the autocorrelation function $C(t) = \langle \nu(0)\nu(t)\rangle - \langle \nu\rangle^2$ of single-molecule spectral trajectories, ν being the spectral mean in wavenumbers. Figure 2.24(A) displays such a $C(t)$, a double exponential decay with the rates for the fast and slow components being $k_1 = 1.85\ s^{-1}$ and $k_2 = 0.022\ s^{-1}$, respectively. The inset in Fig. 2.24(A) shows the distribution of the spectral means accessed by the single molecule in the specific local environment. We observed similar spectral fluctuations for every molecule examined within a large population. Molecules in different local environments have spectral mean distributions significantly different in center positions as well as in widths.

Although we observed a small propensity for dipole reorientation, it is too infrequent to account for these spectral fluctuations. We attribute the spectral fluctuations to changes of either intramolecular (such as conformational changes of a side chain) or intermolecular nuclear coordinates (such as hydrogen bonds or collective nuclear motions in the interacting environment). The observation that the $C(t)$ of the single molecule is double exponential implies that there exist at least two quasi-independent variations in nuclear coordinates taking place with different rates (k_1 and k_2).

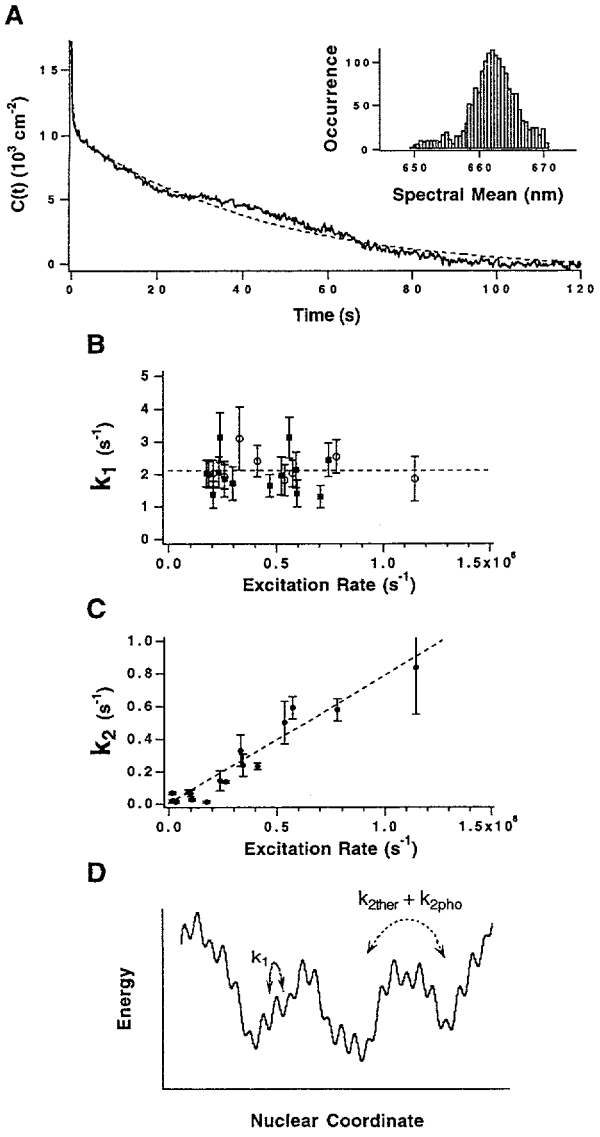

Figure 2.24. (A) Autocorrelation function of the spectral mean, derived from the spectral trajectory of a single sulforhodamine 101 molecule at an excitation rate of 2.6×10^5 ct/s at 594 nm. Dashed line: a fit with a double exponential,

$$C(t) = \sigma_1^2 \exp(-k_1 t) + \sigma_2^2 \exp(-k_2 t),$$

for $t > 0$ ($k_1 = 1.85\ s^{-1}$, $k_2 = 0.022\ s^{-1}$, $\sigma_1^2 = 5000\ cm^{-2}$, $\sigma_2^2 = 10{,}700\ cm^{-2}$). Inset: distribution of spectral means accessed by the single molecule in the specific local environment. (B) k_1 as function of excitation rate at 594 nm (squares) and 532 nm (circles). Independent of the excitation rate and wavelength, the fast spectral fluctuation is spontaneous. (C) k_2 as a function of excitation rate at 532 nm. The linear relationship shows that the slow spectral fluctuation is dominated by photo-induced fluctuation. (D) Schematic of the molecular potential energy surface of the nuclear coordinates (from Ref. 2).

For each type of variation of nuclear coordinates, both spectral diffusion and photo-induced fluctuation are possible. In evaluating many trajectories, we observed that (1) the fast component (k_1) is independent of excitation rate and excitation wavelength (Fig. 2.24(B)), which indicates that the fast component is a spontaneous spectral fluctuation (known as spectral diffusion); and (2) the slow component (k_2) is dependent on excitation rate (Fig. 2.24(C)) and excitation wavelength, which clearly indicates that the slow component is dominated by photo-induced fluctuation (k_{2pho}). The rate of spectral diffusion in the same nuclear coordinate, $k_{2ther} = k_2 - k_{2pho}$, is difficult to obtain by extrapolating to the zero excitation rate in Fig. 2.24(C). However, k_{2ther} has been determined to be $0.02 \pm 0.01\ s^{-1}$ by a scheme in which the excitation light is periodically blocked for a period of "dark time" after each spectrum collection, waiting for spectral diffusion to occur.[2]

The spectral diffusion at the rates of k_1 and k_{2ther} would have been extremely difficult, if not impossible, to detect at room temperature in ensemble-averaged experiments. The spectral diffusion indicates two distinctly different types of barrier heights in the molecular potential energy surface. We attribute the fast component to variations of intermolecular coordinates, and the slow components to variations of intramolecular coordinates. As shown in a simplified one-dimensional cross section of the molecular potential surface, (Fig. 2.24(D)), the small barriers between the minima of intermolecular potential can be accessed easily through thermally activated fluctuation (k_1), whereas the large gross barriers between the minima of intramolecular potential can be accessed only through photoexcitation (k_{2pho}) and much slower thermally activated fluctuation (k_{2ther}). The temperature dependence of the thermal fluctuations are being determined to obtain the activation energies. Similar spectral trajectory analyses of a single fluorophore in a protein is being studied, which will allow detailed investigation of conformational dynamics and energy landscapes for a specific active site and their influence on enzymatic reactions.

The repetitive excitations ($<10^7$/s) single-molecule experiments do not permit monitoring single-molecule trajectories in real time on the picosecond and nanosecond time scale. For a repeatable photoinduced process, however, measurements of single-molecule fluorescence lifetime using ultra-

fast pulse trains allow determination of the temporal survival probability of an excited state on this time scale.[4,5] This makes it possible to study photoinduced chemical reactions of single molecules in specific local environments. Figure 2.25(A) shows the fluorescence decay of a single cresyl violet molecule adsorbed on an indium-tin-oxide (ITO) surface.[6] Upon excitation, this molecule injects an electron into the conduction band or energetically accessible surface electronic states of ITO. The kinetics of this interfacial electron transfer is determined by the fluorescence decay, which is a single exponential decay with a time constant of 480 ps. Interestingly, we find a wide distribution of electron transfer rates for individual molecules at different sites, Fig. 2.25(B). Based on Fig. 2.25(B), measurements made on large ensembles of molecules would have more than 20 exponentials, which is impossible to resolve in practice. Our single-molecule results indicated that the multiexponential behavior of this system arises from the heterogeneity of the "static" sites. This illustrates that single-molecule measurements are capable of providing much more detailed information than ensemble-averaged measurements.

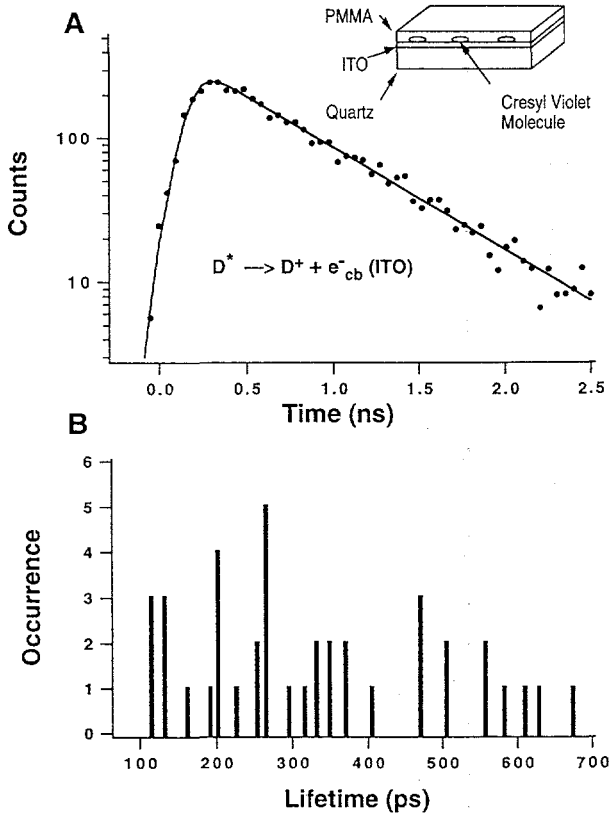

Figure 2.25. (A) The fluorescence decay of a single cresyl violet molecule dispersed on an ITO film. The fast decay is due to interfacial electron transfer from the excited molecule (D*) to the conduction band of ITO. The solid line is a single exponential fit (480 ps) convoluted with the instrumental response function. (B) Histogram of emission lifetimes for 40 different molecules examined, revealing a broad distribution of site-specific electron transfer kinetics.[6]

References

1. For reviews, see W. E. Moerner, *Acc. Chem. Res.* **29**, 563 (1996); X. S. Xie, *Acc. Chem. Res.* **29**, 598 (1996).
2. H. P. Lu and X. S. Xie, *Nature* **385**, 143 (1997).
3. J. K. Trautman *et al.*, *Nature* **369**, 40 (1994).
4. X. S. Xie and R. C. Dunn, *Science* **265**, 361 (1994).
5. J. J. Macklin *et al.*, *Science* **272**, 255 (1996).
6. H. P. Lu and X. S. Xie, *J. Phys. Chem.*, in press.

Single-Molecule Studies of Flavoenzymes

*X. S. Xie, H. P. Lu, and L. Xun**

Supported by Laboratory Directed Research and Development (LDRD).

*Washington State University.

Flavoproteins are ubiquitous in nature because of their capabilities to undergo redox reactions in a thermodynamically and kinetically fully reversible manner. Their enzymatic reactions not only facilitate various electron transfers in our bodies, but are also involved in biodegradation.

For example, the high mobility of radionuclides complexed with chelating agents such as nitrilotriacetate (NTA) represents a major environmental concern at DOE sites. Biodegradation of chelating agents by microorganisms can help immobilize radionuclides in the environment. Recently, an NTA monooxygenase from a microorganism was purified and characterized, and the corresponding gene cloned and sequenced, providing an opportunity for molecular-level understanding of the biodegradation process.[1] Flavin mononucleotide (FMN) is involved in the redox reactions of this enzyme and activating O_2.

The molecular structure of FMN is shown in Fig. 2.26. There has been extensive spectroscopic work done on FMN and related compounds. The oxidized form of FMN is naturally fluorescent, whereas the reduced form ($FMNH_2$) is not. FMN has an absorption peak at 440 nm and emission peak at 500–560 nm. The emission spectra depend strongly on the solvent polarity, pH, etc., providing a good probe for reaction intermediates. A single-molecule experiment is capable of capturing short-lived reaction intermediates that are otherwise difficult to observe because of their low steady-state concentrations.

Figure 2.27 shows the emission spectrum of a single FMN imbedded in a PMMA film taken in 3 seconds using a combination of a spectrograph and a back-illuminated CCD camera. Spectra for individual molecules are distinctly different (20-nm fwhm in distribution) due to different local environments. More interestingly, we observed spectral fluctuations of the single FMN molecules on the sub-second time scale, similar to those observed for dye molecules.[2] This initial experiment demonstrated the feasibility of spectroscopic measurements on individual flavoproteins.

Another biodegradation enzyme, pentachlorophenol-4-monooxygenase, is a 60-kDa enzyme that converts pentachlorophenol to tetrachloro-*p*-hydroquinone.[3] Its active site is flavin adenine dinucleotide (FAD, a derivative of FMN), which is naturally fluorescent in its oxidized form. Figure 2.28 shows a far-field fluorescence image of single flavoproteins immobilized in an agarose gel of 98% water.[4] Each spot corresponds to a single enzyme with a single fluorescent FAD cofactor. Single molecules were evidenced by polarized emission and the sudden, quantified disappearance of the signal due to photobleaching. Each diffraction-limited peak (fwhm 340 nm) is due to a

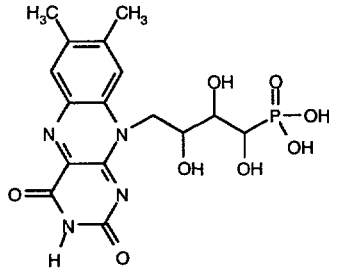

Figure 2.26. Chemical structure of FMN.

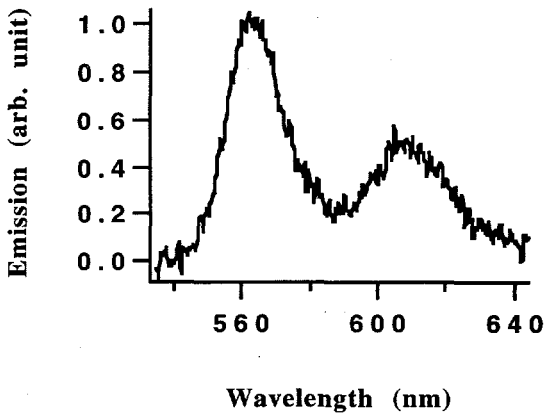

Figure 2.27. Emission spectrum of a single FMN embedded in a PMMA film.

single FAD. Different intensities are due to different molecular orientations and single-molecule spectra. We are recording and analyzing spectral trajectories of the single FADs, which will provide detailed information regarding conformational dynamics and energy landscapes. Spectral fluctuations on the time scale of enzymatic turnovers can influence the kinetics of enzymatic reaction.

References

1. Y. Xu *et al., J. Bacteriol.*, in press.
2. H. P. Lu and X. S. Xie, *Nature* **385**, 143 (1997).
3. L. Xun, E. Topp, and C. S. Orser, *J. Bacteriol.* **174**, 5745 (1992).
4. X. S. Xie, *Acc. Chem. Res.* **29**, 598 (1996).

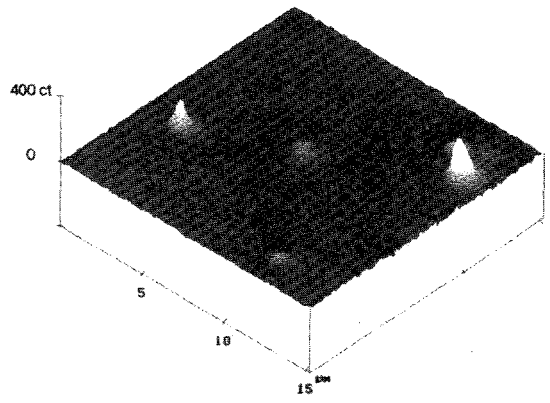

Figure 2.28. A far-field fluorescence image of single proteins of pentachlorophenol-4-monooxygenase demobilized in a thin film of agarose gel of 98% water. Each protein contains an active site, FAD, which is naturally fluorescent in its reduced form. The FAD fluorescence was excited with 488-nm light.

Nonlinear Optical Imaging

E. J. Sanchez, L. Novotny,†*
G. R. Holtom, and X. S. Xie

Supported by Cooperative Research and Development Agreement (CRADA).

*Portland State University graduate student.
†Postdoctoral Research Associate.

In fluorescence microscopy, two-photon excitation of molecular fluorescence has advantages of reduced excitation volume, effective rejection of background, and easy access to UV transitions. Recently, detection of single molecules in the solution phase using two-photon excitation in a fluorescence microscope has been demonstrated.[1]

Using an inverted fluorescence microscope, we obtained high-quality two-photon fluorescence images of immobilized single fluorophores (rhodamine B, sulforhodamine 101, and coumarin 535 on polymethyl methacrylate films) and photosynthetic membrane fragments by raster scanning the sample with respect to a diffraction-limited focus of a mode-locked Ti:sapphire laser beam. Figure 2.29 shows the two-photon fluorescence image of single rhodamine B molecules. The signal-to-background ratio was as high as 50:1, and the full width at half maximum (250 nm) of a single-molecule peak is significantly shorter than that for one-photon excitation. The high sensitivity and simplicity of the two-photon experiment provide a valuable approach for spectroscopic studies on individual immobilized molecules.

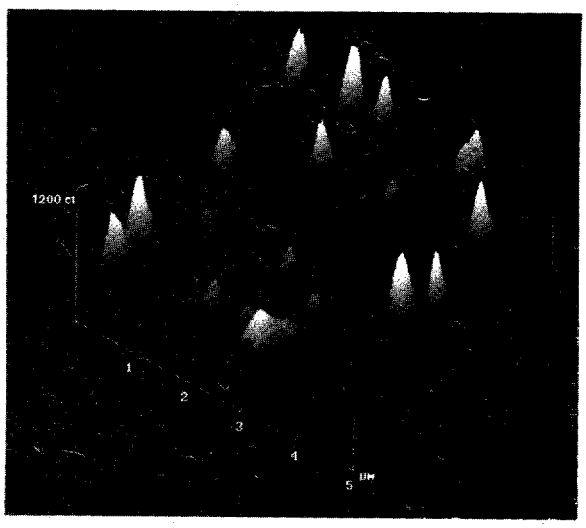

Figure 2.29. Fluorescence images of rhodamine B molecules on a PMMA film obtained using two-photon excitation induced by femtosecond pulses from a Ti:sapphire laser.

With the goal of extending the high-resolution microscopy work to the infrared region, we have also started an effort on vibrational imaging in the chemically important 3-μm wavelength region by using sum-frequency mixing of femtosecond pulses from an infrared optical parametric amplifier[2] and a Ti:sapphire regenerative amplifier.

References

1. J. Mertz, C. Xu, and W. W. Webb, *Optics Lett.* **20**, 2532 (1995).
2. G. R. Holtom, R. A. Crowell, and X. S. Xie, *J. Opt. Soc. Am. B.* **12**, 1723 (1995).

3. Radiation and Other High-Energy Processes at Environmental Interfaces

Photostimulated Desorption of CO from Geologic Calcite Following 193-nm Irradiation

K. M. Beck, D. P. Taylor, and W. P. Hess*

Supported by DOE Office of Basic Energy Sciences and the Strategic Environmental Research and Development Program.

*Postdoctoral Research Associate.

Calcium carbonate ($CaCO_3$) is an environmentally significant mineral that exists in several forms, including orthorhombic aragonite, rhombohedral dolomite, and rhombohedral calcite. The carbonates as a group make up more than 10% of the Earth's sedimentary mass,[1] and calcite itself is present in the soil to the extent that it influences subsurface transport of heavy metals through interactions with groundwater. Calcium carbonate is also a component in the protective caliche layer below the waste storage tanks at the Hanford site. Our immediate interest in calcium carbonate, and molecular ionic compounds in general, arises from the need to perform micro-sample chemical analysis of hazardous wastes in soils. Laser ablation mass spectrometry (LAMS) is an analytical technique being developed for this purpose. The LAMS technique has been successfully applied to complex solid and doped glass samples for quantitative elemental analysis.[2] But for LAMS analysis to be effective here, desorption properties of these molecular ionic components must be understood.[3] In this study we focus on laser desorption following 6.42-eV (193-nm) excitation of calcite and examine laser/solid interactions following excitation of single-crystal calcium carbonate by measuring the translational, rotational, and vibrational energy distributions of desorbed CO.

The experimental apparatus consists of an ultrahigh vacuum chamber equipped with a laser tier, access ports, and quadrupole (QMS) and time-of-flight (TOF) mass spectrometers. Desorbed neutral species may be ionized by a second laser for TOF detection or by electron impact (70 eV) for QMS detection. The sample manipulator also has the capability to rotate the sample about the z-axis, may be cooled to near liquid nitrogen temperatures (90 K), and includes a button heater and thermocouples pressure-mounted to the crystal sample for heating and monitoring. The $CaCO_3$ crystals are irradiated with 5-ns pulses of 193-nm excimer laser emission (100 $\mu J/cm^2$) incident on the sample at 50° normal to the crystal face. The single crystal emits an orange luminescence at the point of irradiation that we use to orient and center the sample within the excitation beam. For the detection of CO we have chosen (2+1) resonance-enhanced multiphoton ionization (REMPI).[4,5] The (2+1) process involves two-photon excitation of the $B^1\Sigma \leftarrow\leftarrow X^1\Sigma$ transition, followed by one-photon ionization from the B-state to the ion ground electronic state. The (2+1) spectrum is characterized by a strong Q branch obtained over a narrow frequency range of ~20 cm^{-1}. Subsequent analysis of the Q branch then affords insight into the rotational product state distribution.[6]

At very low excitation laser fluences, the principal neutral desorption product from calcite is CO. Figure 3.1 displays the QMS signal of neutral species desorbed from calcite. CO dominates other constituents by an order of magnitude. But even after accounting for "cracking" within the electron impact ionizer, distinct signals are apparent for

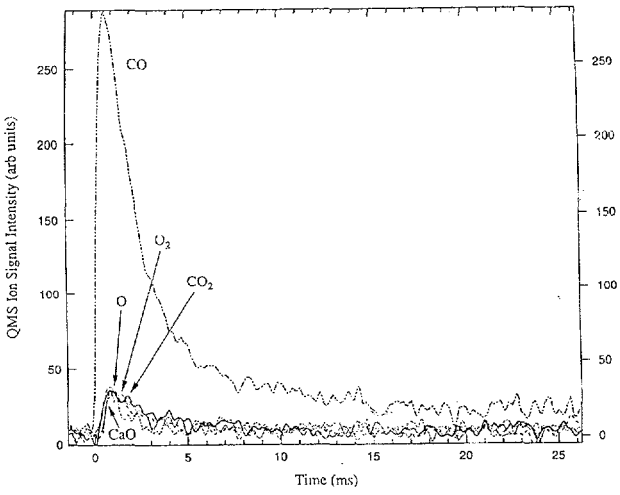

Figure 3.1. QMS ion signals of neutral products desorbed from 193-nm irradiation of geologic calcite: CO, O, O_2, CO_2, CaO. Ions of the neutral products are formed following 70-eV electron bombardment. Corrections to the recorded signals have been made for CO fragmentation (CO, 100%; O, 6.1%; C, 10%).

CaO, O, CO_2, and O_2. At these low pump laser fluences, the TOF-MS detects no CO cation or other ion signal. We conducted power dependence studies of the desorption process at fluences up to ~0.6 mJ/cm^2. CO was detected following electron-impact ionization using the quadrupole mass spectrometer, and we found that a single-photon absorption process leads to molecular desorption of CO from calcite.

Approximately 6% of the desorbed CO contains a single quantum of vibrational energy (2140 cm^{-1}). Investigation of higher vibrational levels of $B^1\Sigma$ state CO is hampered because their rate of predissociation is larger than for ionization. A two-point Boltzmann distribution with a 6% $v = 1$ vibrational population yields a temperature of 1100 K. In contrast, we find the CO velocity distribution to be quite slow and well characterized by a temperature well below that of the substrate. Figure 3.2 represents the velocity distributions of desorbed CO for $Q(J) = 5$ at a substrate temperature of 295 K for $v = 0$. The TOF spectra are fit to a half-range Maxwell-Boltzmann velocity distribution function.[7] The TOF spectra for $v = 0$ can be fit with a translational temperature $T_{trans} = 110 \pm 15$ K.

Figure 3.3 displays the resolved Q branch for the CO (0,0) $B^1\Sigma \leftarrow\leftarrow X^1\Sigma$ and (1,1) $B^1\Sigma \leftarrow\leftarrow X^1\Sigma$ transitions obtained following photostimulated desorption (PSD) from room-temperature $CaCO_3$. The appearance of Q-branch structure is not unexpected since the difference between the X state ($v = 0$, $B = 1.931$ cm^{-1}) and B state ($v = 0$, $B = 1.948$ cm^{-1}) rotational constants causes a splitting of Q-branch transitions that increases with J. This splitting is greater than the combined Doppler and laser bandwidths for $Q(J) > 7$ and approaches 1.0 cm^{-1} for $Q(J) = 20$. Superimposed upon these scans are spectra simulating a thermal distribution at 295 K for CO rotational states up to $Q(J) = 23$. The rotational spectra of CO products, in contrast to the translational energy, appears similar to a thermal simulation at the substrate temperature of 295 K. However, a nonthermal component is also revealed in the rotational spectra. Specifically, the spectrum for $v = 0$ appears "structurally" nonthermal. A stepwise effect may be seen with popu: below thermal at low $Q(J)$, above thermal at mid $Q(J)$, and again below thermal at higher $Q(J)$.

Experimental determination of the state-resolved distribution of CO desorbed from calcite provides a detailed view of the product energy available in the photostimulated desorption process. It is usual for the products observed in most photostimulated desorption experiments to be emitted either thermalized to the surface temperature, or

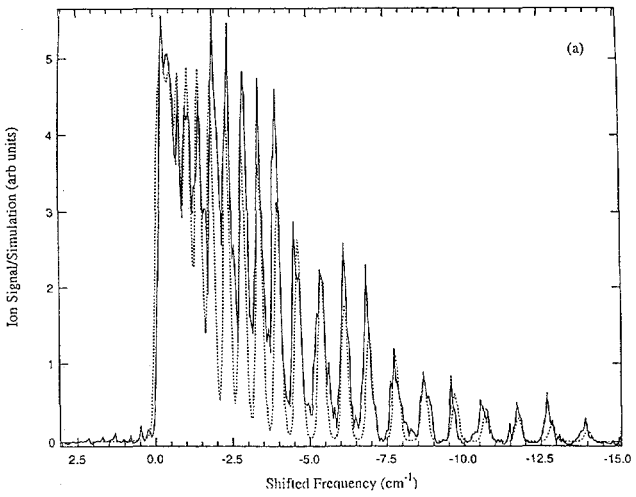

Figure 3.3. Rotationally-resolved Q-branch spectra of desorbed CO. The (2+1) REMPI scheme contains the entire Q branch within a narrow frequency range of < 20 cm^{-1}. The frequency scale is shifted such that the $Q(J) = 0$ transition is located at the band origin. The solid and dashed lines represent the recorded spectra, and the simulated fits (295 K), respectively.

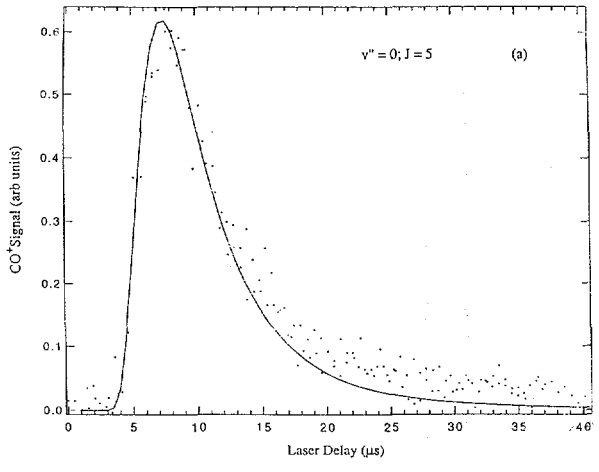

Figure 3.2. Velocity dependence of CO desorbed from $CaCO_3$ monitored via (2+1) REMPI of the $Q(5)$ transition at progressive laser delays. The data can be fit to a translational temperature, T_{trans} = 110 ± 15 K, using a half-range Maxwell-Boltzmann velocity distribution function.

with a high translational energy, but in this work the photodesorbed CO is translationally cold. Subthermal desorption distributions are rare, and we know of no reported case where the translational energy of desorbing molecules is as low as 1/3 of the surface temperature. It seems unlikely that an equilibrium thermal desorption process could account for this phenomena. For example, one argument for "cold" thermal desorption would be that if energy equilibrium of an adsorbate with the surface occurs through small energy increments ($<<kT$), the final small increment would then put the energy above the vacuum level, resulting in low translational motion. This implies a very steeply falling sticking probability with increasing temperature. The intermediate species formed during PSD of calcite are not known, and for now the dynamics of CO formation are shrouded in the complexity of the surface dissociation. It is likely, however, that the CO, once formed, does not stay near the surface long enough to exchange much energy with the surface. The low translational energy would then reflect the energetics of the CO formation. The nonthermal product distributions we observe provide evidence that the product did not remain on the surface long enough to equilibrate. This likely indicates that a surface species or state is involved in the desorption process, and could suggest that excitations involving surface electronic states are involved.

In photostimulated desorption, it is expected that the translational motion is the degree of freedom most easily thermalized. Yet the key feature of our results is the subthermal CO translational motion. This is inconsistent with the high translational energy associated with desorption from a dissociative surface excited state based on the conceptual picture in the Menzel-Gomer-Redhead (MGR) model.[8,9] The MGR model supposes that photoexcitation leads to formation of a "molecular" excited state significantly perturbed from its equilibrium position. The resulting lattice distortion then couples a significant fraction of the photon energy into nuclear motion and eventually into translation of the atomic or molecular desorbate. Any such model that proposes channeling of excess electronic energy into product translation necessarily predicts velocities much higher than we measure here. Therefore, the qualitative dynamical picture that arises is one of a gentle reactive scattering, viewed as the *last half* of a full molecule/surface collision.

References

1. K. H. Wedepohl, *Handbook of Geochemistry* (Springer-Verlag, Berlin, 1969), **1**:250-270.
2. M. L. Alexander, M. R. Smith, D. Koppenaal, and J. Hartman, "Laser Ablation ICP/MS Analysis of Low-Level Hanford Tank Waste Simulants: Optimizing Experimental Parameters" (Rocky Mountain Analytical Conference, Denver, 1995).
3. R. A. Bradley, E. Lanzendorf, M. I. McCarthy, T. M. Orlando, and W. P. Hess, *J. Phys. Chem.* **99**, 11715–11721 (1995).
4. G. W. Loge, J. J. Tiee, and F. B. Wampler, *J. Chem. Phys.* **79**, 196 (1986).
5. P. J. H. Tjossem and K. C. Smyth, *J. Chem. Phys.* **91**, 2041 (1989).
6. K. M. Beck, K. A. H. German, and W. P. Hess, *Chem. Phys. Lett.* **256**, 297 (1996).
7. R. Kelly and R. W. Dreyfus, *Surf. Sci.* **198**, 263 (1988).
8. D. Menzel and R. Gomer, *J. Chem. Phys.* **41**, 3311 (1964).
9. P. A. Redhead, *Can. J. Phys.* **42**, 886 (1964).

Mass Spectrometry of Low-Molecular-Weight Solids by Matrix-Assisted Laser Desorption/Ionization

S. C. Goheen, K. L. Wahl,* J. A. Campbell,* and W. P. Hess*

Supported by DOE Office of Basic Energy Sciences and the Strategic Environmental Research and Development Program.

*Environmental and Health Sciences Division, Materials and Chemical Sciences Department.

Matrix-assisted laser desorption/ionization (MALDI) was designed to overcome the limitations of laser desorption ionization and provide a simple method for introducing high-molecular-weight (HMW) species directly into the gas phase in both neutral and ionic form. Using MALDI, the mass spectrometry of very large polymers, biomolecules, and a variety of thermally nonlabile materials has been accomplished with many studies focusing on extending the high-mass regime, with masses in the range 150,000 to 250,000 amu detected.[1-3] An experimental advantage of target-

ing high-mass analytes is that the analyte mass is many times greater than the mass of the matrix molecules, so the two species seldom interfere. The prospect of such interferences is significant, as the optimum matrix-to-analyte molar ratio is usually high, on the order 1,000–10,000 to 1.[4] A few recent MALDI studies have focused on medium to low-molecular-weight nonvolatile compounds.[5–8] Our interest in extending MALDI to analysis of complex mixtures of low-molecular-weight (LMW) molecules is derived from the need for speciation of mixed hazardous wastes.

We have used MALDI time-of-flight (TOF) mass spectrometry to examine anions, organic acids, and chelators including EDTA, HEDTA, citric acid, NTA, and the inorganic anions sulfate, phosphate, nitrate, and nitrite. In addition, we performed MALDI on mixtures of these molecules to reflect the combinations of compounds found in complex mixed wastes and to consider the technical aspects of low and high molecular weight MALDI. Data were obtained using a commercial linear TOF instrument with a nominal mass resolution of $m/\Delta m$ = 600, positive- and negative-ion detection modes, and a channeltron ion detector. An internal 337-nm nitrogen laser of 3-ns pulse duration was used to induce the desorption/ionization process. The laser was focused to a rectangular spot 200 μm × 100 μm at the sample tray. Laser power was varied using a calibrated attenuator; power was generally set to a range between 40% and 80% above the threshold for ion appearance. Both positive and negative ions are produced during MALDI, and the two channels often provide complementary information. We used 2,5-dihydroxybenzoic acid (DHB) as the matrix for all analysis of LMW species. In most cases the DHB matrix was dissolved in water to a concentration of 10 mg/mL to produce a nearly saturated solution. Analyte molecules were dissolved in water to the same concentration and combined, in various proportions, with the matrix solution. One (1.0) microliter of sample was applied to each spot on the sample tray.

Figure 3.4 shows the positive ion MALDI spectrum of EDTA, displaying multiple sodium adducts $[M + nNa]^+$. At lower m/z, strong ion signals attributable to the DHB matrix are observed; $[DHB - OH]^+$ at m/z = 137, $[DHB + H]^+$ at m/z = 155, and $[DHB + Na]^+$ at m/z = 177. Figure 3.5 shows the negative-ion MALDI mass spectrum of

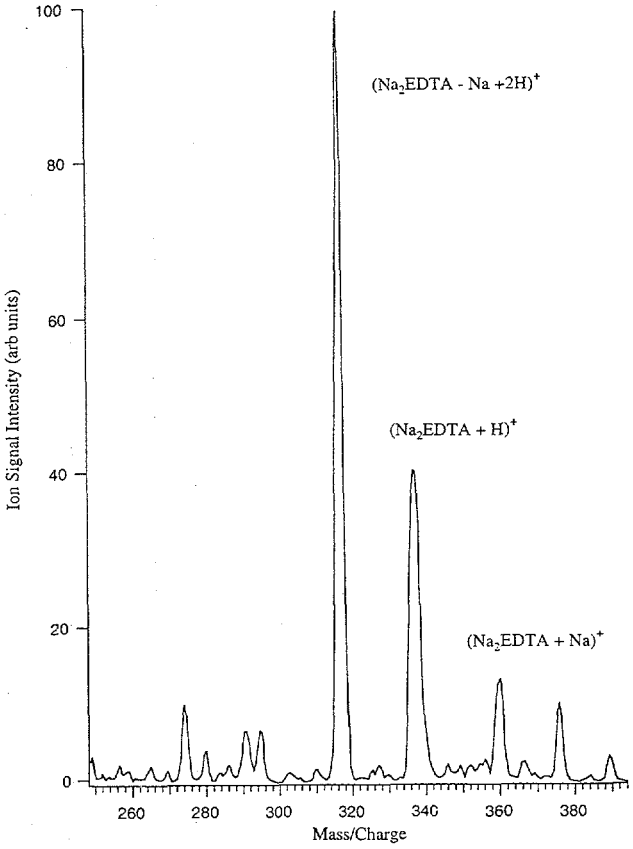

Figure 3.4. Positive-ion MALDI spectra for EDTA in DHB at a matrix-to-analyte molar ratio of 100:1. Note the progression of sodiated peaks at m/z = 315, 337, and 359. The peaks at m/z = 137, 155, and 177 are attributed to ionized matrix species.

citric acid. The strong negative-ion signal is attributed to the deprotonated parent molecule $[M - H]^-$ at m/z = 191. Figure 3.5 illustrates how little matrix interference can be present in the negative-ion detection mode, as only a single strong matrix peak at m/z = 153, $[DHB - H]^-$, is observed.

The analytes studied and the m/z values and assignments of the ions observed in positive- and negative-ion MALDI are shown in Table 1. Inspection of Table 1 reveals an interesting feature: the amine-based chelating compounds yield strong signals in the positive-ion mode, while the small organic acids and oxyanions yield strong signals in the negative-ion mode. This effect is most easily rationalized on the basis of relative acidities and ion stabilities. The acidity of an organic acid is due to the stability of its anion; the more stable the anion the stronger the acid. The strong negative-ion signals observed for organic acids are

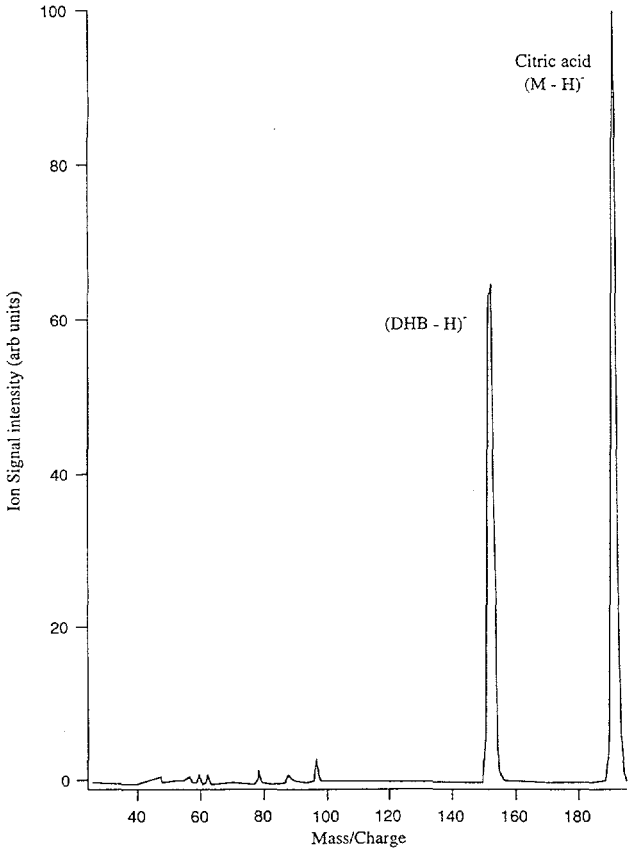

Figure 3.5. Negative-ion MALDI mass spectrum for citric acid in DHB matrix. The "clean" mass spectrum displays only two significant peaks, the $[M - H]^-$ base peak at m/z = 191 and the single matrix base peak $[DHB - H]^-$ at m/z = 153.

likewise a result of the stability of the acid anions. Similarly, the stable oxyanions nitrate, nitrite, and hydrogen sulfate display strong signals in negative-ion MALDI. Chelating compounds such as EDTA form stable positive ions by adduction of a proton (or Na^+) to the basic amine functional groups.

Hazardous waste is often a very complex mixture containing dozens of compounds. It was anticipated that multiple analytes might interfere with one another, or that some analytes would preferentially associate with the matrix, resulting in poor sensitivity. Figure 3.6 shows the negative-ion MALDI spectrum of a relatively equimolar mixture of citric acid, oxalic acid, ammonium sulfate, and sodium nitrate with DHB matrix. All four analytes are readily observable, although the nitrate ion signal at m/z = 62 is considerably weaker than the three other analyte ion signals. Weak nitrate ion

Table 1. Positive and Negative Ions Observed by MALDI-TOF MS

Analyte	Mol. Wt.	Ions Observed (m/z)	
		(–)	
Sodium nitrate	85	62 $[NO_3]^-$	
Sodium nitrite	69	46 $[NO_2]^-$	
Oxalic acid	90	89 $[M - H]^-$	
Fumaric acid	116	115 $[M - H]^-$	
Maleic acid	116	115 $[M - H]^-$	
Succinic acid	118	117 $[M - H]^-$	
Ammon. sulfate	132	97 $[HSO_4]^-$	
Citric acid	192	191 $[M - H]^-$	
		(+)	
HEDTA	278	279 $[M + H]^+$	301 $[M + Na]^+$
NTA	191	192 $[M + H]^+$	214 $[M + Na]^+$
EDTA	292	293 $[M + H]^+$	315 $[M + Na]^+$
		337 $[M + 2Na]^+$	359 $[M + 3Na]^+$

intensity is a common feature that has been observed with other similar mixtures.

Although many MALDI studies of HMW species have been completed, few studies of small molecules have been reported. Low molecular weight but thermally nonlabile species, while amenable to MALDI analysis, provide unique challenges, and significant technical differences exist between the low- and high-mass regimes. The most significant difference is that the masses of matrix ions, including dimers and fragments, are similar to analyte masses, and interferences between matrix and analyte can be significant. The chemistry of large and small molecules provides another significant difference between the two mass regimes. Many HMW biomolecules contain several acidic and basic functional groups. The amphoteric nature of the large molecules results in MALDI signals in both negative- and positive-ion channels. For smaller molecules, either the positive- or negative-ion channel will likely be favored.

In studies of small proteins and peptides, Zhu *et al.*[6] found that the positive-ion MALDI signal was strongly enhanced by the presence of basic amino acids in the chain. In that work, it was suggested that a proton is transferred, in solution, from a matrix molecule to a basic amino acid by an acid–base reaction, thus providing a low-energy mechanism for ionization. The concept of preformed solid-phase ions leading to gas ion products by

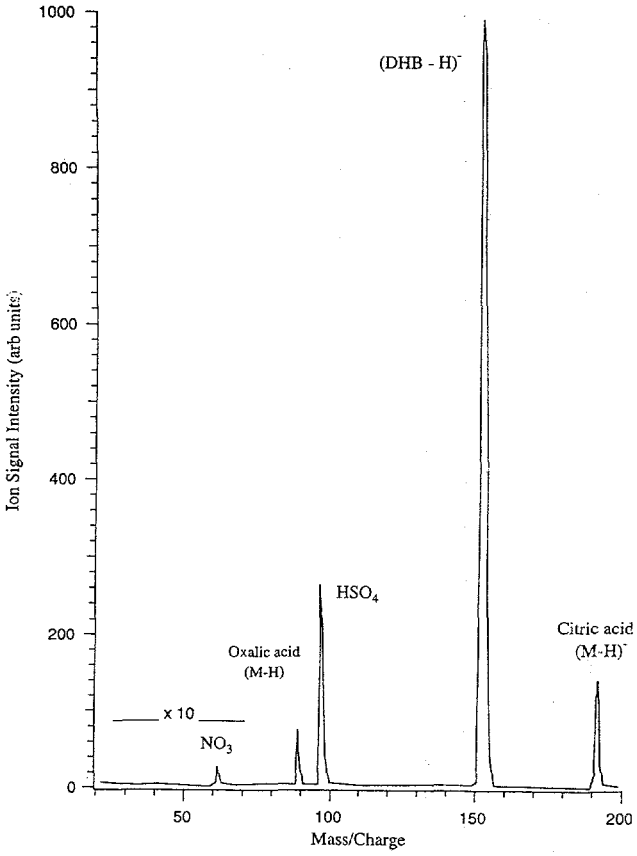

Figure 3.6. Negative-ion MALDI spectrum of the analyte mixture consisting of equimolar concentrations of ammonium nitrate, oxalic acid, ammonium sulfate, citric acid, and DHB matrix. It is notable that all four analytes produce strong signals, although the intensity NO_3^- peak is significantly weaker than for the sulfate or organic acid analytes.

direct desorption has been discussed in fast atom bombardment (FAB) literature. It is thought that an enhanced response is observed because only desorption of the ion need occur and no ionization step is required.[9] Liao and Allison have recently extended these FAB concepts to matrix-assisted laser desorption analysis by demonstrating enhanced response for triphenylphosphium-derivatized peptides in a α-cyano-4-hydroxycinnamic acid matrix.

We varied initial sample pH to determine the effect on positive- and negative-ion modes for HEDTA and citric acid analytes, respectively. A strong base peak is observed for citric acid in the negative-ion channel at $m/z = 191$. Ions indicative of HEDTA were observed as $[M + H]^+$ at $m/z = 279$ and the $[M + Na]^+$ ion at $m/z = 301$. The differences in the relative intensities of the ions from the different pH solutions were less apparent than for citric acid. Clearly, ionization mode had an effect on which analytes were observed, but the solution pH had limited effect on the ionization efficiency of these two analytes. Because the range of pH covered in this study spans the pKa of the analytes, this implies that a pre-proton-transfer mechanism is not responsible for ionization in these molecules, as one would expect pre-proton transfer to decrease with pH. Our results indicate that the oxidation state of the analyte is not a strong factor in determining ion yield.

References

1. M. Karas and F. Hillenkamp, *Anal. Chem.* **60,** 2299 (1988).
2. K. Tanaka, H. Waki, Y. Ido, S. Akita, Y. Yoshida, and T. Yoshida, *Rapid Commun. Mass Spectrom.* **2,** 151 (1988).
3. M. Karas, A. Ingendoh, U. Bahr, and F. Hillenkamp, *Biomed. Environ. Mass Spectrom.* **18,** 841 (1989).
4. F. Hillenkamp, M. Karas, R. C. Beavis, and B. T. Chait, *Anal. Chem.* **63,** 1193A (1991).
5. E. Schroeder, H. Muenster, A. Overberg, and I. Merfort, *42nd ASMS Conference of Mass Spectrometry* (Chicago, 1994), p. 939.
6. Y. F. Zhu, K. L. Lee, K. Tang, S. L. Allman, N. I. Taranenko, and C. H. Chen, *Rapid Commun. Mass Spectrom.* **9,** 1315 (1995).
7. R. Lidgard and M. W. Duncan, *Rapid Commun. Mass Spectrom.* **9,** 128 (1995).
8. M. G. Bartlett, K. L. Busch, C. A. Wells, and K. L. Schey, *J. Mass Spectrom.* **31,** 275 (1996).
9. P. C. Liao and J. Allison, *J. Mass Spectrom.* **30,** 511 (1995).

Infrared Polarization Study of the Ultraviolet Photolysis of Condensed-Phase Acetyl Chloride

B. Rowland and W. P. Hess*

Supported by DOE Office of Basic Energy Sciences.

*Postdoctoral Research Associate.

Understanding the differences between photoreaction of gas- and condensed-phase molecules is vital to understanding chemical events and processes on heterogeneous surfaces or occurring within particles found in the atmosphere.[1] Gas-phase photodissociation experiments have reached such a sophisticated level that the molecular dynamics are often studied in exquisite detail. Much less knowledge exists for reactions in the condensed phase; nonetheless, the details of condensed-phase reactivity are often more relevant to environmental concerns. We are studying the condensed-phase ultraviolet (UV) photodynamics of environmentally relevant molecules to better delineate the chemical dynamics important to these systems.

Distinct differences exist between the UV photodissociation dynamics of acetyl chloride in the gas and condensed phases.[2,3] Photodissociation of gas-phase acetyl chloride molecules by 235-nm light produces Cl and acetyl radicals ($CH_3CO\cdot$) that further dissociate into CH_3 and CO.[2,4] Chlorine is promptly ejected from photoexcited acetyl chloride with an average translational energy of 9.9 kcal/mol. The mean internal energy within the acetyl radical is 19 kcal/mol, which is large enough to break the weak C–C bond. Thus, the UV photoreaction of acid aldehydes differs from the expected Norrish type I reaction observed for asymmetrically substituted aldehydes and ketones.[5] For a Norrish type I reaction the weaker C–C bond is expected to break over the stronger C–Cl bond in accordance with RRKM theory.

Photoreaction of condensed-phase acetyl chloride produces HCl and ketene molecules, products unseen in the primary gas-phase photoreaction. There are two reaction mechanisms that have been considered for the condensed-phase photoreaction: direct elimination and a caged abstraction.[3] The direct elimination mechanism produces HCl·ketene complexes through a concerted process on an electronic surface distinct from that of the gas-phase dissociation. Such an elimination mechanism would likely lead to aligned HCl·ketene product complexes that are well correlated to the polarization axis of the incident irradiating laser. We have use polarized infrared (IR) spectroscopy to aid in distinguishing between elimination and caged abstraction mechanisms.

Thin films of matrix-isolated acetyl chloride (500:1, Ar:CH_3COCl) are vapor-deposited onto a KBr substrate mounted on a closed-cycle helium cryostat at 11 K. Deposits of xenon-matrix–isolated acetyl chloride samples (300:1, Xe:CH_3COCl) are similarly prepared onto a substrate cooled to 20 K. The films are irradiated for 1 to 2 minutes using the 266-nm fourth harmonic of a linearly polarized Nd:YAG laser with an average pulse energy of 0.3 mJ at a 20-Hz repetition rate. The thickness of the argon deposits is monitored using optical interference measurements with a 633-nm helium–neon laser. Such measurement can not be made for Xe matrices because the refractive index of the Xe matrix and KBr substrate are nearly equal.

Infrared spectra are collected before and after irradiation at a resolution of 2 cm^{-1} using a Mattson 10000 Fourier transform infrared (FTIR) spectrometer. Polarized IR spectra are obtained by inserting an IR polarizer between the IR source and condensed sample. The orientation of the HCl·ketene complex is analyzed by collecting background, preirradiated IR spectra, and post-irradiated spectra at 45° increments of the IR polarizer. By subtracting background spectra at each polarization, any systematic artifact due to polarization-sensitive optics within the FTIR spectrometer is removed.

The IR spectrum of HCl·ketene complexes formed by irradiation of acetyl chloride molecules isolated in argon is displayed in Fig. 3.7. Acetyl chloride is identified by the intense C=O stretch at 1808 cm^{-1}, and the photoproducts are identified by the strong bands at 2730 cm^{-1} (HCl) and 2100 cm^{-1} (C=O stretch). Identical photoproducts are observed in neat films and Xe matrix-isolated acetyl chloride samples. No other primary photoproducts are observed. Small amounts of secondary products such as CH_3Cl and CO are observed in Ar-matrix–isolated acetyl chloride, but only after extensive UV irradiation at 266 nm.

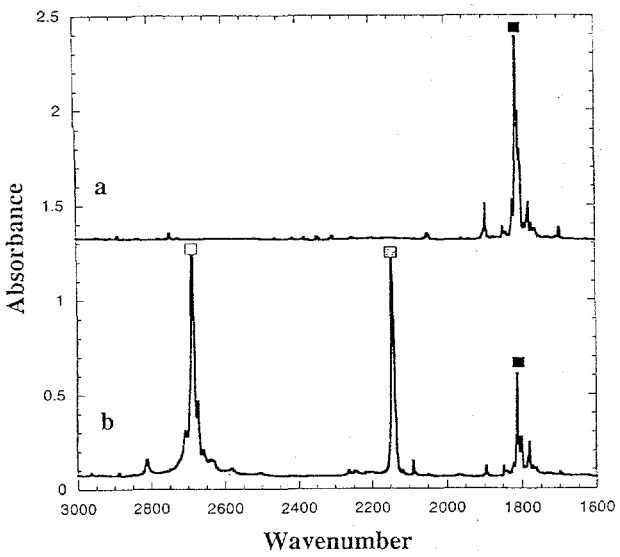

Figure 3.7. Infrared spectra of matrix-isolated (argon, 500:1) acetyl chloride for pre-irradiated (a) and post-irradiated (b) samples at ~11 K. The C=O stretch of acetyl chloride, the C=O stretch of ketene, and the HCl stretch are designated by black, gray, and white filled square markers, respectively.

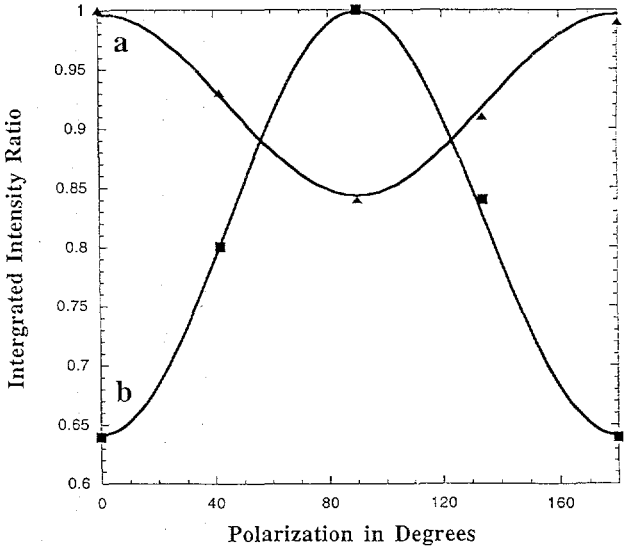

Figure 3.8. The IR polarization dependence of the integrated IR intensities of product HCl (a) and ketene (C=O stretch) (b); IR spectra were taken at ~11 K for an irradiated deposit of matrix-isolated acetyl chloride (argon, 500:1). The thin film was irradiated using a vertically-polarized UV laser (θ = 0 in the laboratory frame).

Alignment data of the vibrational dipoles of ketene and HCl are displayed in Fig. 3.8. The data are fit using a $\cos^2\theta$ distribution that yields photoproduct orientation relative to each other and to the vertically polarized excitation laser (laboratory frame). The geometry of the ketene·HCl complex is determined from the $\cos^2\theta$ fits, such that the HCl molecule is located above the plane of the ketene molecule, oriented nearly perpendicular, at a 92° angle. The geometry of the products can also be inferred by comparing the alignment data of the vibrational dipoles of acetyl chloride with the net vibrational dipoles determined by *ab initio* calculations. This indicates that the hydrogen end of HCl is located near the methylenic carbon, and the chlorine is tilted toward the alkyl carbon.

The ketene·HCl complex is formed following UV irradiation of condensed-phase acetyl chloride by a direct elimination reaction. Our data provide no support for the possibility of a stepwise caged-abstraction mechanism. The exclusive production of HCl·ketene complexes, their distinct alignment relative to the polarization axis of the irradiating laser, and the lack of CH_3Cl and acetyl radical products all argue strongly against any contribution by a caged-abstraction mechanism.

References

1. M. J. Molina, L. T. Molina, and D. M. Golden, *J. Phys. Chem.* **100**, 12888 (1996).
2. S. Deshmukh, J. D. Myers, S. S. Xantheas, and W. P. Hess, *J. Phys. Chem.* **98**, 12535 (1994).
3. B. Rowland and W. P. Hess, *Chem. Phys. Lett.* **263**, 574 (1996).
4. S. Deshmukh and W. P. Hess, *J. Chem. Phys.* **100**, 6429 (1994).
5. M. D. Person, P. W. Kash, and L. J. Butler, *J. Chem. Phys.* **97**, 355 (1992).

Plasma and Materials Chemistry Approach to Treatment of Automotive Exhaust

R. G. Tonkyn, S. E. Barlow, M. L. Balmer, D. Goulette,† and T. M. Orlando*

Supported by Cooperative Research and Development Agreement (CRADA) with USCAR.

*EMSL Interfacial and Processing Science.
†Delphi Energy and Engine Management Systems, Flint, Michigan

Current catalytic converter technology for automobile exhaust treatment provides inefficient reduction of NO_x under oxidizing conditions. To meet emissions standards, the engine must be run at stoichiometric or even fuel-rich conditions. By operating the engine under lean-burn conditions (high air/fuel ratio), up to 6% of the vehicle fuel could be conserved. Unfortunately, the resulting exhaust stream is highly oxidative, and current "3-way" catalytic converters are ineffective for NO_x removal.

The nonthermal barrier discharge approach to emissions treatment is an attractive alternative (or supplemental) technology that has the potential to overcome the technical problems associated with more conventional catalysts. Theoretical and experimental work has shown that discharges can effectively lower concentrations of both hydrocarbons and NO in gas streams, though successful treatment over the wide range of gas compositions and temperatures present in typical engine exhaust streams has yet to be demonstrated. Modeling and current experimental efforts suggest that homogeneous gas-phase remediation by discharge technology will not have the necessary energy efficiency to be a practical replacement for present emission technologies. However, techniques that combine discharges with surface chemistry may have this potential. Packed-bed barrier discharge systems are well-suited to take advantage of plasma–surface interactions because of the large number of contaminant–surface collisions in the bed. Our experiments suggest that the packing material surface chemistry can alter the discharge-driven chemistry in synthetic lean-burn exhaust mixtures. Energy density measurements for the materials studied thus far indicate that the rate-limiting step occurs in the gas phase.

Both NO and NO_x were monitored with a chemiluminescence NO_x detector. The NO_2 concentration is the difference between the NO_x and NO signal. Any loss of NO could arise from oxidation to NO_2, reduction to N_2, partial oxidation to intermediate organonitrates, or deposition onto the packing material surface. Molecular nitrogen product was not detected due to the huge excess of N_2 in the gas stream. However, we failed to detect any other oxidative products, including nitric acid, nitrous oxide, or organonitrates. Also, as we show below, the observed dependence of the NO reactivity on oxygen and propene are similar to that found in thermal lean NO_x reduction catalysts, where N_2 has been detected. We therefore tentatively assign the loss of NO_x to the reduction of NO to molecular nitrogen.

We first consider spherical ZrO_2 beads as a packing material. These beads have a relatively high dielectric constant, are rugged, go into corona well, and are known to be resistant to plasma damage. Figure 3.9 shows our results using these beads on a lean exhaust mixture at 180°C. The fractional loss of NO_x was limited to approximately 20%, indicating oxidation of roughly 80% of the NO to NO_2. Although a small reductive channel exists (presumably $N\cdot + NO \rightarrow N_2 + O\cdot$), the effect of the plasma is mainly to enhance the oxidation of NO to NO_2.

Among other materials, we have tested several

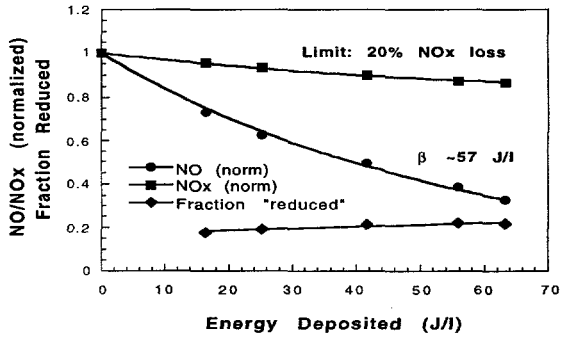

Figure 3.9. Plot of the normalized NO and NO_x concentrations as a function of energy density measured in joules per liter of flow for 3-mm ZrO_2 beads. The gas composition included 7.4% O_2, 4.3% CO_2, 2% H_2O, 0.2% CO, 760 ppm C_3H_6, and 270 ppm NO_x, with the balance N_2.

zeolites as packing materials. The most efficient packing material found so far is a commercially-available product labeled material B for proprietary reasons. The dashed lines in Fig. 3.10 illustrate data taken with this packing material. Assuming NO_x loss is due to NO reduction, a significant increase in the "reductive" channel was observed. The maximum fraction we have been able to "reduce" is approximately 50%. On one occasion we managed to increase the energy beyond that required to drop the NO concentration to our detection limit. No further change was observed in the NO_x concentration at higher energies. These observations suggest that the net reaction may be a disproportionation of NO into N_2 and NO_2.

One difference between zeolites and other packings we have tried is a large increase in the available surface area. To investigate the effect of the surface area we sintered a sample of material B for 1 hour at 800°C. This treatment changed the phase and reduced the Brunauer-Emmett-Teller (BET) surface area to near zero by collapsing the pores. Our results are illustrated by the solid lines in Fig. 3.10. We note that the energy efficiency for NO loss did *not* change, but the "reductive" channel was significantly smaller. Treatment at 700°C reduced the surface area by only 7% without a phase change, and had little effect on the chemistry. This suggests that the oxidation of NO to NO_2 occurs in the gas phase. One possible explanation for the increased loss of NO_x is plasma-assisted deposition of nitrates, nitrites, or organonitrites onto the zeolite. Preliminary temperature-programmed desorption measurements on used material detected large amounts of water and CO_2 deposited, but only modest amounts of NO and NO_2.

Figure 3.11 shows the effects of varying the oxygen concentration in the gas stream at a constant input power. Oxygen improved the efficiency for both NO oxidation *and* reduction, but the fraction of the NO that is oxidized did not change. Similarly, increasing the propene concentration at constant power improved the energy efficiency, with almost no effect on the fraction reduced. These results are similar to those observed in NO_x-selective catalytic reduction studies of thermally active zeolites. In those studies, the evidence suggested that the production of N_2 from NO_x was driven by reaction of NO_2 with methane to yield both NO and N_2 product. Added oxygen enhanced the oxidation of NO to NO_2, and added methane enhanced the subsequent reduction step. Such a reaction mechanism is consistent with our data.

Our data indicate that the identity of the packing material in a packed-bed dielectric barrier reactor can strongly affect the chemistry observed in the low-temperature plasma treatment of lean NO_x exhaust streams. We have shown that certain zeolite materials increase what we have labeled the "reductive" channel from 20 to 50%, a marked improvement from ZrO_2 and $BaTiO_3$ samples. It is plausible, but by no means proven, that this channel is indeed reduction to N_2. The 50% limit and apparent common precursor step may indicate that NO is disproportionating to NO_2 and N.

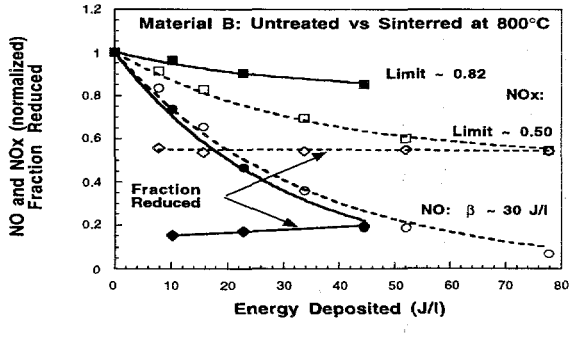

Figure 3.10. Comparison of material B performance before and after sintering at 800°C. The dashed lines represent the untreated material; solid lines the treated material.

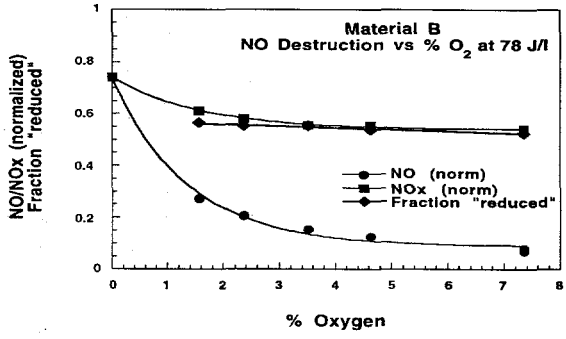

Figure 3.11. Plot of the normalized NO and NO_x concentrations as a function of added oxygen at constant energy on material B. The data were taken with 270 ppm NO at 180°C, with the concentrations of the other constituents held fixed.

Mechanisms of Radiolytic Decomposition of Complex Nuclear Waste Forms

T. M. Orlando, K. D. Keefer, K. Knutsen,† N. Petrick,§ Y. Su,† and D. P. Taylor†*

Supported by PNNL Laboratory Directed Research and Development (LDRD).

*EMSL Interfacial and Processing Science.
†Postdoctoral Research Associate.
§Special American Business Internship Training Program (SABIT) appointee.

Electron-Stimulated Degradation of Soda Glass
(Knutsen, Su, Keefer, and Orlando)

We have conducted experiments probing effects of radiation- and ionization-driven chemistry on the stability of glasses that may be used in the long-term storage and/or processing of low- and high-level nuclear wastes. In particular, we have investigated mechanisms of radiation-induced degradation of soda glass via low-energy (5–120 eV) electron-stimulated desorption (ESD) studies.[1] The major ionic desorption products observed are H^+, Na^+, O^+, and Si^+; the relative ion abundances at 100 eV are $H^+ > O^+ > Na^+ > Si^+$. The electron-stimulated production/desorption of neutral species, such as molecular hydrogen, has also been observed.

Na^+ signal intensity as a function of electron energy shows signal onset at ~45 eV, and a major threshold between 90 and 95 eV. O^+ has an initial threshold at 18 eV and a second major threshold near 30 eV. The H^+ signal shows a single threshold at 24 eV, and all ion yields increase monotonically with increasing electron energy. It is well known that ESD processes in wide band gap materials can be initiated by Auger decay of deep valence, shallow core, and/or deep core holes. This was first postulated by Knotek and Feibelman[2] to explain the ESD of cations from full-valence compounds such as TiO_2. The process generally consists of hole production, Auger decay, reversal of the Madelung potential, and ion expulsion due to the Coulomb repulsion. An example of such a mechanism as it pertains to the ESD of ions from soda glass is depicted in Fig. 3.12.

The Na^+ major threshold near 100 eV may be attributed to excitation of the Si (2*p*) level, followed by an interatomic Auger decay from the O (2*p*) level. There is also noticeable signal below 100 eV, which extends to about 45 eV. We believe this is associated with direct ionization of the Na^+ (2*p*) level, or possibly with ionization of surface-bound Na_2O. Stimulated desorption of sodium occurs at the interface, whereas stimulated diffusion and migration can possibly occur in the bulk. Thus, radiation-assisted diffusion of sodium to the surface of nuclear waste glass is a distinct possibility and is the subject of current investigation.

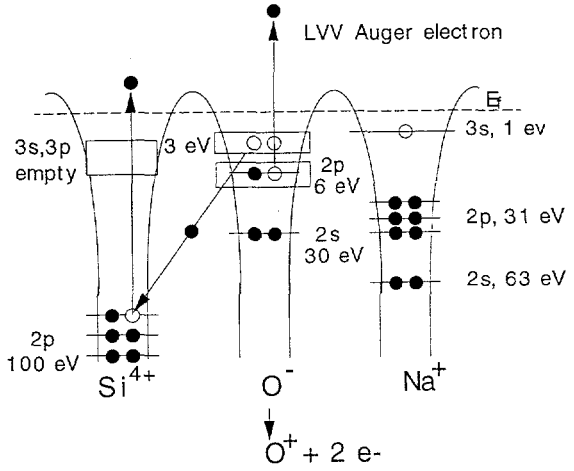

Figure 3.12. Interatomic Auger de-excitation model for ESD from soda glass. The filled circles represent electrons and the open circles represent holes created by either electron impact or the Auger process. The band designations and energy levels are not to scale.

Though we have worked at temperatures where chemisorbed water should not exist, the surface likely contains many terminal hydroxyl groups. Hydroxyl-rich surfaces are known to be unstable in an electron beam, and the H^+ ESD yields are quite high.[3] The H^+ threshold at 25 eV is in the correct energy region for O (2*s*) excitation in the terminal OH group. Excitation in the SiO_2 produces O^+ via intra-atomic Auger decay,[4] whereas excitation of the Si–OH produces H^+ by interatomic Auger decay. At present, we cannot completely rule out contributions to the H^+ yield from two-hole excitations localized on Si–H sites.

The primary O^+ thresholds near 30 eV can be attributed to excitation of the O (2*s*) level in SiO_2. It is interesting to note that the threshold energy for O^+ desorption does not shift significantly due

to the presence of Na. However, it is possible that the damage cross section increases considerably due to the Na loading. It is also established that the degree of surface hydration increases the susceptibility to radiation damage. Therefore, detailed experiments to quantify the damage cross sections and the degree of stimulated Na diffusion are currently under way.

Laser-Stimulated and Cathodoluminescence Studies of Yttria-Stabilized ZrO_2
(Taylor, Petrick, and Orlando)

We have studied luminescence of yttrium (6–10%)-stabilized ZrO_2 (100) and (110) single crystals in ultrahigh vacuum under pulsed laser (213 nm, 266 nm, and 355 nm) and electron-beam (500 eV) irradiation. Laser-stimulated luminescence and cathodoluminescence (LSL and CL), measured for 150–500 K, are similar, and consist primarily of a broad band between 375 and 750 nm with two maxima near 500 and 625 nm. Temperature quenching of LSL and CL demonstrate that the crystal lattice phonons interact strongly with the excited luminescence centers. Kinetics measurements utilizing 266-nm excitation indicate two decay components with activation energies of ~0.05 and 0.16 eV. We tentatively relate these activation energies to thermally stimulated migration of trapped electrons to luminescent centers. The nature of the luminescent centers and the relative importance of these processes with respect to electron- and photon-stimulated desorption processes are currently being addressed.

References

1. K. Knutsen, Y. Su, K. Keefer, and T. M. Orlando, "Mechanisms of Radiolytic Decomposition of Complex Nuclear Waste Forms," *Proc. Amer. Nucl. Soc. Meeting on Hazardous Waste Management* (1996), pp. 616-619.
2. M. L. Knotek and P. J. Feibelman, "Ion Desorption by Core-Hole Auger Decay," *Phys. Rev. Lett.* **40**, 964 (1978).
3. M. L. Knotek and J. E. Houston, "Study of the Stepwise Oxidation and Nitridation of Si (111): Electron Stimulated Desorption, Auger Spectroscopy, and Electron Loss Spectroscopy," *J. Vac. Sci. Technol. B* **1**, 899 (1983).
4. M. Petravic, "Desorption of Positive and Negative Ions from SiO_2/Si Surfaces by Electron Excitation of Core Levels," *Phys. Rev. B* **48**, 2627 (1993).

Mechanistic Studies of Radiation (Low-Energy Electron) Damage of $NaNO_3$ Surfaces and Interfaces

K. Knutsen, D. M. Camaioni,† and T. M. Orlando*

Supported by DOE Environmental Management Science Program (EMSP).

*Postdoctoral Research Associate.
†Environmental and Health Sciences Division, Materials and Chemical Sciences Department.

Previous work[1] at PNNL has demonstrated that excitation of $NaNO_3$ interfaces with 193-nm photons results in the stimulated desorption of mainly NO ($^2\Pi$) and O (^3P_J). These products were detected via state-resolved laser ionization spectroscopy, and the yields show a 1-photon laser fluence dependence, with no observable threshold, down to ~1 $\mu J/cm^2$. The O (^3P) *J*-state distribution is nonthermal, and the O (^3P) and NO ($^2\Pi$) velocity distributions are bimodal, with thermal and nonthermal components, consistent with near-surface dissociation events. The 193-nm (6.4-eV) valence band excitation in $NaNO_3$ solids/interfaces has been correlated with the NO_3^- $\pi^* \leftarrow \pi$ band and is below the nominal band-gap[2] energy of ~8 eV. Excitations of this band create localized excitons, which couple to phonons and trap at surface and/or defect sites. Decomposition of these excitons results in the *direct* desorption of NO ($^2\Pi$) and O (^3P). We favor a mechanism in which surface excitons decay to produce NO (g) + O (g) + O^- (sf), either in one step or via an NO_2^- intermediate, which is consistent with the observation of NO_2^- as a primary bulk radiolysis product.[3,4]

Under the EMSP program, radiolysis studies were carried out using pulsed low-energy electron beams to simulate the secondary cascading effects typically produced by high-energy radiation. In these studies, we also observe NO ($^2\Pi$) and O (^3P_J) as the primary neutral products. In addition, some O_2 (g) and a small amount of NO_2 (g) are produced. We believe these latter products are produced *indirectly* from recombination of O atoms with O, NO, or NO_3^- at the surface and in the bulk. The electron-energy thresholds for O and NO production are ~6–8 eV (Fig. 3.13), which corresponds to the $\pi^* \leftarrow \pi$ band but also overlaps the charge-transfer/conduction band transition.

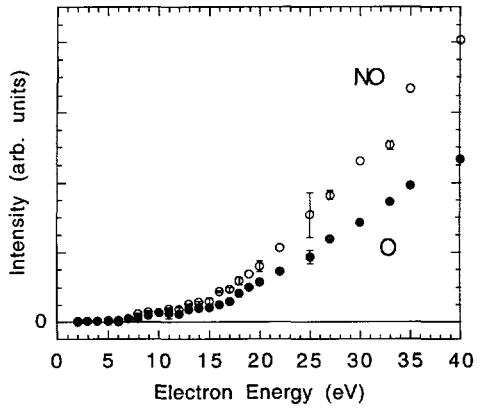

Figure 3.13. The threshold incident electron energies for the stimulated production and desorption of NO and O from $NaNO_3$ interfaces.

In addition to the above-mentioned exciton dissociation channels, removal of an electron from the NO_3^- valence band results in the production of NO_3^*, which can then dissociate to the neutral products detected. At incident energies above the conduction band, localization of secondary electrons at nitrate defect sites could result in the production of an excited species NO_3^{*2-}, which, though stable in the bulk, can decay at the surface via a process known as dissociative electron attachment to form $NO_2^{*-} + O + e$ and $NO + O_2^{*-} + e$. The NO_2^{*-} and O_2^{*-} can further dissociate to form O^-, which can trap at the surface or in the bulk.

In summary, the primary direct radiolysis products of $NaNO_3$ solid surfaces are NO, O, and O^-. We note that stable secondary products such as O_2, NO_2, NO_2^-, and NO_3^{2-} can also form in the bulk. These species are very reactive in the aqueous environment and are quite important in solution-phase reactions. As pointed out in an earlier study at Argonne National Laboratory,[5] it is likely that NO reactions with organic radicals lead to the production of N_2O (g) and NH_3 (g) in Hanford tank wastes. These reactions may occur in solution and at the solid/liquid interface. Thus, the electron-stimulated reactions of the desorption products, particularly the NO, with organic radicals formed in overlayers grown on salt surfaces are currently under investigation.

References

1. K. Knutsen and T. M. Orlando, *Phys. Rev. B*, submitted.
2. K. Knutsen and T. M. Orlando, *Surf. Sci.* **348**, 146 (1996).
3. J. Cunningham, in *Radical Ions*, E. T. Kaiser and L. Kevan, eds. (Interscience, New York, 1968), pp. 475–523.
4. J. Cunningham and L. R. Steele, *Phys. Rev. Lett.* **9**, 47 (1962).
5. D. Miesel, C. D. Jonah, S. Kapoor, S. Matheson, and M. C. J. Sauer, *Radiolytic and Radiolytically Induced Generation of Gases from Synthetic Wastes* (ANL Report ANL-93/43, 1993).

Decomposition of Hexafluoroethane in a Packed-Bed Corona Reactor

W. O. Heath and R. G. Tonkyn*

Supported by Battelle Memorial Institute Institutional Research and Development funds.

*Environmental Technology Division, Process Technology Department.

Very limited work has been performed to date on the destruction of fully fluorinated compounds such as those used as monomers in the electrochemical production of fluorinated plastics. Gas streams released during the electrochemical fluorination of plastics include hexafluoroethane in pure hydrogen. Accordingly, we have investigated the destruction of hexafluoroethane using a packed-bed corona reactor.

The decomposition of hexafluoroethane in a corona reactor packed with soda glass beads was examined as an alternative to thermal decomposition. Tests performed in air and in various mixtures of hydrogen and argon revealed removal rates above 93% and as high as 99% at concentrations between 100 and 10,000 ppm. Our results suggest that the addition of argon to the gas stream can significantly lower the overall energy costs. The primary destruction byproducts appeared to be SiF_4, H_2O, and CH_4, with small amounts of CF_4, little or no HF, and no F_2.

As shown in Fig. 3.14, the decomposition of hexafluoroethane in air is first order in the input energy density, but extremely energy intensive. The exponential factor, called the specific energy,

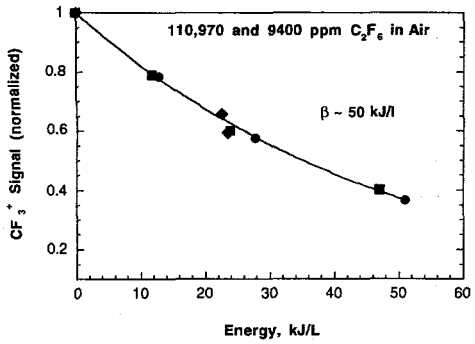

Figure 3.14. Decomposition of C_2F_6 as a function of energy.

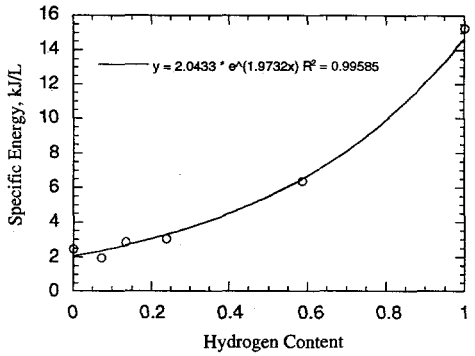

Figure 3.15. Effect of hydrogen content on specific energy at 900 ppm C_2F_6.

has units of J/L and is defined as the energy required to reduce the concentration of contaminant in a given volume to 1/e of its initial value. The extremely high energy requirement is consistent with the primary step being dissociative electron attachment, because the energy resonance is quite high in C_2F_6. The observed independence of the rate constant over a factor of 100 in concentration is evidence that the addition of C_2F_6 has no significant effect on either the average electron density or kinetic energy in the plasma.

We performed similar tests on the destruction of C_2F_6 in pure hydrogen, pure argon, and various intermediate concentrations. As shown in Fig. 3.15, the specific energy increases monotonically with hydrogen content. Two factors could be at work here. First, the addition of a diatomic gas to pure argon will decrease the average electron kinetic energy simply because of an increase in the inelastic scattering due to the greater number of internal degrees of freedom in the bath gas. It is also possible that the presence of argon metastables and/or ions alters the overall chemistry, although we saw no new product species with the addition of argon.

The only fluorine-containing products detected in our mass spectrometer were CF_3 and C_2F_5, which are both daughter products of C_2F_6, and SiF_3, which is presumed to be a fragment of SiF_4. Based on the relative intensities, we believe that SiF_4 was the primary decomposition product within that mass range. At lower mass, background subtraction revealed peaks corresponding to methane and water. Little or no hydrofluoric acid was detected, and no molecular fluorine signal was observed. Following the experiments, disassembly of the reactor revealed that the glass beads used as the packing material were etched, as was the reactor wall to a lesser extent.

We have established that hexafluoroethylene can be decomposed at low temperatures using a packed-bed corona reactor, although the measured energy requirements were found to be quite high. Destruction appeared to be complete in that no partially decomposed fluorocarbons were detected in the reactor effluent. Based on our experimental data, it should be possible to add argon to the waste stream containing C_2F_6 in hydrogen as a means of lowering the overall energy requirement for treatment.

Nonthermal Interfacial Processes: Electron- and Photon-Stimulated Desorption, Dissociation, and Surface/Interface Chemistry

T. M. Orlando, M. T. Sieger, W. C. Simpson,* R. G. Tonkyn,*

Supported by DOE Office of Basic Energy Sciences.

*Postdoctoral Research Associate.

We have a multitask program that is directed toward understanding low-energy (5–150 eV) electron and ultraviolet (6–12 eV) photon-stimulated desorption, dissociation, and surface/interface chemistry. In particular, we study electron-stimulated desorption/dissociation (ESD) and photon-stimulated desorption/degradation (PSD), as well as stimulated inelastic and reactive scattering on and in molecular thin films and wide-band-gap materials. Developing an understanding of such processes is critical if one hopes to unravel some of the complicated events that occur during the interaction of high-energy radiation (such as that produced by radioactive decay events) with solids and mixed-phase interfaces. In the last few years, we have carried out a series of electron-stimulated desorption experiments[1–6] on nanoscale films of amorphous and crystalline D_2O ice grown on Pt (111). Such an approach allows us to probe the details of radiation damage of water and wet interfaces, and the use of amorphous ice may allow us to extrapolate to radiation damage events that may occur in the liquid state.

It is important to note that ESD is a very sensitive and ultrafast local probe of the surface terminal sites and local scattering potential. Therefore, we carried out ESD studies as a function of ice-film temperature, phase, and film thickness. Such studies allow us to monitor changes in ESD cross sections (yields) that result from excited-state lifetime changes that are brought about by surface restructuring. In addition, we have also carried out ESD and PSD studies of environmentally relevant oxide substrates such as $NaNO_3$ (Ref. 7) and ZrO_2 (see below). Thus far, we have determined that (1) ESD and PSD of $NaNO_3$ occur primarily via exciton dissociation, and can be understood in terms of the model previously developed to describe radiation damage in alkali halide systems; and (2) ESD of ZrO_2 (100) involves Auger-stimulated events. Preliminary results indicate that PSD of ZrO_2 is a very complicated multiple-photon process.

The Electron-Stimulated Desorption of D^+ from D_2O Ice
(Sieger, Simpson, and Orlando)

The behavior of water and ice under energetic particle bombardment is important in the treatment and storage of wet radioactive wastes. Spent nuclear fuel rods are commonly stored under water, so the interactions of radiation with the aqueous environment are of great interest. Most studies of water radiolysis have focused upon the fragmentation and desorption caused by interaction with highly energetic particles ($E > 1$ keV). High-energy collisions can, however, create vast numbers of secondary electrons with energies resonant with valence excitations, which can lead to bond breaking. The detailed physics of this process is, however, not fully understood.

To gain insight into the mechanisms of water radiolysis, we have carried out a detailed investigation of the electron-stimulated desorption of deuterium cations (D^+) from thin (1–40 monolayer) D_2O ice films deposited on a Pt (111) substrate. Ice films are easier to study in an ultrahigh vacuum environment, and amorphous water ice is similar to liquid water in many respects. We have found that the yield of cations increases as the degree of surface hydrogen bonding decreases, which suggests that the local environment of the water molecule (at the vapor/liquid interface, or adsorbed on a surface) has a large bearing on its cross section for radiolytic decomposition.

Figure 3.16 shows the D^+ cation yield versus ice temperature at selected electron energies. The yield generally increases between 90 and 160 K, and the irreversible amorphous–crystalline phase transition is evidenced by a drop in total yield at about 162 K. Our analysis of the data suggests that water molecules at the ice surface undergo a reduction in coordination number near 120 K, well below the temperature at which the evaporation rate becomes appreciable. This reduction in coordination number may be related to thermally activated migration of Bjerrum L defects to the surface. By 140 K, the amorphous surface has reached a stable configuration in which the H-bond coordination number does not change, and near 162 K the ice crystallizes, reforming the

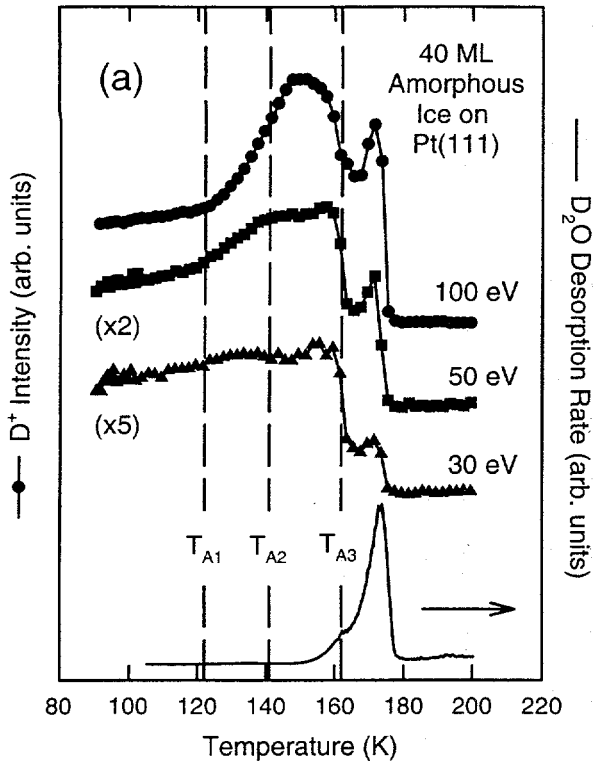

Figure 3.16. Total D^+ ESD yield as a function of ice temperature for selected excitation energies and the film desorption rate. The solid trace at the bottom is the thermal desorption signal.

hydrogen bonds. Examination of the relevant dissociative states of the water molecule suggests that the excited-state lifetimes are being strongly affected by the degree of surface hydrogen bonding. Similarities between the temperature and thickness dependence of the D^+ yield, D^- yield, and work function give further evidence for temperature-dependent changes in the surface structure. These results imply that the local environment of a water molecule is important for its dissociation cross section, and such structure-dependent effects may be important for water radiolysis in astrophysics, biophysics, and atmospheric chemistry, as well as waste storage.

Dissociative Electron Attachment in Condensed D_2O Films: The Effect of Film Thickness, Temperature, and Morphology
(Simpson, Sieger, Kimmel, and Orlando)

Low-energy electron-molecule scattering results in transient negative-ion resonances which decay via electron autodetachment and dissociative electron attachment (DEA). DEA involves multielectron core-excited resonances that consist of an excess electron temporarily bound by the positive electron affinity of an electronically excited target molecule. These are generally two-electron, one-hole configurations that are classified as either Feshbach or core-excited shape resonances. Because the lifetimes of Feshbach resonances are typically ~10^{-12}–10^{-14} sec, dissociation into a stable anion and neutral fragment(s) may result if the resonance is dissociative in the Franck-Condon region. Considerable attention has been focused recently on extending the current understanding of gas-phase DEA to explain the resonant behavior observed in the ESD of negative ions and neutrals from adsorbed molecules and from molecular solids. DEA in condensed molecules can be described in terms of single-site scattering, as is done for gas-phase molecules, but recent investigations demonstrate that factors due to the surrounding medium must be considered. These include (1) changes in the symmetry of the scattering problem, (2) the medium polarization response, (3) the fixed orientation of the molecule with respect to the solid surface, and (4) post-dissociation interactions between the ion fragment and surrounding medium.

The ESD of D^- ions from condensed D_2O films has been investigated. Figure 3.17 shows three low-energy peaks in the D^- yield, which are identified as arising from excitation of $^2B_1$, $^2A_1$ and $^2B_2$ dissociative electron attachment resonances. The resonance energies and ion yields vary with the thickness, temperature, and morphology of the D_2O film. At 90 K, the resonances shift to higher energy and their ion yields decrease with increasing film thickness. This behavior reverses when the film is heated. The D^- yield generally increases with temperature, but it deviates noticeably from this trend at temperatures corresponding to structural phase transitions in bulk ice. The D^- temperature dependence is remarkably similar to that observed for ESD of low velocity D^+ from D_2O ice, even though the two originate from different electronic excitations. These results are discussed in terms of the reorientation of surface D_2O molecules, which changes their excited-state lifetimes and hence their ESD cross sections.

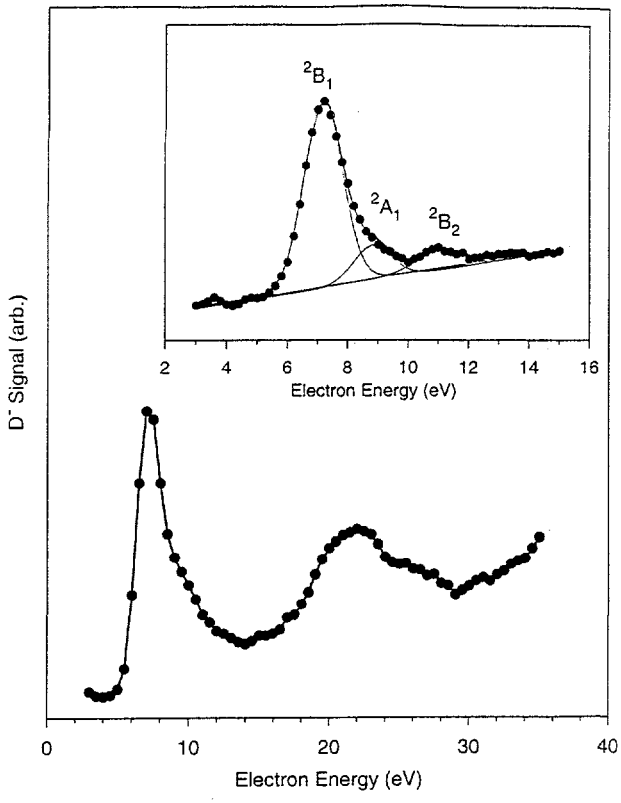

Figure 3.17. D^- signal vs. incident electron energy, collected at 120 K from a 5-ML film of amorphous ice grown at 90 K. The inset contains a higher-resolution scan in the energy range 3–15 eV, along with a fit to the data.

Low-Energy (5–50 eV) Electron-Stimulated Desorption of Atomic Hydrogen and Metastable Emission from Amorphous Ice
(Orlando, Kimmel, P. Cloutier,* and L. Sanche*)
*MRC Group in Radiation Sciences, University of Sherbrooke, Quebec

Low-energy (5–50 eV) electron-stimulated desorption of D (1 ^{2}S) from amorphous D_2O water films has been studied using laser resonance-enhanced multiphoton ionization (REMPI) spectroscopy. The D (1 ^{2}S) desorption product shown in Fig. 3.18 has a threshold energy of ~6.5 ± 0.3 eV relative to the vacuum level, and a low velocity distribution. ESD of electronically excited D ($n \geq 2$ ^{2}S) was not detected using photoionization schemes.

A small metastable ($n \geq 2$ ^{2}P) desorption yield and/or emission of ultraviolet (UV) photons ($h\nu \geq$ ~ 6 eV) was detected at incident electron energies

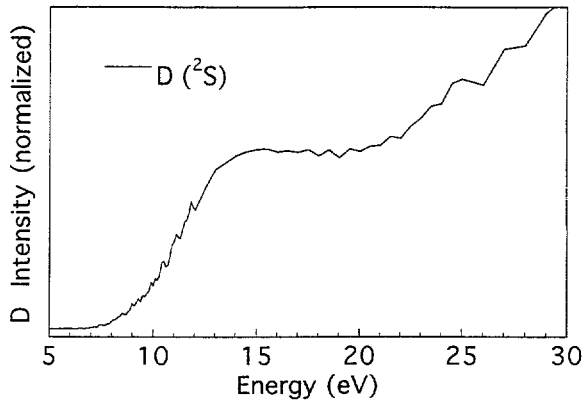

Figure 3.18. Desorption yield of D (1 ^{2}S) as a function of incident electron energy. The D (1 ^{2}S) was detected using 2+1 resonance enhanced multiphoton ionization spectroscopy via the $3s \leftarrow\leftarrow 1s$ ^{2}S two-photon transition.

> 25 eV. This experiment was carried out at the University of Sherbrooke using a multichannel plate detection technique. We attribute the ground-state D desorption to exciton decay, and associate the small metastable/UV photon emission yield with dissociation of doubly excited states and efficient autoionization.

Electron-Stimulated Desorption of Oxygen from Yttria-Stabilized Cubic Zirconia
(Simpson and Orlando)

Zirconium-based alloys are commonly used as cladding materials for nuclear fuel rods, as well as for various parts in nuclear reactors. Zirconium is chosen for the robust nature of the oxide (ZrO_2) that it forms, which is highly corrosion resistant. However, under the extreme conditions present in a nuclear reactor, its resistance to corrosion breaks down somewhat. It has been suggested that secondary electrons generated in the material by ionizing radiation lead to its degradation, thereby weakening its resistance to chemical attack.

We are currently conducting a set of controlled experiments to investigate the decomposition of ZrO_2 by low-energy electrons. Our approach is to take a well-characterized ZrO_2 surface and submit it to bombardment by a monochromatic low-energy electron beam. By varying the energy of the incident electrons while monitoring the ion and neutral flux desorbing from the ZrO_2 surface, we are able to identify the nature of the excitations that lead to decomposition.

Figure 3.19 shows some preliminary results of our work. The O^+, H^+, and OH^+ yields from the electron bombardment of the (100) facet of yttria-stabilized cubic ZrO_2 were collected as a function of the incident electron energy. The crystal was first exposed to water vapor, then heated to 450 K, which drove off most of the water, leaving behind only a small amount of H and OH on the surface. Both the H^+ and OH^+ yields have a threshold near the O (2*s*) ionization energy, whereas the threshold for O^+ desorption is near the ionization energy of the Zr (4*p*) core level.

The desorption of H^+ and OH^+ likely results from the ionization of the OH groups on the surface. O^+ desorption, on the other hand, appears to follow the classic Knotek-Feibelman model for electron-stimulated desorption (ESD) from oxide surfaces. In this model, ionization of an oxygen core level does not lead to O^+ desorption. However, ionization of a zirconium core level does lead to desorption through an Auger decay mechanism. After the Zr 4*p* level is ionized, it is filled by a valence electron residing on a nearby O atom. The same oxygen atom then emits two more Auger electrons to conserve the total energy of the system. This oxygen atom, which was originally in an O^{2-} state, finds itself in a repulsive O^+ state and is ejected from the surface. ZrO_2 appears to have a reasonably high cross section for this to occur, which may explain some of its instability in an ionizing environment. Future investigations will look into the ESD of neutral oxygen atoms from ZrO_2, which, according to the literature, should have a much larger ($\times 10^8$) cross section.

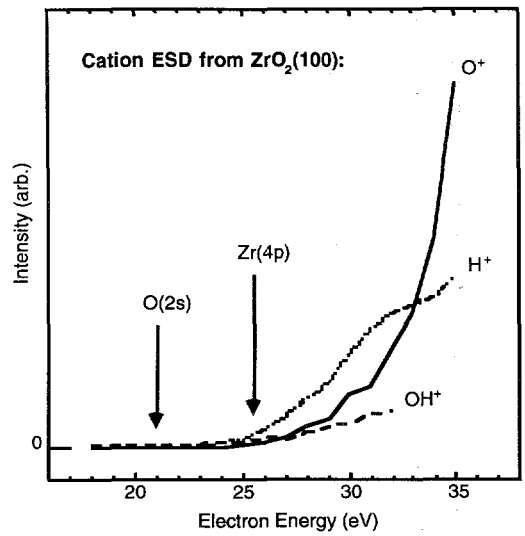

Figure 3.19. ESD cation yields from ZrO_2 (100) exposed to a small amount of water and heated to 450 K.

References

1. G. A. Kimmel, T. M. Orlando, L. Parenteau, and L. Sanche, *J. Chem. Phys.* **101**, 3282 (1994).
2. G. A. Kimmel, R. G. Tonkyn, and T. M. Orlando, *Nucl. Instr. Meth. Phys. Res. B.* **101**, 179 (1995).
3. G. A. Kimmel and T. M. Orlando, *Phys. Rev. Lett.* **75**, 2606 (1995).
4. G. A. Kimmel and T. M. Orlando, *Phys. Rev. Lett.* **77**, 3983 (1996).
5. G. A. Kimmel, L. Parenteau, L. Sanche, and T. M. Orlando, *J. Phys. Chem.*, submitted.
6. M. T. Sieger, W. C. Simpson, and T. M. Orlando, *Phys. Rev. B*, submitted.
7. K. Knutsen and T. M. Orlando, *Phys. Rev. B*, submitted.

Photon-Stimulated Desorption of O (^{3}P) and NO ($^2\Pi$) from $NaNO_3$ Single Crystals

K. Knutsen and T. M. Orlando*

Supported by DOE Office of Basic Energy Sciences.

*Postdoctoral Research Associate.

The use of resonance-enhanced multiphoton ionization (REMPI) and time-of-flight (TOF) quadrupole mass spectrometry (QMS) detection schemes revealed that O (^{3}P) and NO ($^2\Pi$) were primary $NaNO_3$ PSD products, while O (^{1}D) and O_2 were detected only at 193-nm laser fluences >100 μJ/cm^2. Anions such as NO_2^- and O^- were not detected by TOF techniques nor by QMS. The NO($^2\Pi_{1/2}$), O($^3P_2$), and O($^1D_2$) yields as a function of 193-nm fluence are presented in Fig. 3.20. The O(^{3}P) data were obtained with the probe laser tuned to the O ($^3P_2$) transition, and the NO data were taken on the NO ($^2\Sigma^+$–$^2\Pi_{1/2}$) (0,0) band head and on the N = 15 R_1 transition. The data points are the average of 100 to 200 laser shots, with the desorption-probe laser time delay set to the peak of the velocity distributions. The solid lines in Fig. 3.20 are linear least-squares best fits to the data and yield identical slopes of 0.9 ± 0.1 for both O ($^3P_2$) and NO ($^2\Pi_{1/2}$). Thus, the fluence depend-

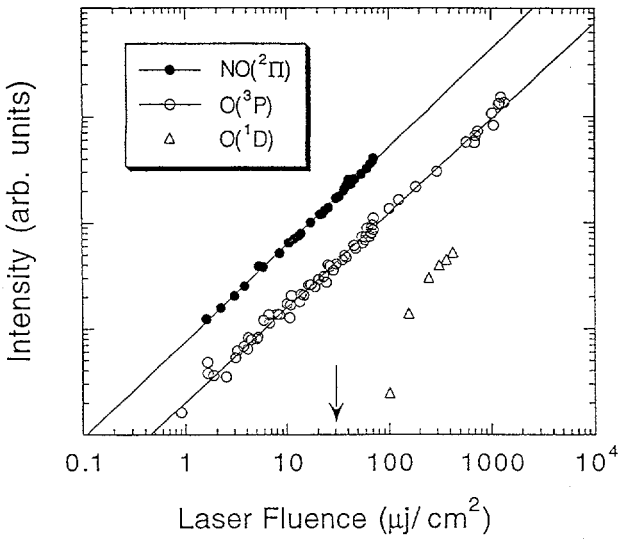

Figure 3.20. The NO ($^2\Pi_{1/2}$), O ($^3P_2$) and O (^{1}D) yields as a function of desorption laser fluence. The data are scaled for ease of presentation. The lines are the linear least-squares best fits to the data, and show a one-photon dependence on laser fluence for both the NO ($^2\Pi_{1/2}$) and O ($^3P_2$) primary desorption products. The fluence threshold and non-linear fluence dependence of O (^{1}D) suggests that it is formed by secondary, or higher order, processes. The arrow denotes the typical desorption laser fluence at which the time-of-flight and fine-structure state distributions were obtained.

ence of the O and NO yields is one-photon. No "threshold" laser fluence for desorption was apparent within the limit of our detection sensitivity, and no induction time was required for the appearance of the NO and O (^{3}P) desorption products. These observations confirm that the PSD process producing these fragments is direct and is not driven by plasma interactions or defect formation.

At excimer laser fluences greater than ~100 μJ/cm^2, a small NO_2 signal appeared in the QMS, and a small, broad O^+ signal was observed in the TOF spectrum at the correct probe laser wavelength (203.6 nm) for O (^{1}D) ionization. The 193-nm fluence dependence of this signal is highly nonlinear (Fig. 3.20). Because we do not vary our ion extraction conditions, and the kinetic energy of the desorbing neutrals is fixed for a given time delay, we believe that the broadening we observe in the O^+ signal is related to changes in the kinetic energy imparted at the point of ionization. This would be consistent with a photodissociation event in the probe laser beam, immediately followed by ionization of the resulting O (^{1}D) fragment. Direct REMPI detection of NO_2(g) is below our detection sensitivity limit of 10^6 molecules/cm^3.

In summary, 193-nm photon absorption in $NaNO_3$ creates surface excitons, either directly or via localization of mobile excitons that are created in subsurface layers. Decomposition of these excitons results in the direct desorption of NO ($^2\Pi$) and O (^{3}P). We favor a dissociation mechanism in which surface interactions may stabilize the exciton with respect to autodetachment, providing access to otherwise energetically inaccessible repulsive anionic potential energy surfaces. These excitons then decay to produce NO (g) + O (g) + O^- (sf), either in one step or via a sequence of dissociations. The similarities between our data and that obtained from PSD of alkali halides suggest that this general mechanism should be applicable to other ionic materials containing polyatomic anions and is analogous to the X_2^{*-} H-center mechanism used to explain both ESD and PSD from alkali halides. However, an important difference in our proposed mechanism is that, for $NaNO_3$, the formation of the H-center precursor is not necessary, because the molecular anion already exists.

4. Cluster Models of the Condensed Phase

Cluster Model Studies of the Structure and Bonding of Environmentally-Important Materials

*L.-S. Wang, J. B. Nicholas,**
S. D. Colson, S. R. Desai,†
H. Wu,§ S. Li,† and C. M. Rohlfing‡

Supported by DOE Office of Basic Energy Sciences.

*EMSL Theory, Modeling, and Simulation.
†Postdoctoral Research Fellow.
§Washington State University.
‡Sandia National Laboratory, Livermore, Cal.

Oxides of Si, Al, Mg, and Ti are major components of the earth and are important environmental materials. Their surface chemistries influence the storage and underground transport of waste materials. EMSL is directing a major effort to understanding their surface and interface properties. We have initiated a program to study the structure and bonding of these materials with cluster models. We combine experimental and theoretical studies using anion photoelectron spectroscopy (PES) and quantum calculations. The smaller, controlled sizes of these cluster systems provide atomic-level models to better understand bulk surfaces and defect sites and are an excellent testing ground to benchmark theories intended for large and "real-world" systems.

A state-of-the-art magnetic-bottle time-of-flight PES spectrometer with a laser vaporization cluster source has been built for these studies. With high mass and high electron energy resolution, this is a powerful apparatus for the study of clusters. Several initial experiments have been carried out on small silicon oxide, germanium oxide, and aluminum oxide clusters. Preliminary studies on titanium clusters have also been performed.

1. Structure and Bonding of Small Aluminum Oxide Clusters: $Al_xO_y^-$ (x = 1–2, y = 1–5)[1,2]

The structure and bonding of aluminum oxide clusters, Al_xO_y (x = 1–2, y = 1–5), are studied with anion PES and are compared with preliminary *ab initio* calculations. The spectra were obtained at four detachment photon energies: 2.33, 3.49, 4.66, and 6.42 eV. The 6.42-eV spectrum for AlO^- reveals the $X^2\Sigma^+$ ground state and two excited states of AlO. The 6.42-eV spectrum for AlO_2^- also shows three states for AlO_2: the $X^2\Pi_g$ ground state and the $A^2\Pi_u$ and $B^2\Sigma_g^+$ excited states. The spectra for $Al_2O_y^-$ clusters (Fig. 4.1) show vibrationally resolved ground states, which come from Al *sp*-type orbitals, and also high-binding-energy excited states, which are mainly of oxygen 2*p* character. Al_2O_2, which has a $\mathbf{D_{2h}}$ rhombus structure, has an electron affinity (EA) of 1.88 eV, and its singlet-triplet excitation energy is measured to be 0.49 eV. Much higher EAs are measured for the larger Al_2O_y clusters. The PES spectra of $Al_2O_3^-$, $Al_2O_4^-$, and $Al_2O_5^-$ show very similar electronic and vibrational structure. These observations suggest that these molecules all have a rhombus-like structure, similar to Al_2O_2, with the oxygen atoms sequentially attaching to the terminal aluminum atoms (Fig. 4.2). The spectra are consistent with an ionic bonding view of these clusters, and the vibrational frequencies are in close agreement with the theoretical results. Significant information about the structure and bonding of these small aluminum oxide clusters is obtained.

2. Small Silicon Oxide Clusters: Chains and Rings[3]

We studied several silicon oxide cluster series with different Si:O stoichiometries: $(SiO)_n^-$ (n = 3–5), $(SiO_2)_n^-$ (n = 1–4), and $Si(SiO_2)_n^-$ (n = 2,3). The $(SiO)_n$ clusters are shown to be closed-shell molecules, and the HOMO-LUMO gaps are observed from the PES spectra to decrease for larger n. These clusters are shown to have ring structures. Si_3O_4 is known to have a $\mathbf{D_{2d}}$ structure with two perpendicular Si_2O_2 rhombuses. The PES spectrum of $Si_4O_6^-$ is very similar to that of $Si_3O_4^-$. It is concluded that Si_4O_6 has a similar structure with a chain of three Si_2O_2 rhombuses. The $(SiO_2)_n$ clusters all exhibit high electron affinities and only one band is observed at 4.66-eV photon energy (Fig. 4.3). These clusters are shown to have similar chain structures containing Si_2O_2 rhombuses, but the two terminal Si atoms are bonded to an extra O atom each. These clusters may provide structural models for oxygen-deficient defects in bulk silicon oxides.

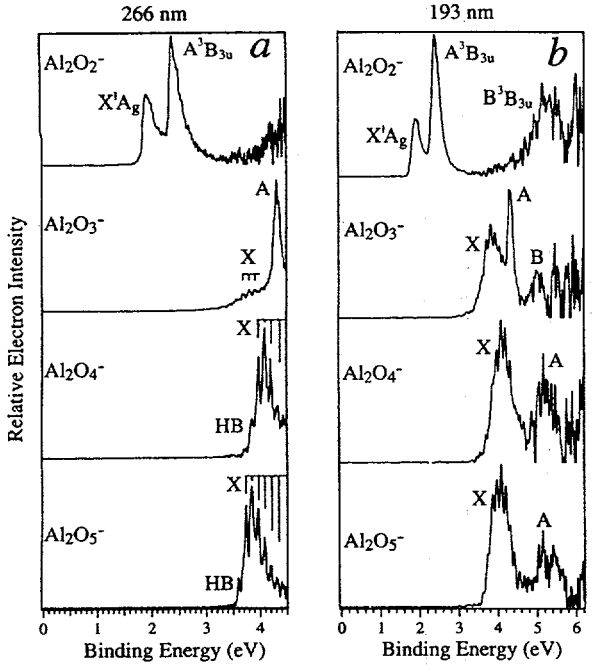

Figure 4.1. Photoelectron spectra of $Al_2O_y^-$ (y = 2–5) clusters at (a) 4.66 eV (266 nm); and (b) 6.42 eV (193 nm). Peaks labeled "HB" are hot bands.

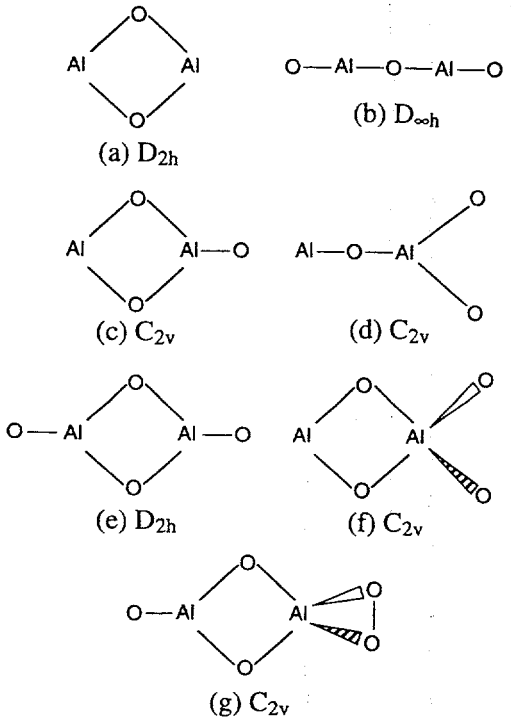

Figure 4.2. Possible structures of the Al_2O_y clusters, based on experimental observations and preliminary calculations at the Hartree-Fock and MP2 levels. The rhombus-type structures are suggested to be the ones observed in the current experiments.

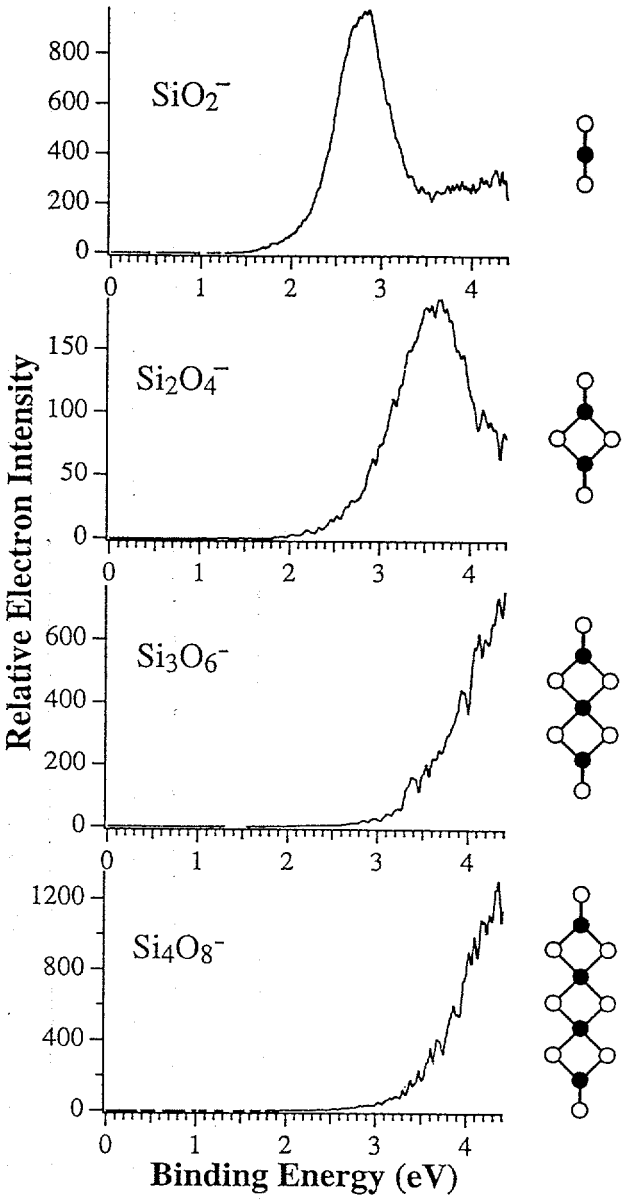

Figure 4.3. Photoelectron spectra of $(SiO_2)_n^-$ (n = 1–4) at 4.66-eV photon energy. The structures of the neutral clusters are shown schematically.

3. Si_3O_y (y = 1–6) Clusters: Models for Oxidation of Silicon Surfaces and Defect Sites in Bulk Oxide Materials[4]

We have studied the structure and bonding of a series of silicon oxide clusters, Si_3O_y (y = 1–6), using anion photoelectron spectroscopy and *ab initio* calculations (Fig. 4.4). For y = 1–3, the clusters represent the sequential oxidation of Si_3 and provide structural models for the oxidation of silicon surfaces. For y = 4–6, the clusters contain a

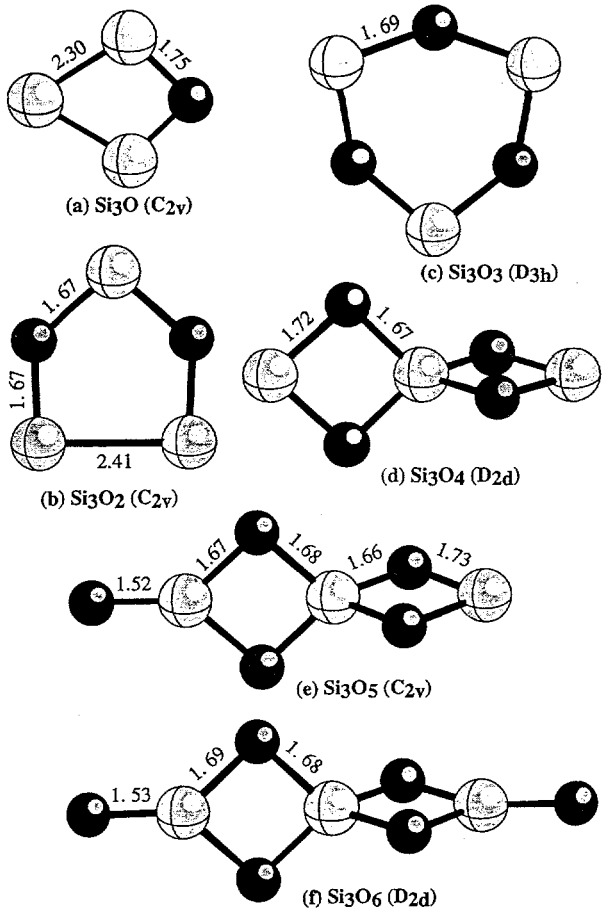

Figure 4.4. MP2/6-311+G* optimized structures of the Si_3O_y (y = 1–6) clusters. All bond lengths are in Å. Note that for y = 1–4, all the O atoms are bridge bonded to two Si.

central Si in a tetrahedral bonding environment, suggesting the onset of the bulk-like structure. Evidence suggests that the Si_3O_4 cluster ($\mathbf{D_{2d}}$) may provide a structural model for oxygen-deficient defect sites in bulk SiO_2 materials.

References

1. S. R. Desai, H. Wu, and L.-S. Wang, *J. Mass. Spectrom. Ion Processes*, in press.
2. S. R. Desai, H. Wu, C. Rohlfing, and L.-S. Wang, *J. Chem. Phys.* **106**, 1309 (1997).
3. L.-S. Wang, S. R. Desai, H. Wu, and J. B. Nicholas, *Z. Phys. D*, in press.
4. L.-S. Wang, J. B. Nicholas, H. Wu, M. Dupuis, and S. D. Colson, *Phys. Rev. Lett.*, submitted.

Photoelectron Spectroscopy and Electronic Structure of Metal Clusters and Chemisorbed Metal Cluster Complexes

*L. S. Wang, H. Wu,**
*C. F. Ding,† and X. Li**

Supported by the National Science Foundation.
*Washington State University.
†Postdoctoral Research Fellow, WSU.

One of the key issues in the study of metal clusters is to understand the electronic structures of these intermediate systems and their evolution toward bulk band structure as the cluster size increases. Transition-metal clusters are of particular interest due to their diverse physical and chemical properties, but they have presented considerable experimental and theoretical challenges, primarily due to the presence of partially filled *d*-orbitals. Heretofore, very little has been known about their detailed structures and their electronic properties. Our goals are to elucidate the evolution of the electronic structure of the transition-metal clusters, and to use the obtained electronic structure information to understand the chemical and physical properties of the clusters.

The interactions between oxygen and metals are important in many areas of chemistry and materials sciences. Oxide clusters involving Cu and Fe are particularly interesting because of the importance of Cu and Fe oxide materials. Some small Cu and Fe oxide clusters are also active centers in many organic metallic compounds and non-heme proteins. We focused on clusters involving one to four metal atoms and have found that: (1) CuO_x^- clusters have distinct isomers involving either oxide molecules or O_2 complexes, (2) electron affinity of the oxide clusters increases with oxygen content up to the highest oxidation states of the metal (the concept of sequential oxidation), and (3) for Fe_3O_x and Fe_4O_x clusters the O atoms can be viewed as sequential chemisorption on surfaces of the core metal clusters, Fe_3 and Fe_4.

1. Evolution of the Electronic Structure of Small Vanadium Clusters from Molecular to Bulk-Like[1]

The evolution of the electronic structure of V_n clusters has been probed by photoelectron spec-

troscopy (PES) at photon energies of 3.49, 4.66, and 6.42 eV (Fig. 4.5). Three regions of spectral evolution are distinctly observed as a function of cluster size: molecular-like behavior for n = 3–12; transition from molecular to bulk-like from n = 13–17; and gradual convergence to bulk for n > 17, for which a surface-like feature is observed to slowly merge into the bulk feature near n = 60. The PES spectra provide an atom-by-atom view of the evolution of the electronic structure of the V_n clusters from molecular to bulk-like.

2. Chemical Bonding Between Cu and Oxygen. Copper Oxides vs. O_2 Complexes: A Study of CuO_x (x = 0–6) Species by Anion Photoelectron Spectroscopy[2]

An extensive photoelectron spectroscopic study on the CuO_x^- (x = 0–6) species has been carried out. The photoelectron spectra of these species were obtained at four detachment photon energies: 2.33, 3.49, 4.66, and 6.42 eV. The spectra of the copper atom are included to show the dependence of the detachment cross sections on the photon energies (Fig. 4.6). An intense two-electron transition to the ^2P excited state of Cu is also observed in the 6.42-eV spectrum of Cu^-. For CuO^-, we observe an excited state of the anion, as well as photodetachment transitions to charge-transfer excited states of CuO ($Cu^{2+}O^{2-}$). Six transitions are observed for CuO_2^- at 6.42 eV, revealing all six valence molecular orbitals of the linear OCuO molecule.

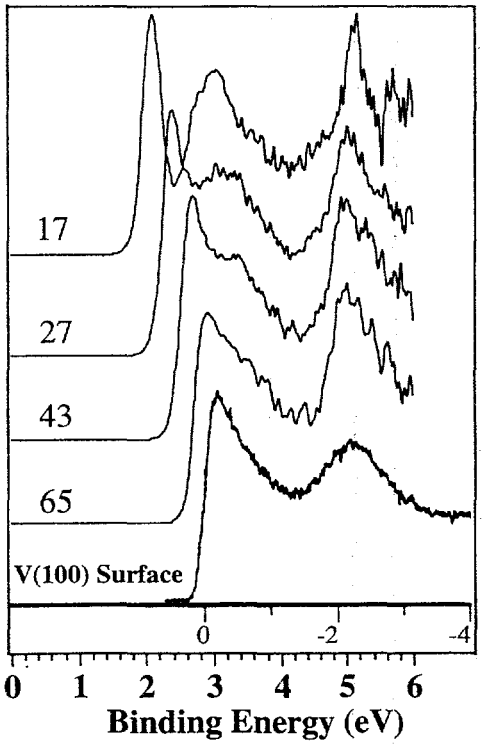

Figure 4.5. Photoelectron spectra of V_{17}^-, V_{27}^-, V_{43}^-, and V_{65}^- at 6.42-eV photon energy, compared to the bulk photoelectron spectrum of V(100) surface at 21.21-eV photon energy, showing the appearance of bulk features at V_{17} and how the cluster spectral features evolve toward the bulk.

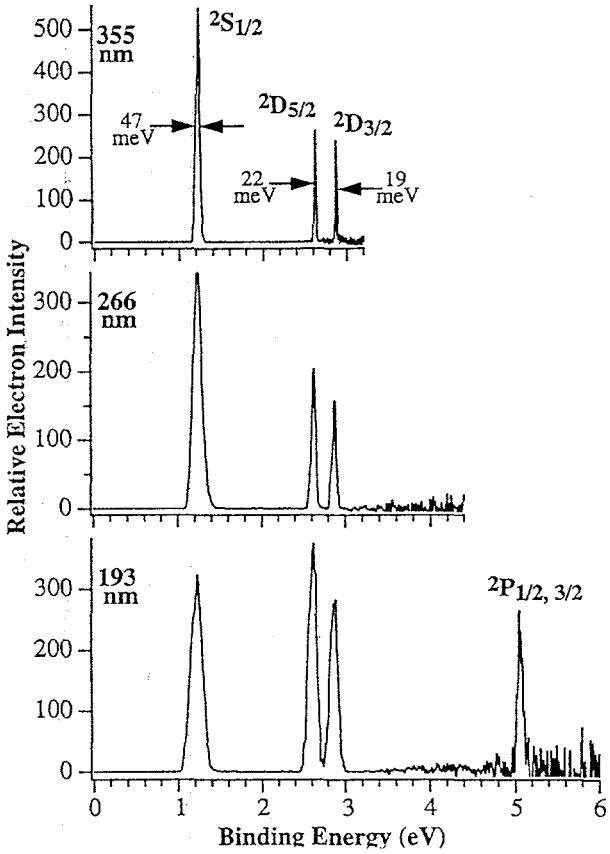

Figure 4.6. Photoelectron spectra of Cu^- at 355, 266, and 193 nm.

CuO_3^- is observed to undergo photodissociation at 3.49 eV to give an internally hot CuO^- plus O_2. It is shown to have an $OCuO_2$ type of structure and its electronic structure can be viewed to be due to that of CuO perturbed by an O_2. For CuO_4^-, two isomers are observed; one undergoes photodissociation at 3.49 eV and is shown to be a Cu/O_2 complex, $Cu(O_2)_2^-$. The second isomer yields spectra identical to that of the linear $OCuO^-$ with a slight energy shift and is concluded to be an $OCuO^-$ solvated by a very weakly bonded O_2, $(OCuO^-)O_2$.

CuO_6^- exhibits similar behaviors as CuO_4^- with a Cu/O_2 complex, $Cu(O_2)_3^-$, and an O_2-solvated CuO_2^-, $(OCuO^-)(O_2)_2$. The CuO_5^- spectra are observed to be similar to that of CuO_3^- and arise from a CuO_3^- solvated by an O_2, $(OCuO_2^-)O_2$.

3. Sequential Oxygen Atom Chemisorption on Surfaces of Small Iron Clusters[3]

Photoelectron spectra of iron oxide clusters, $Fe_xO_y^-$ (x = 1–4, y = 1–6), show that for a given x, the electron affinity increases with the number of O atoms (Fig. 4.7), which is consistent with an increasing degree of oxidation. The results, interpreted based on charge-transfer interactions between the Fe_x clusters and the O atoms, provide key information about oxide cluster structures in which each O atom probably locates on the surface of the clusters for the x = 3 and 4 series (Fig. 4.8). These clusters provide novel model systems for understanding the electronic structure of bulk iron oxides.

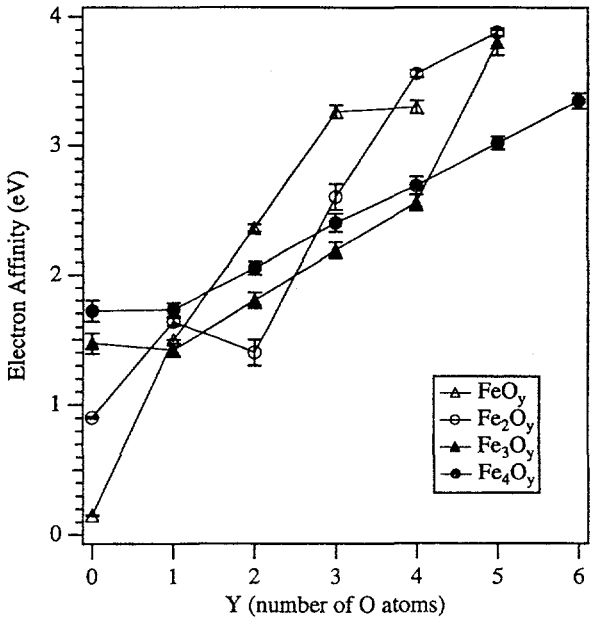

Figure 4.7. The electron affinity of Fe_xO_y clusters versus the number of O atoms.

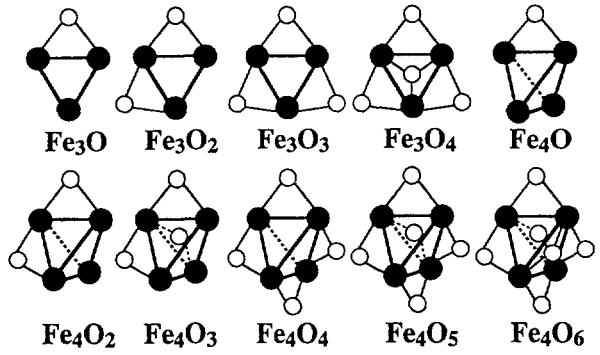

Figure 4.8. Proposed structures for the Fe_3O_y and Fe_4O_y oxide clusters.

References

1. H. Wu, S. R. Desai, and L.-S. Wang, *Phys. Rev. Lett.* 77, 2436 (1996).
2. H. Wu, S. R. Desai, and L.-S. Wang, *J. Phys. Chem.* **101**, in press (1997).
3. L.-S. Wang, H. Wu, and S. R. Desai, *Phys. Rev. Lett.* **76**, 4853 (1996).

Study of Transition-Metal–Carbon Mixed Clusters[1]

L. S. Wang, S. Li, C. F. Ding,* and X. Li†*

Supported by the National Science Foundation.

*Postdoctoral Research Fellow, WSU.
†Washington State University.

We are studying the structure and formation of metal carbide clusters (M_xC_y) in the gas phase and the nanomaterials formed by these clusters in the condensed phase. The gas-phase study involves anion photoelectron spectroscopy, which yields electronic structure and vibrational information of the clusters. We aim for a fundamental understanding of the structure and bonding of the M_xC_y clusters in a wide size range and to understand the subtle differences in bonding and structures between carbon and the transition metals across the first transition series. The gas-phase studies will lead to insight into the formation mechanisms of three classes of novel materials: endohedral metallo-fullerenes, single-shell carbon nanotubes, and metallo-carbohedrenes (met-cars), for their formation depends on the interaction between carbon and the transition metals, and exhibits certain trends among the transition metals. Microscopic understanding of the formation of these materials requires a thorough characterization of M_xC_y clusters and how their structure and bonding evolve as the cluster size increases. This will lead to more efficient methods to synthesize

these novel materials and to design new cluster materials involving carbon and transition metals.

We have performed the first photoelectron spectroscopy experiments on a metallo-carbohedrene, $Ti_8C_{12}^-$, to obtain electronic structure information. The $Ti_8C_{12}^-$ anion is produced by laser vaporization of a titanium carbide target (Fig. 4.9); its spectra show an intense threshold feature and two weaker features followed by a gap and additional higher-energy features (Fig. 4.10). The electron affinity of Ti_8C_{12} is found to be 1.05 ± 0.05 eV (adiabatic) and 1.16 ± 0.05 eV (vertical). The surprisingly low electron affinity and the observed electronic features are interpreted using previous theoretical electronic structure information. The current experiments provide the most direct spectroscopic information on the met-car Ti_8C_{12}.

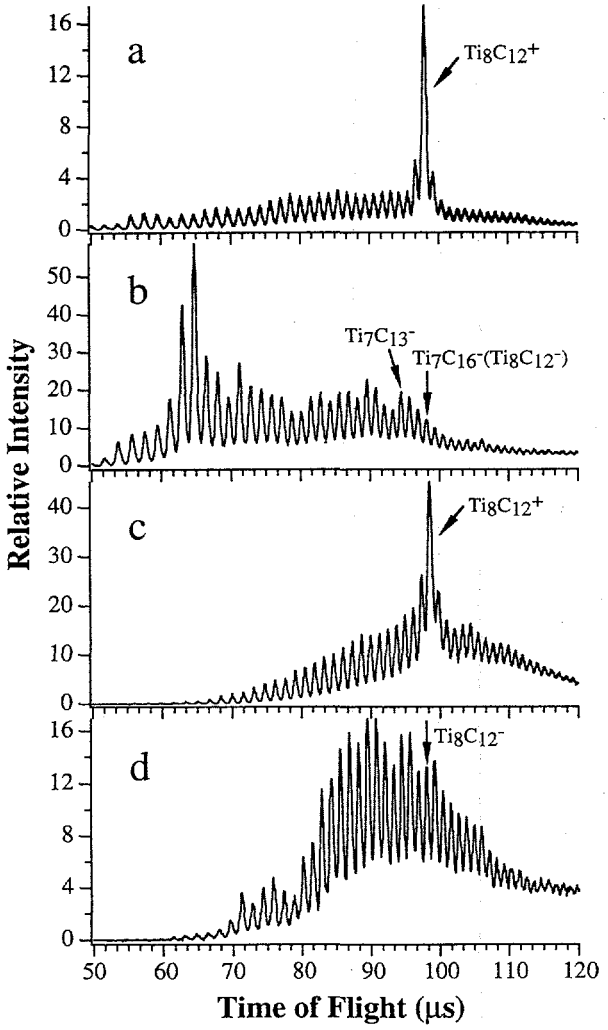

Figure 4.9. (a) Positive-ion mass spectrum of $Ti_xC_y^+$ clusters when a titanium target is vaporized with a 5% CH_4-seeded helium carrier gas, showing the "magic" $Ti_8C_{12}^+$ met-car. Laser vaporization conditions: 10 mJ/pulse at 532 nm, 7-ns pulse width. (b) Negative-ion mass spectrum of $Ti_xC_y^-$ clusters under similar conditions to (a), showing that $Ti_8C_{12}^-$ is not produced. (c) Positive-ion mass spectrum of $Ti_xC_y^+$ clusters when a TiC target is vaporized in neat helium carrier gas, showing $Ti_8C_{12}^+$. Laser vaporization conditions: 3 mJ/pulse at 532 nm, 7-ns pulse width. (d) Negative-ion mass spectrum of $Ti_xC_y^-$ clusters under similar conditions to (c) (7 mJ/pulse), showing significant abundance of $Ti_8C_{12}^-$.

Reference

1. L.-S. Wang, S. Li, and H. Wu, *J. Phys. Chem.* **100**, 19211 (1996).

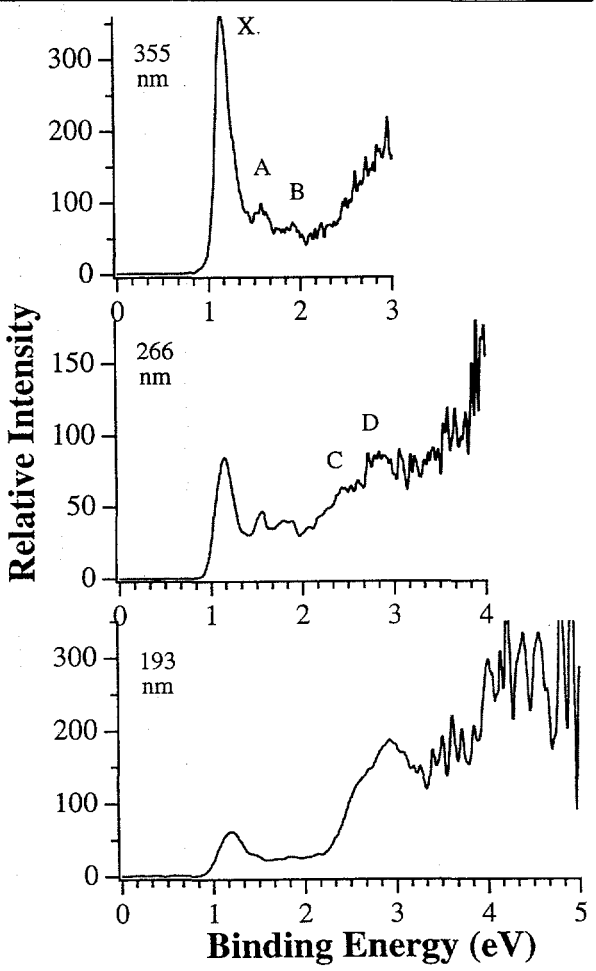

Figure 4.10. Comparison of the photoelectron spectra of $Ti_8C_{12}^-$ at three photon energies: top, 355 nm (3.49 eV); middle, 266 nm (4.66 eV); bottom, 193 nm (6.42 eV).

High-Resolution IR Spectroscopy of Molecules and Clusters

S. W. Sharpe, T. A. Blake,
R. L. Sams, and R. S. McDowell*

Supported by DOE Office of Basic Energy Sciences, with instrument development by Environmental Molecular Sciences Laboratory.

*Associated Western Universities Fellow.

Infrared (IR) spectroscopy is one of several powerful techniques that the physical chemist can call upon for studying the behavior of matter on an atomic scale. In addition, it forms the basis for a suite of analytical techniques that are highly specific and extremely sensitive and can be directly applied to a number of monitoring problems.

High-resolution gas-phase IR spectroscopic techniques have traditionally been plagued by a number of problems including spectral congestion, Doppler broadening, and pressure broadening. Spectral congestion is related to the number of quantum states populated at a given temperature and is determined by Maxwell-Boltzmann statistics. Doppler broadening is related to temperature through the kinetic energy relationship, but also involves the random 3-dimensional motion of the gas molecules. Pressure broadening is related to temperature through the collisional frequency of the molecules, which in turn depends on the density and velocity of the sample. By cooling and reducing the pressure of a gas sample in specially designed cells, these three effects can be minimized, but at the expense of drastically reduced signals.

A technique that takes advantage of the properties of a gaseous sample rapidly expanding into a moderate vacuum has been used in our laboratory for the last six years. A gas sample is expanded through a slit orifice that measures 12 cm in length by 50 μm wide. The resulting ribbon of gas expands at supersonic velocities, and in the process molecules entrained in this ribbon are cooled to a few degrees above absolute zero. In addition, the random 3-dimensional motion of the gas molecules are changed to a 2-dimensional flow with little velocity component in the plane of expansion but perpendicular to the mass flow. If infrared light is used to interrogate the gas molecules through the plane of expansion, spectral congestion, Doppler broadening, and pressure broadening are reduced significantly.

In the past, we have made extensive use of tunable IR lead-salt diode lasers to interrogate the expanding gas. While infrared lasers are ideal light sources in many respects (*i.e.*, extremely high spectral brightness, low noise, narrow bandwidth, and rapid tunability), they are severely limited by narrow spectral coverage. Often an experiment will be determined by what laser coverage is available. Recently, we have succeeded in interfacing a high-resolution Fourier-transform infrared spectrometer (FTIRS) with a continuous slit expansion source (Fig. 4.11). FTIR spectrometry is an alternative to laser sources and offers continuous spectral coverage from the near to far infrared (ca. 15,000 to 10 cm^{-1}). Although FTIR has been used to interrogate molecular beams in the past, these setups utilized a round expansion orifice at moderate spectral resolution. The PNNL FTIRS-beam machine is capable of recording high-resolution ($\Delta\nu \geq 0.0015$ cm^{-1}) spectra at rotational temperatures of 15 K anywhere in the near- to far-infrared spectral region.

This unique instrument has recently been used to complete an infrared spectral investigation of perfluoroethane, a freon substitute. Both a diode laser and the FTIR spectrometer were used in this study. The laser study was of slightly higher resolution and has approximately 10 times the signal-to-noise, compared to the FTIRS results. But despite its lower signal-to-noise, the FTIRS data was comprehensive, covering two entire bands and requiring a fraction of the time to acquire. A similar study of CCl_4 has provided spectral information basic for monitoring this significant green-

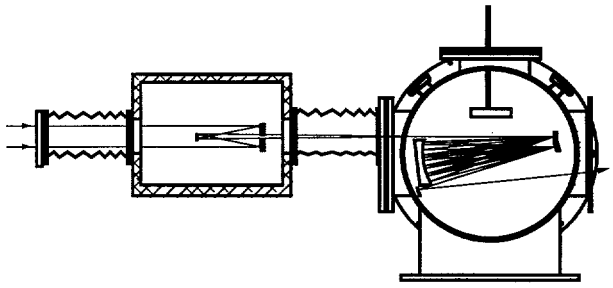

Figure 4.11. Layout of FTIR beam-machine. The box at left contains beam-reducing optics. The supersonic beam is generated at the top of the round chamber.

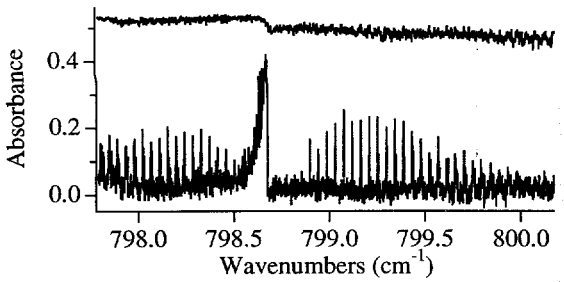

Figure 4.12. Spectra of carbon tetrachloride. Upper trace taken at room temperature at Doppler resolution; lower trace taken in FTIRS beam system.

house gas. Figure 4.12 shows the dramatic increase in resolvable rotational structure provided by expansion cooling.

Spectroscopy and Dynamics of Clusters

A. G. Joly and D. Ray

Supported by DOE Office of Basic Energy Sciences.

The synthesis of clusters in molecular beams affords the opportunity to create model systems exhibiting a rich variety of chemical phenomena. The application of techniques of laser spectroscopy and mass spectrometry to size-selected cluster beams facilitates rigorous studies of fundamental properties (both static and dynamic) of these model systems. The goal of this project is to examine the relationships between cluster structure (geometric and electronic) and function (reaction dynamics and kinetics) in clusters. Comparison of the experimental results with predictions of emerging theoretical models is an important component of this project.

We are currently developing and applying time-domain spectroscopic techniques to determine the geometric structures of clusters. The methods under development are implementations of rotational coherence spectroscopy (RCS), a high-resolution, time-domain spectroscopic method for the determination of the moments of inertia of molecular species isolated in the gas phase. RCS yields the rotational constants of an absorber to an accuracy of 0.1–1% without requiring precise measurement or detailed analysis of individual eigenstates. This has become an established technique, principally through the efforts of Felker and coworkers.[1] In many cases RCS is complementary to high-resolution spectroscopy in the frequency domain. RCS has great utility for providing gross structural data and is a particularly useful technique for species that have prohibitively dense or featureless spectra in the frequency domain.

A photofragmentation-based implementation of RCS, similar to that described by Magnera *et al.*,[2] has been implemented to study ionic clusters. In this approach, the rotational coherence transients are obtained via a psec pump–probe scheme by monitoring the production of photofragments as a function of the time delay between the pump and probe pulses. A rotational coherence transient of Ar_3^+ is shown in Fig. 4.13. There have been very few measurements of the rotational constants of ionic clusters due to the difficulty of generating a large enough sample; the RCS methods we are developing are sufficiently sensitive to measure rotational constants of extremely small numbers of ions and should therefore have wide applicability.

References

1. P. M. Felker, *J. Phys. Chem.* **96**, 7844–7857 (1992).
2. T. F. Magnera, D. M. Sammond, and J. Michl, *Chem. Phys. Lett.* **211**, 378–380 (1993).

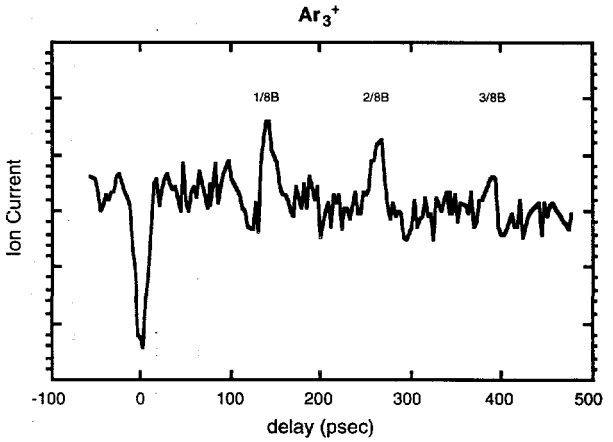

Figure 4.13. Rotational coherence transient of Ar_3^+.

Intrinsic Affinity and Selectivity of Crown Ethers for Alkali-Metal Cations

M. B. More, P. B. Armentrout,* and D. Ray*

Supported by DOE Office of Basic Energy Sciences and the National Science Foundation.

*Department of Chemistry, University of Utah.

Noncovalent interactions between ions and neutral molecules are of fundamental importance in molecular recognition phenomena occurring in complex chemical and biochemical systems.[1] The study of a series of cation–ether complexes composed of different metal cations and a selection of ligands ranging from simple, monodentate ethers to cyclic polyethers provides an opportunity to examine the noncovalent interactions operative in "simple" ion–molecule complexes. Cation–ether complexes are also interesting from a practical point of view: crown ethers have been proposed for use in new chemical separations technologies[2] and in the development of advanced analytical methods.[3] Computational models capable of reliably predicting ligand selectivity in a variety of condensed-phase environments would be valuable tools for the advancement of separations technologies. Such methods are currently under development; however, the development is hindered by a lack of suitable experimental data. One goal of the present work is to provide accurate experimental data to address this deficiency.

Accurate measurement of the intrinsic properties of cation–ether complexes is the principal challenge from the experimental perspective. Studies of ion–molecule complexes in the gas phase can provide insight into the intrinsic aspects of the interactions, because the isolated complexes are unperturbed by solvent-induced phenomena. In the present work, collision-induced dissociation (CID) cross-section measurements are made with a guided ion-beam mass spectrometer, an instrument specifically designed for measurements of the kinetic-energy dependence of collision-induced phenomena. The cross-section thresholds are interpreted to yield 0 and 298 K bond dissociation energies after accounting for the effects of multiple ion–molecule collisions, internal energy of the complexes, and unimolecular decay rates. Measurements have been made on complexes of simple and complex ethers (dimethyl ether; 1,2-dimethoxyethane; 12-crown-4, triglyme; 15-crown-5 and 18-crown-6) with the alkali metal cations.[4] These experiments provide the first benchmark data for *ab initio* electronic structure calculations of the selectivity and affinity of macrocyclic ligands for ions.

The experimentally determined bond dissociation energies for the complexes are in close agreement with conventional ideas of electrostatic ligation of gas-phase ions and with recent *ab initio* calculations by Feller and coworkers.[5] Correlations between the bond dissociation energies and the calculated equilibrium structures[5] demonstrate that the orientation of the C–O–C moieties relative to the metal cation can be more important than the M^+–O bond length in determining the stability of the complexes, as predicted by Hay *et al.*[6,7]

References

1. See, for example, D. A. Dougherty, *Science* **271**, 163 (1996); A. D. Buckingham and S. M. Roberts, eds., *Principles of Molecular Recognition* (Blackie Academic and Professional, Glasgow, 1993).
2. E. P. Horwitz, M. L. Dietz, and D. E. Fisher, *Solvent Extract. Ion Exchange* **9**, 1 (1991).
3. J. W. Grate, R. Strebin, J. Janata, O. Egorov, and J. Ruzicka, *Anal. Chem.* **68**, 333 (1996).
4. M. B. More, E. D. Glendening, D. Ray, D. Feller, and P. B. Armentrout, *J. Phys. Chem.* **100**, 1605 (1996); D. Ray, D. Feller, M. B. More, E. D. Glendening, and P. B. Armentrout, *J. Phys. Chem.* **100**, 16116 (1996); M. B. More, D. Ray, and P. B. Armentrout, *J. Phys. Chem.*, in press; M. B. More, D. Ray, and P. B. Armentrout, *J. Phys. Chem.*, submitted.
5. S. E. Hill, E. D. Glendening, and D. Feller, *J. Phys. Chem.*, submitted; E. D. Glendening, S. E. Hill, and D. Feller, *J. Phys. Chem.*, in press.
6. B. P. Hay and J. R. Rustad, *J. Am. Chem. Soc.*, **116**, 6316 (1994).
7. B. P. Hay, J. R. Rustad, and C. J. Hostetler, *J. Am. Chem. Soc.* **115**, 11158 (1993).

5. Miscellaneous

Near-Infrared Spectroscopy for Trace Atmospheric Monitoring

*S. W. Sharpe, T. A. Blake, and R. L. Sams**

Supported by DOE Office of Basic Energy Sciences, with instrument development by Environmental Molecular Sciences Laboratory.

*Associated Western Universities Fellow.

With the rapid technological growth of the telecommunications industry, near-infrared semiconductor lasers are becoming readily available. Although originally intended for high-speed data transmission, these devices can also be packaged for spectroscopic applications, where tunable and spectrally narrow radiation is required. One such application involves atmospheric monitoring for a variety of trace species.

The decision to base an instrument on the far-, mid-, or near-infrared spectral region(s) must be driven both by fundamental and technological issues. The far-infrared region is densely populated with the pure rotational lines of water. In addition, laser sources for the far-infrared region are still experimental and not easily implemented in the field. Both the mid- and near-infrared spectral regions offer atmospheric spectral windows that are largely free from absorption by common interferents such as water and carbon dioxide. Figure 5.1 shows an absorbance spectrum typical of clean air; note the three prominent atmospheric windows centered at 4500 cm^{-1} (2.2 μm), 6200 cm^{-1} (1.6 μm) and 8000 cm^{-1} (1.25 μm). Strictly speaking, there are "micro" windows between the individual water-vapor lines in both the mid- and near-infrared regions. As we will see, these micro windows can also be exploited.

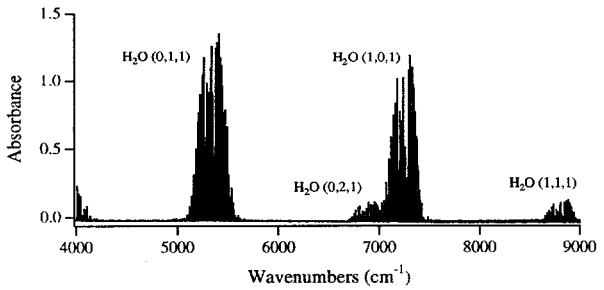

Figure 5.1. Near-infrared spectrum of "clean" air (10-m path at 24°C; spectral resolution 0.05 cm^{-1}).

Currently, mid-infrared tunable diode laser sources require bulky cooling equipment, excluding them from being incorporated in a hand-held device. Mid-infrared devices typically need to be cooled to liquid nitrogen temperature for proper operation. The next decade may see important developments in room-temperature, tunable mid-infrared diode lasers capable of miniaturization.

Fortunately, room-temperature (or Peltier cooled), tunable, near-infrared (NIR) semiconductor diode lasers are commercially available for 5000–13,000 cm^{-1} (0.77– 2 μm). The NIR region corresponds to overtones and combinations of fundamental vibrations. These higher-order vibrations are typically reduced in intensity by 10 to 100 times from their corresponding fundamentals, representing a fundamental disadvantage of operating in the near infrared. To some extent, the reduced absorption cross section inherent of the near-infrared is offset by the extreme spectral brightness associated with NIR lasers and the high spectral response and low noise of NIR detectors.

Laser-Based Detection of Chemical Contraband

S. W. Sharpe, R. G. Clemmer, J. F. Kelly,† S. W. Martin,* and G. M. Mong§*

Supported by internal National Security funding.

*National Security Division.
†Energy Division, Sensors and Measurement Systems Department.
§Materials and Chemical Sciences Department.

The goal of this work is to develop a portable and rapid laser-based air sampler for detection of specific chemical contraband and to compile a spectral database in the near infrared of sufficiently high quality to be useful for gas-phase spectroscopic identification of chemical contraband.

The synthesis or "cooking" of illicit chemicals may release relatively high concentrations of solvents, precursors, and byproducts. In some instances,

the final product (*e.g.*, methamphetamine) may have sufficient vapor pressure to be itself detectable in the surrounding air. The detection of a single high-value effluent or the simultaneous detection of two or more low-value effluents suggest a nearby clandestine operation. The designation of high- versus low-value effluent reflects both the commercial availability and legitimate usage of a specific chemical.

Methamphetamine can be manufactured by any of several synthetic routes. The three procedures outlined below represent the most commonly encountered syntheses. Specific chemicals that can be detected in the near or mid infrared and used as indicators of methamphetamine production are indicated with an asterisk (*).

Amination-reduction of phenylacetone

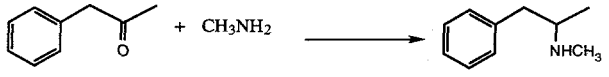

1 2 3

This process requires that *phenylacetone (1) be dissolved in an alcohol. The specific alcohol is determined by economic factors and availability; *isopropanol is often employed. *Methylamine (2) is then added to the mixture and aluminum amalgam is used as a reducing agent. *Methamphetamine (3) produced by this route is in the free-base form, and has appreciable vapor pressure under typical ambient conditions (~1.5 Torr).

Both methamphetamine and phenylacetone are Schedule-II substances and represent high-value effluents. Methylamine is listed as a Schedule-II controlled immediate precursor and is also considered to be a high-value effluent if detected in vicinities remote from major industrial settings. Isopropyl alcohol would be considered a low-value effluent under most conditions.

Deoxygenation of ephedrine/pseudoephedrine

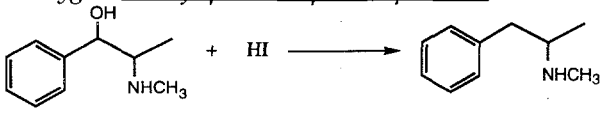

4 5

Ephedrine or pseudoephedrine salts (4) are commercially available in nonprescription cold remedies. Ephedrine/pseudoephedrine in bulk form (25-lb. bags) is frequently encountered in methamphetamine production processes; the source is frequently the Orient. In this process, the ephedrine or pseudoephedrine salt is deoxygenated by *hydriodic acid (5) in the presence of red phosphorus. This route presents an entirely different challenge to detection-at-a-distance, for the only volatiles are HI and the attendant iodine product.

Here, the detection mode for volatiles must focus on inorganic agents (HI, I_2) as the only reasonable signatures for manufacture. Other unrelated work here at PNNL has indicated that the presence of iodine species in ordinary air (Eastern seaboard) is very low (1–10 ng/m^3). Amounts exceeding this value would be an excellent indication of methamphetamine manufacturing; HI would thus be considered as a high-value effluent.

Leuckart-Wallach process

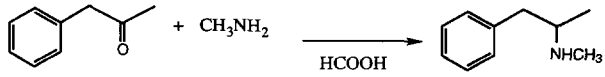

6

The Leuckart-Wallach route is less common; it utilizes *formic acid (6) or ammonium formate as a reductant of intermediate imines (similar to the function of aluminum in the amalgam method). The presence of formate/*formaldehyde in the atmosphere should be interpreted with caution; note, however, that this method is in conjunction with phenylacetone in equimolar proportion.

Near-Infrared Spectral Maps

Near-infrared spectral maps at the requisite resolution (better than 0.02 cm^{-1}) do not exist for many of the species of interest to this project. As a consequence, these spectra were taken on the EMSL Bruker 120HR Fourier-transform infrared spectrometer in a long-path-length White-type cell. Some of these spectra are shown in Figs. 5.2–5.5.

Both hydrogen iodide and methylamine are considered high-value effluents, because they are neither readily available nor commonly used. Both substances have vapor pressures greater than 1 atmosphere at room temperature, making them excellent indicators of methamphetamine cooking. Taken individually, neither formic acid nor isopropanol should be considered high-value effluents, although the simultaneous detection of both formic acid and isopropanol can be taken as a good indicator of a cooking event. Methanol and ammonia have been included for purposes of detection-limit comparison.

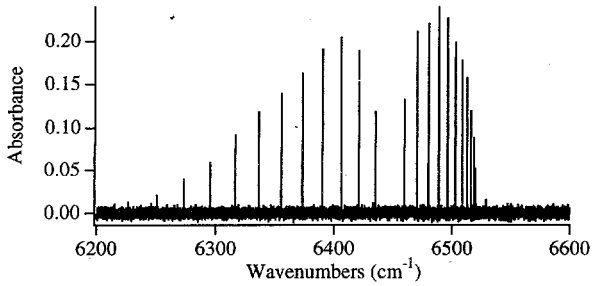

Figure 5.2. Hydrogen iodide in the 2nd overtone region. Such "stick" spectra are most amenable to laser detection.

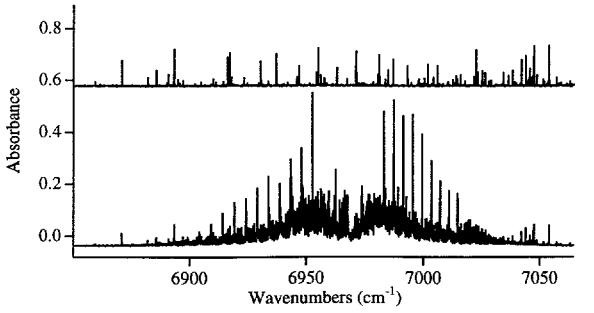

Figure 5.3. Vapor spectra of formic acid (lower) and water (upper). Sharp formaldehyde features can be found between the many water lines.

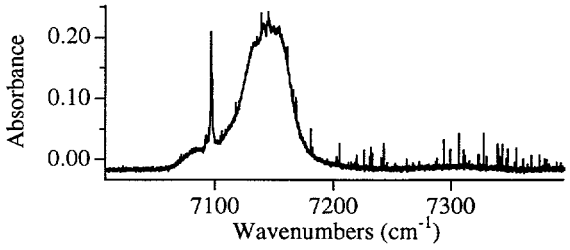

Figure 5.4. Isopropyl alcohol. Note the extremely sharp feature to the red of the main OH overtone band.

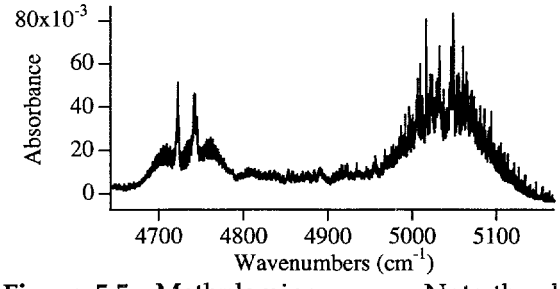

Figure 5.5. Methylamine vapor. Note the sharp features riding on a broad continuum.

Species	Detection Limit (ppb)
ammonia	20
formic acid	115
HI	100/214 (at 2.3/1.6 μm)
methanol	125
isopropanol	326
methylamine	1500

Disease Diagnosis and Laser-Based Breath Analysis

*S. W. Sharpe, J. J. Toth,**
R. L. Sams,† and K. D. Thrall§

Supported by Laboratory Directed Research and Development (Medical Technologies).

*Environmental Technology Division, Systems and Risk Management Department.
†Associated Western Universities Fellow.
§Molecular Bioscience Department.

The bacterium *Helicobacter pylori* has been directly implicated as the leading cause of gastritis and indicated in stomach cancer. It is estimated that 50% of the world population and 30% of the U.S. population are currently infected. The bacterium is found under the thick mucus layer of the stomach and produces large amounts of urease, which is thought to be released by the bacterium to control the local pH at the infected site:

$$O{=}C(NH_2)_2 + H^+ + 2H_2O \rightarrow$$
$$(\text{urease}) \rightarrow HCO_3^- + 2(NH_4)^+.$$

Currently accepted FDA diagnosis involves biopsy and culturing of the stomach lining, which costs about $500, not including time lost from work, and is both time consuming and invasive, requiring the patient to be under a general anesthetic.

The goal of this work is to develop a portable and rapid laser-based breath analyzer for the diagnosis of the *Helicobacter pylori* infection in humans. Small infrared-active molecules such as ammonia, carbon monoxide, and nitrous oxide are all present in exhaled breath and can be readily detected by laser absorption spectroscopy. In addition, many of the stable isotopomers of these molecules can be accurately detected, making it possible to follow specific metabolic processes. We describe a near-infrared laser-based system for detecting ammonia in human breath, and its possible application in a rapid, noninvasive diagnostic tool for *Helicobacter pylori*.

Applications of tunable infrared semiconductor lasers to breath analysis have been reported in the literature by a number of researchers.[1–7] Advantages of laser absorption over more conventional techniques such as Fourier transform infrared (FTIR)[8] and nondispersive[9] spectroscopies include higher sensitivity, greater spectral resolution, faster data acquisition, and potentially compact packaging of the apparatus for field deployment.

Generally, breath analysis occurs after preconditioning and/or preconcentrating the exhaled breath. This may involve passing the breath over a suitable desiccant, through a cold trap, or mixing with an inert diluent to reduce water vapor. The sample may then be preconcentrated by bubbling through an appropriate solvent/indicator or condensed to remove only the "active" species. Detection of selected species is subsequently performed using mass spectroscopy, scintillation spectroscopy, colorimetric spectroscopy, or gas chromatography, and more recently gas-phase infrared absorption spectroscopy. Gas-phase IR spectroscopy has the advantage of requiring minimal preconditioning and/or preconcentration of the sample prior to analysis.

The apparatus for acquiring and analyzing exhaled breath consists of three subunits including the sampling cell, the laser system, and detection/data acquisition electronics.

A rapid-scan procedure is used to acquire the spectral data. A breath sample is continuously pulled through the sampling cell for the duration of the measurement. No preconcentration is employed. Pressure in the sampling cell is maintained at <80 Torr by throttling the inlet. As the sample is pulled through the sampling cell, repeated laser scans (500 scans/sec) are acquired via a 12-bit transient digitizer, and the resulting digital data are co-added by a microcomputer. Each laser scan starts at the same initial spectral frequency and covers a spectral region of approximately 7500 MHz. Approximately 150 scans can be averaged in 0.3 seconds. The initial spectral frequency will depend on the absorber of interest.

Both a long optical path length and a reduced operating pressure can be obtained by utilizing a modified Herriott cell consisting of two concave, slightly astigmatic mirrors that are separated by 55 cm. One of the mirrors is fastened to a kinematic mount that allows for translational and angular adjustments; the second is fastened to a rigid base plate. A Pyrex tube surrounds the mirrors so that the 3-liter volume between them can be evacuated and/or filled with a sample. The mirrors are configured to allow the output of an infrared diode laser to be reflected between them 182 times, for a total optical path length of 100 m. This modified design reduces fringing effects caused by feedback of the laser that is common to all multipass optical systems.

High spectral brightness (0.5 mW) and narrow line widths (20 MHz) make tunable GaAs near-infrared diode lasers, similar to those found in CD players and telecommunications equipment, ideal light sources for detection of Doppler-limited samples. These sources are commercially available throughout the near-infrared region (0.6–3 μm). The source includes temperature stabilization and laser frequency scan electronics. We use epitaxial indium gallium arsenide (InGaAs) detectors and a high-speed current preamplifier to increase the signal output. The signal is delivered to an oscilloscope and a transient digitizer, both of which are triggered synchronously with the ramping of the diode laser. (The oscilloscope trace allows the operator to align and optimize the apparatus in real time, but is not required.)

Selection of the appropriate spectral features is of critical importance, because it determines the sensitivity of the technique and its immunity to interfering gases (H_2O, CO_2). Since relatively few high-resolution gas-phase near-infrared spectra exist, we recorded the requisite spectral maps for vapor phase water and ammonia ($^{15}NH_3$ and $^{14}NH_3$). A portion of these spectral maps appears in Fig. 5.6.

To calculate absolute absorbance values and avoid problems associated with changes of laser power vs. frequency, a "zero" wave form is recorded with the laser off, and a "baseline" wave form is generated, associated with the I_0 of the spectral wave form and created by fitting the data wave form to a polynomial. The final I/I_0 wave form is related to transmittance, and can be converted directly to absorbance. The individual peaks are then fit to a Gaussian, Lorentzian, or Voigt profile, depending on the pressure region.

The theoretical absorbance limit of this apparatus (dictated by shot noise) is predicted to be ~10^{-8}.

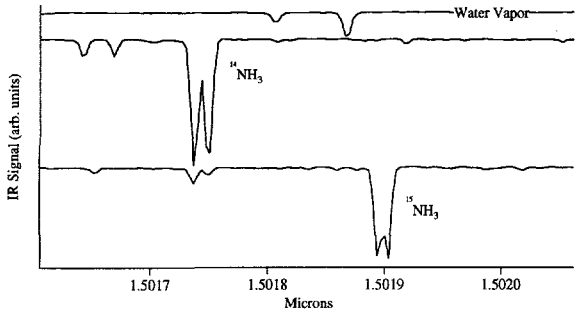

Figure 5.6. A small region of the near-infrared spectral maps for water and ammonia. Data taken on the EMSL high-resolution FTIRS at 0.02 cm^{-1} resolution. Stronger ammonia transitions correspond to the $\nu_1 + \nu_3$ $^{R}R(^{4}4 \leftarrow {}^{3}3)$ transition.

Sensitivity is approximately 10^{-4} absorbance units, limited by the presence of fine fringes traced to étaloning within our Herriott cell. In some cases, we can improve the sensitivity by a factor of 10 with use of optimal filtering, which consists of convolving the normalized spectral data with an appropriate response function, determined *a priori*. We can thus observe absorbance signals corresponding to tens of parts per billion (by volume) of a specific absorber, which is equivalent to a partial pressure of approximately 10^{-6} Torr of absorber in one atmosphere of sample; see Fig. 5.7.

Two tests have been considered for the PNNL preliminary human studies. The first involves tagging urea with ^{15}N, which is non-radioactive and has a natural abundance of 0.37%, making it an ideal taggent for this project:

$$O{=}C(^{15}NH_2)_2 + H^+ + 2H_2O \rightarrow$$
$$(\text{urease}) \rightarrow HCO_3^- + 2(^{15}NH_4)^+.$$

While the FDA has approved untagged urea for human tests, $O{=}C(^{15}NH_2)_2$ has not yet been approved. We have therefore defaulted to a second testing option, looking for an incremental increase in untagged ammonia in exhaled breath. The testing protocol is as follows:

- Have patient read and sign consent form
- Administer serological test for *H. pylori*
- Have patient give three baseline breaths
- Administer untagged urea cocktail
- Take breath samples at intervals of 0, 2, 6, 8, 12 and 20 minutes.

A portion of a typical test spectrum appears in Fig. 5.8. A large number of such data sets will be required to build a statistical model for normal vs. infected persons.

We are currently involved in acquiring new data sets, and anticipate definitive results confirming or denying the utility of this test in early 1997.

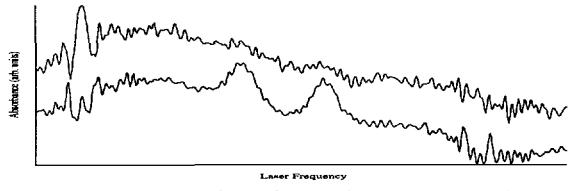

Figure 5.7. Raw data from the transient digitizer, showing the absorption profile of an ammonia doublet transition at ~1.5 μm. The upper trace is of room air; the lower corresponds to approximately 500 ppb ammonia in exhaled breath.

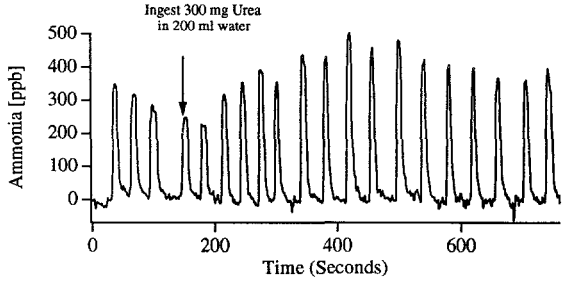

Figure 5.8. Test data from an *H. pylori*–negative patient. Each feature corresponds to an individual exhalation into the instrument. Note the apparent decrease followed by increase of ammonia after ingesting the sample.

References

1. Y. Higashi, H. Ohohara, and Y. Sasaki, "Stable isotope analysis using tunable diode laser spectroscopy and its application to ^{13}C breath test," *Igaku* **4**, 8–9 (1994).
2. R. U. Martinelli, R. J. Menna, D. E. Cooper, C. B. Carlisle, and H. Riris, "Near-infrared InGaAs/InP distributed-feedback lasers for spectroscopic applications," *Proc. SPIE* **2148** (*Laser Diode Technology and Applications VI*) 292–307 (1994).
3. K. L. Moskalenko, A. I. Nadezhdinskii, and E. V. Stepanov, "Tunable diode laser spectroscopy application for ammonia and methane content measurements in human breath," *Proc. SPIE* **2204**, 448–452 (1993).
4. K. L. Moskalenko, N. V. Sobolev, I. A. Adamovskay, E. V. Stepanov, A. I. Nadezhdinskii, and S. McKenna-Lawlor, "Tunable diode

laser application for fully automated absolute measurements of CO and CO_2 concentrations in human breath," *Proc. SPIE* **2205**, 440–447 (1993).
5. D. E. Cooper, R. U. Martinelli, C. B. Carlisle, H. Riris, D. B. Bour, and R. J. Menna, "Measurement of $^{12}CO_2/^{13}CO_2$ ratios for medical diagnostics with 1.6-μm distributed-feedback semiconductor diode lasers," *Appl. Opt.* **32**, 6727–6731 (1993).
6. U. Lachich, S. Rotter, E. Shlomo, and U. El-Hanany, "Tunable diode laser based spectroscopic system for ammonia detection in human respiration," *Rev. Sci. Instr.* **58**, 923–927 (1987).
7. T. A. A. Alobaidi and D. W. Hill, "Helium-neon laser infrared analyzer for alcohol vapor in the breath," *J. Phys. E* **8**, 30–32 (1975).
8. A. Franzblau, S. P. Steven, L. Burgess, A. Qu, R. M. Schreck, and J. B. D'Arcy, "The use of a transportable Fourier transform infrared (FTIR) spectrometer for the direct measurement of solvents in breath and ambient air," *Amer. Ind. Hyg. Assoc. J.* **53**, 221–227 (1992).
9. B. Conlon and J. Dittmar, "Multiple-component nondispersive infrared gas analyzer," Patent: Criticare Systems, Inc. (1992).

Asymmetric RF Ion Trap and Simultaneous Anion/Cation Detection

S. E. Barlow, M. L. Alexander, and J. C. Follansbee†*

Supported by DOE Office of Basic Energy Sciences.

*Materials and Chemical Sciences Department.
†EMSL Computing and Information Sciences.

The use of Paul-type RF ion traps as analytic mass spectrometers has become widespread; at least four commercial versions of these instruments are now available. All of these devices operate using principles first described by Paul[1] in 1950. Paul's ideas, for which he was awarded a Nobel prize in 1989, took advantage of the stability/ instability character of Mathieu's equation:

$$\ddot{z} + [a - 2q\cos(2t)z] = 0, \qquad (1)$$

where a and q are constants and t is the independent variable. This equation with its periodic coefficients cannot be solved by elementary means.[2,3] However, Mathieu's equation goes through regions of stability and instability as a function of the parameters a and q. A reasonably detailed discussion of Mathieu's equation as related to Paul traps is given in March and Hughes.[4]

An interesting feature of the Paul trap is that it can simultaneously store both cations and anions. Further, the various detection schemes that are used for mass identification affect ions of either charge more or less equally. Many currently available ion traps are equipped with detectors that allow the user to select which charge-sign ions are examined. In principle, one should be able to simultaneously generate mass spectra of both charges, but in practice the detectors are subject to large shot-to-shot signal fluctuations and therefore require considerable averaging to produce high-quality spectra, and no particular advantage accrues through the added complications of dual detection. The developments described below should greatly reduce this problem and open the way to new analytic capabilities.

The Harmonic Trap with Asymmetric Hyperbolic Electrodes

Equation (1) implies the existence of a harmonic field, and three-dimensional trapping requires

fields in all directions. If these fields are harmonic and cylindrically symmetric, then we have a harmonic trapping potential, Eq. (2). The use of electrode structures that accurately produce quadratic electrostatic potentials has been widely investigated. Several different schemes to achieve this result to one degree or another have been proposed and successfully demonstrated.[1,4–6] The quadratic or quadrupolar electrostatic potential has several attractive features for use in mass spectrometric applications and precision measurements. First among these is a simple-to-understand, mathematically analytic form,

$$\Phi(r,\theta,z) = \frac{V}{D^2}\left(r^2 - 2z^2\right) + \Phi_o \qquad (2)$$

where $\Phi(r,\theta,z)$ is the electric potential in cylindrical-polar coordinates, V is an applied "trapping" voltage that may contain both DC and RF terms, D is a quantity that describes the trap's geometry and size, and Φ_o is an arbitrary constant that allows us to define the potential zero. Figure 5.9 shows a plot of Eq. (2), where we have set $\Phi_0 = 0$ and $V/D^2 = -1$. In Fig. 5.10 we have replotted Eq. (2) as a contour plot, and it becomes apparent the a three-dimensional quadrupole potential will be produced when appropriate hyperbolic electrodes are selected, as is well-known.[1,5] An example is illustrated in Fig. 5.11. When hyperbolic electrodes are used, D is defined by:

$$D^2 = \frac{1}{2}r_o^2 + z_o^2, \qquad (3)$$

where r_0 is the radius of the central ring electrode at $z = 0$, and z_0 is the distance to an end-cap electrode at $r = 0$. Then Eq. (2) can be rewritten as

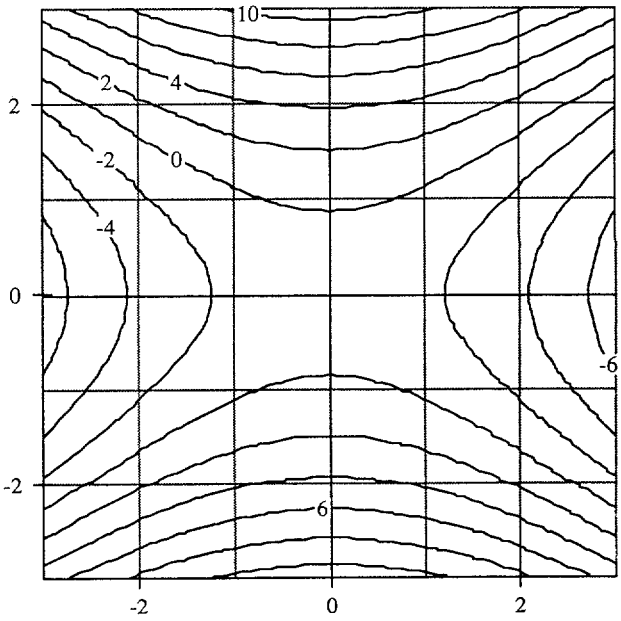

Figure 5.10. Contour plot of the saddle potential.

$$\Phi(r,\theta,z) = \frac{V}{D^2}\left(r^2 - 2z^2\right) + V\left(1 - \frac{r_o^2}{D^2}\right). \qquad (4)$$

In the language of mathematics, the ring electrode is a confocal hyperboloid of one sheet,and the end-cap electrodes are confocal hyperboloids of two sheets. The particular value of the constant term

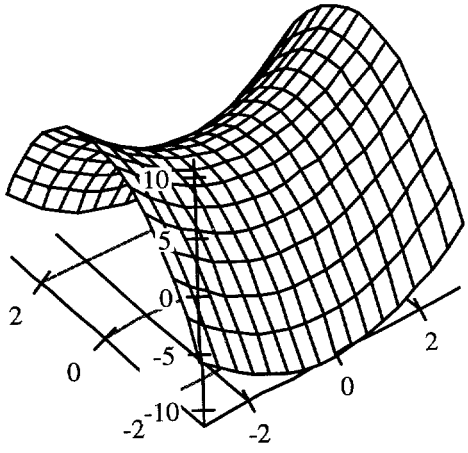

Figure 5.9. Saddle potential.

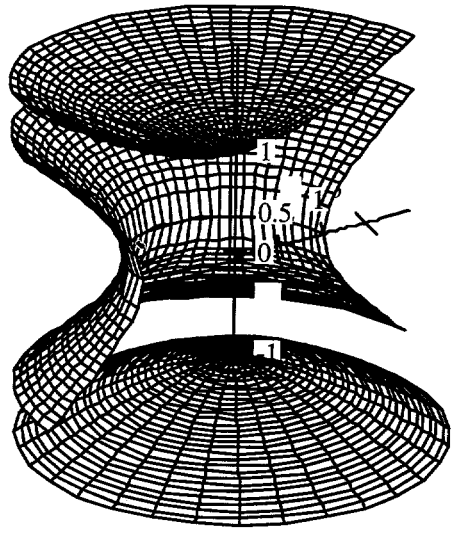

Figure 5.11. Hyperbolic electrode cutaway. The radius of the ring electrode in the $z = 0$ plane is r_0, while the distance from the origin to the nearest point on the end-cap electrode is z_0.

in Eq. (4) gives the ring electrode a potential value of V and the end caps a value of $-V$ and has been chosen for reasons of symmetry and to simplify later developments. Up to this point, we see that the choice of r_0 and z_0 are arbitrary *and* independent of one another. In any case, all allowed end-cap and ring structures have the same asymptotes,

$$z = \pm\frac{1}{\sqrt{2}}r. \qquad (5)$$

This gives a trap designer freedom to tailor the trap size to meet specific needs. In practice, the trap electrodes are truncated and this can introduce field errors, as can machining imperfections.[6] Referring back to Fig. 5.11, we see that although the ring electrode by necessity has a plane of symmetry through it in the $z = 0$ plane, it is *not* essential that the end caps be chosen as members of the same confocal hyperboloid of two sheets. Rather, we are free to choose *any* two end caps, provided only that they belong to the family of hyperboloids described by Eq. (5). However, if we do choose to make them different, the trap biasing required to make a harmonic well will be more complex. Returning now to Eq. (4), we can set $\Phi(r,\theta,z)$ first to V to give the equation for the ring electrode:

$$z_{ring} = \pm\sqrt{\frac{r^2 - r_o^2}{2}}, \qquad (6)$$

and for the end cap with z_0, $\Phi(r,\theta,z) = -V$ we find

$$z_{endcap} = \pm\sqrt{\frac{r^2 + 2z_o^2}{2}}. \qquad (7)$$

The boundary choice of $\pm V$ on the electrodes is quite arbitrary up to this point, but if we now set $\Phi(r,\theta,z) = 0$, we find a new end-cap possibility with

$$z_{Newendcap} = \pm\sqrt{\frac{1}{2}r^2 - \frac{1}{4}r_o^2 + z_o^2}. \qquad (8)$$

An example of this geometry is shown in Fig. 5.12. A brief consideration of Eqs. (6) to (8) shows that to actually construct such a trap, we must have $z_0 > r_0$. If we designate that point on the new end cap when $r = 0$ we can define

$$z_n^2 = z_o^2 - \frac{1}{4}r_o^2. \qquad (9)$$

Aside from some essentially trivial changes in biasing, the major difference between the symmetric and asymmetric trap is the energy an ion needs to reach the end cap. The energy ratio between the nearer and farther end cap is given by z_n^2/z_0^2. This fact along with the biasing choice suggested in Fig. 5.12 describe two of the three free parameters that a trap designer actually has at his disposal. The final parameter is just the overall scale of the trap, set now by r_0 (or z_0 or z_n).

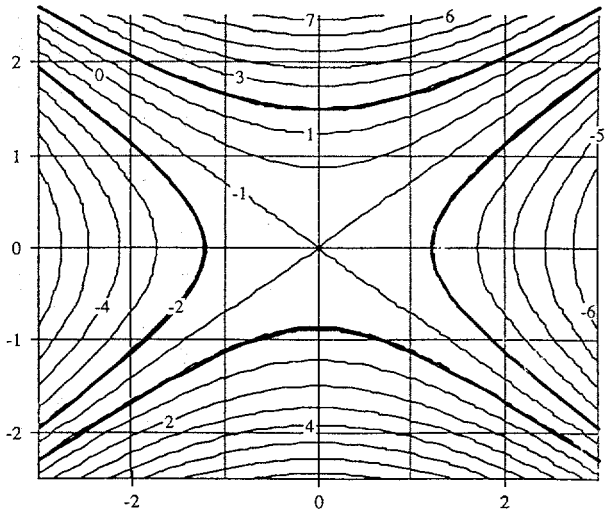

Figure 5.12. Contour plot of an asymmetric harmonic trap showing RF biasing.

Note: From the discussion below, a reader may wish to retrofit an existing trap to take advantage of the benefits of asymmetry. Because most commercial instruments have $z_0 < r_0$, the appropriate modification is to construct the more distant electrode with a new z_0. The relationship between the old and new z_0 is

$$z_{newo}^2 = z_{oldo}^2 + \frac{1}{4}r_o^2, \qquad (10)$$

which follows directly from Eq. (8).

Simultaneous Cation and Anion Detection

Two types of ion detection are of general applicability in ion traps: image current and ion collection. In the former method, ions are resonantly excited, and the resulting image current transient is monitored and Fourier transformed (or some equivalent process). Such methods have been attempted with varying degrees of success in the Paul trap.[4,7] However, ion–ion and ion–neutral dephasing collisions make this technique much less attractive than in the case of the Penning trap in Fourier-transform mass spectrometry. Further, because we ultimately intended to make use of the trap for simultaneous detection of both cations and anions, the inability to distinguish charge sign

makes image current methods undesirable. We conclude that it is desirable to eject ions from the trap through one and only one of the end caps and then direct them to separate collectors depending on their charge sign. This is, of course, similar to the standard method of ion detection for RF-trap mass spectroscopy. The need to know which end cap the ion will exit can be predetermined by employing the asymmetric trap design described above.

Depending on the method of ion ejection, ions will exit the trap with some energy dispersion. In the application considered here the ions may consist of cations, anions, or both, so it is necessary to first separate the two types and send each to its appropriate detector. Figure 5.13 illustrates schematically how this might be accomplished. Note that the detectors are actually folded back from the line of sight of the ejection port. This geometry actually has two advantages: first, it opens the ejection port itself for additional probes, *e.g.*, an electron gun or laser; second, in the event that one chooses to use instability ejection, the ions will possess a very large energy dispersion; the curved trajectory from the end cap to the detector will cause higher-energy ions to take a longer path and thus produce some energy focusing. This energy focusing is somewhat akin to techniques used in time-of-flight mass spectrometers and should improve spectral quality. This supposition has been verified by trajectory modeling calculations, which also indicated that the 90° angle between the detectors is nearly optimal for this purpose.

With suitable modification of the biasing scheme, this trap should be able to perform all of the functions currently available in commercial instruments. However, its attractiveness lies in the *extension* of current capabilities. In particular, we expect that the asymmetric electrode design will produce superior quality spectra. Further, the improved spectra should allow us to analyze particularly difficult samples that have large inhomogeneities, such as environmental aerosols

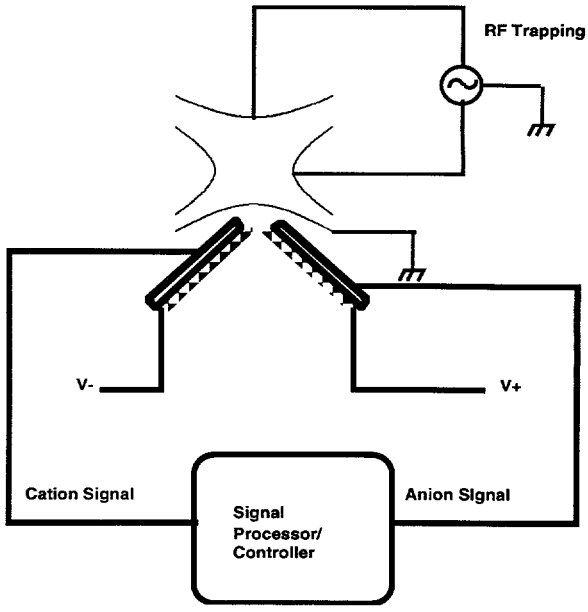

Figure 5.13. Asymmetric trap with dual detectors.

where one cannot be certain from one measurement to the next that the analyte is the same. Patents on this approach are pending.

References

1. W. Paul and H. Steinwedel, *Z. Naturforsh.* **8a**, 448 (1950).
2. G. Blanch, in *Handbook of Mathematical Functions,* M. Abramowitz and I. A. Stegun, eds., U.S. Government Printing Office (1964), Chapt. 20.
3. N. W. McLachlan, *Theory and Application of Mathieu Functions*, Clarendon Press, Oxford (1947).
4. R. E. March and R. J. Hughes, *Quadrupole Storage Mass Spectroscopy*, J. Wiley & Sons, New York (1989), p. 396.
5. J. R. Pierce, *Theory and Design of Electron Beams,* 2nd ed., Van Nostrand, New York (1954), p. 41.
6. G. Gabrielse, *Phys. Rev. A* **29**, 463 (1984).
7. S. Jefferts, private communication (1996).

Near-Field Optical Tweezers

L. Novotny, R. X. Bian,† and X. S. Xie*

Supported by Laboratory Directed Research and Development (LDRD).

*Postdoctoral Research Associate.
†Earth Systems Sciences Department, Atmospheric Sciences Section.

Optical trapping by highly focused laser beams has been extensively used for the manipulation of submicron-size particles such as biological structures.[1] Conventional optical tweezers rely on the field gradients near the focus of a laser beam, which give rise to a trapping force toward the focus. The trapping volume of these tweezers is diffraction limited. Near-field optical microscopy enables optical measurements at a dimension beyond the diffraction limit. With near-field microscopy, it is now possible to optically monitor chemical changes of single biomolecules. We have started an effort to extend the near-field approach to high-resolution optical tweezers,[2] with the aim of manipulation and control of biomolecules in an aqueous environment at the nanometer scale.

Our nanometric optical tweezers rely on the strongly enhanced electric field at a sharply pointed metallic tip under laser illumination. The near-field close to the tip consists mainly of evanescent components that decay rapidly with distance from the tip. The utilization of the metal tip for optical trapping offers the following advantages: (1) the highly confined evanescent fields significantly reduce the trapping volume, (2) the large field gradients result in a larger trapping force, and (3) the field enhancement allows the reduction of illumination power and radiation damages to the sample.

We have performed a rigorous electromagnetic analysis for the field enhancement. To solve Maxwell's equations in the specific geometry of the tip and its environment, we employed the multiple multipole method (MMP).[2] Figure 5.14 shows our three-dimensional MMP simulation of the foremost part of a gold tip (5-nm radius at the end) in water, for two different monochromatic plane-wave excitations. The wavelength of the illuminating light is 810 nm (Ti:sapphire laser). In Fig. 5.14(a), a plane wave is incident from the bottom with the polarization perpendicular to the tip axis, whereas in Fig. 5.14(b) the tip is illuminated from the side with the polarization parallel to the tip axis. A striking difference is seen for the two different polarizations: in (b), the intensity enhancement at the foremost part of the tip is 3000 times stronger than the illuminating intensity, whereas no enhancement beneath the tip, and only moderate enhancement on the sides of the tip (factor of five), exist in (a). This result suggests that it is crucial to have a large component of the excitation field along the axial direction to obtain a high field enhancement.

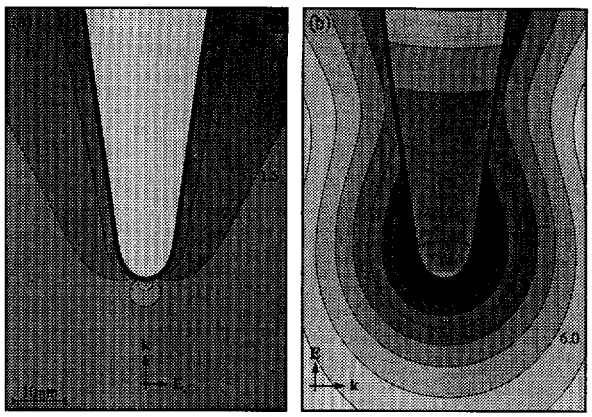

Figure 5.14. Near field of a gold tip in water, illuminated by two different monochromatic waves of 810 nm. Direction and polarization of the incident wave is indicated by the k and E vectors. The figures show contours of E^2 (factor of two between successive lines). The scaling is given by the numbers in the figures (multiples of the exciting field). No enhancement at the tip in (a); enhancement of 3000 in (b). The field in (b) is almost rotationally symmetric in the vicinity of the tip.

Figure 5.15 shows the field distribution around the tip and a dielectric sphere being trapped (dielectric constant $\varepsilon = 2.5$, radius 5 nm). The intensity contours are distorted around the sphere, and the field inside the sphere is highly inhomogeneous. The force (indicated by the arrow) cannot be calculated by using the Rayleigh approximation, which applies only to negligibly small particles. We performed a rigorous calculation of trapping force at different center positions of the particle using the Maxwell stress tensor.[2] The trapping potential was determined from the force field and is shown in Figure 5.16(a). Figures 5.16(b) and (c) show cross sections of the trapping potential along the transverse and axial directions of the tip. Because the trapping potential is almost rotationally symmetric, we show only results for

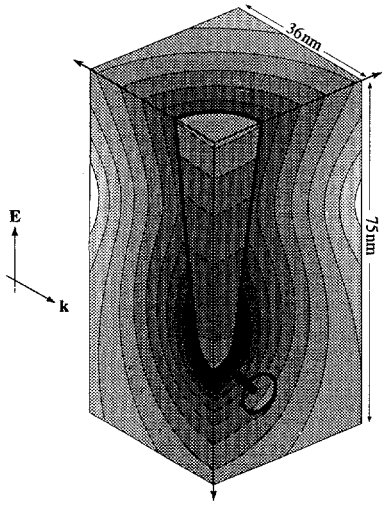

Figure 5.15. Perturbation of the near field by a particle being trapped (ε = 2.5, 5-nm radius). The arrow indicates the direction of the trapping force. The figure shows contours of E^2 (factor of two between successive lines).

the (x,z) plane. The potential is normalized with the illuminating intensity I_0 and with T = 300 K. Based on the theory of Brownian motion in a potential well, I_0 = 65 mW/μm² is required to have a trapping accuracy of 5 nm ($\langle x^2\rangle^{1/2}$ or $\langle y^2\rangle^{1/2}$). This result indicates the feasibility for trapping on a nanometer scale with a moderate power level.

A practical concern is laser heating of the tip, which could damage the sample and induce convection at the tip surface. A finite-difference time-domain method was employed to simulate the steady-state temperature distribution around the tip. For 65 mW/μm² of illuminating intensity, the maximum temperature rise at the surface of the tip was 6.5 K.[2] This result indicated that the temperature rise induced by laser heating is minimal for the intensity level required for stable trapping.

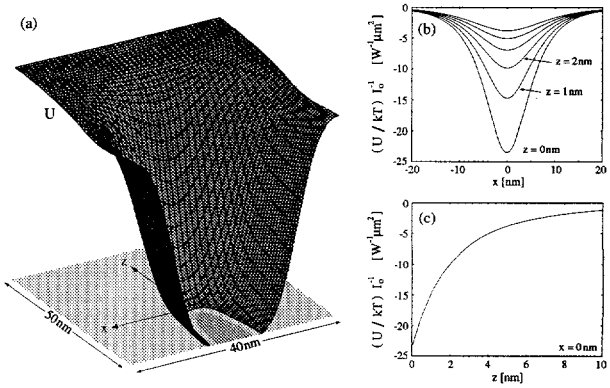

Figure 5.16. Trapping potential of a particle (ε = 2.5, 5-nm radius) in the vicinity of the tip. (a) Potential surface in the (x,z) plane (the tip is indicated by the shadow on the bottom plane). (b,c) Potential energy evaluated along the x and z directions (normalized with kT, T = 300 K, and with the illuminating intensity I_0).

In our optical trapping scheme, a sharp metal tip is brought to the focus of an illuminating beam where a particle has been trapped by the conventional means. A polarization component along the tip axis enables the trapping of the particle to the near-field zone of the tip. A trapped particle can be moved within the focal region of the illuminating light by translating the tip with a piezoceramic manipulator. The metal tip needs to be inert and nonreactive to the trapped particle. The trapped particle can be released by turning off the laser illumination. Experimental realization of this scheme is underway. The scheme has the potential for nanometric manipulation of individual biomolecules in their aqueous environment and control of their chemical activities.

References

1. A. Ashkin and J. M. Dziedzic, *Science* **235**, 1517 (1987).
2. L. Novotny, R. X. Bian, and X. S. Xie, *Phys. Rev. Lett.*, submitted.

6. Appendix

Chemical Structure and Dynamics Staff

Associate Director, EMSL

Steven D. Colson

B.S. Utah State University 1963; Ph.D. California Institute of Technology 1968; Postdoctoral Fellow, National Research Council (Ottawa) 1968; Assistant Professor to Professor of Chemistry, Yale University, 1968–1989; joined PNNL as Associate Director for Chemical Structure and Dynamics June 1989. Research interests: photochemistry, photophysics, and molecular dynamics; electronic structures of molecules; processes at the molecule/surface interface.

(509) 375-6882 sd_colson@pnl.gov

Program Manager

Robin S. (Rod) McDowell

B.A. Haverford College 1956; Ph.D. M.I.T. 1960; Staff Member, Assistant Group Leader, and Laboratory Fellow, Los Alamos National Laboratory, 1960–1991; joined PNNL as Program Manager for Chemical Structure and Dynamics April 1991. Research interests: high-resolution infrared and Raman spectroscopy applied to molecular structure and bonding; molecular dynamics and force fields; statistical mechanics; infrared analytical techniques.

(509) 375-6681 rs_mcdowell@pnl.gov

Staff

Stephan E. Barlow

B.A. Southern Oregon State College 1976; Ph.D. University of Colorado 1984, Postdoctoral Fellow 1984–1989; Senior Instructor in Chemistry, University of Denver 1989–1991; joined PNNL June 1991. Research interests: development and application of mass spectrometric techniques to gas-phase chemical kinetics, reaction mechanisms, and structure.

(509) 375-2959 se_barlow@pnl.gov

James P. Cowin

B.S. Case Western Reserve University 1974; Ph.D. University of Chicago 1981; Postdoctoral Fellow, University of Toronto 1981–1983; Assistant Professor of Chemistry, University of California, Santa Barbara, 1983–1990; joined PNNL July 1990. Research interests: molecular motions at interfaces, especially energy and charge transfer, bond formation dynamics, and light-stimulated surface reactions.

(509) 375-6838 jp_cowin@pnl.gov

Wayne P. Hess

B.A. University of Colorado 1981; M.S. University of Oregon 1983; Ph.D. University of Colorado 1988; Postdoctoral Fellow, Sandia Livermore Combustion Research Facility 1988–1990; joined PNNL January 1990. Research interests: modeling condensed phase chemistry through the study of energetic reactive processes in molecular solids and thin films (dissociation and fragmentation, electronic and vibrational energy transfer), using laser-induced desorption and ablation of adsorbed molecules and solid surfaces.

(509) 375-2555 wp_hess@pnl.gov

Gary R. Holtom

B.A. Pfeiffer College 1969; Ph.D. University of California, Berkeley, 1978; Postdoctoral Fellow, Wesleyan University 1978–1979; Head of Laser Operations, University of Pennsylvania Regional Laser and Biotechnology Laboratory, 1979–1989; joined PNNL September 1989. Research interests: short-pulse laser spectroscopy; condensed-phase photochemistry, in particular the dynamics of electronically excited organic molecules.

(509) 375-2459 gr_holtom@pnl.gov

Stephen A. Joyce

B.S. Boston College 1982; Ph.D. M.I.T. 1987; Postdoctoral Fellow, National Institute of Standards and Technology 1987–1989; Sandia National Laboratories 1989–1991; joined PNNL October 1991. Research interests: scanning probe microscopies for studying molecularly resolved chemistry on solid surfaces.

(509) 375-6459 sa_joyce@pnl.gov

Bruce D. Kay

B.S. University of Illinois 1976; Ph.D. University of Colorado 1982; Senior Member of the Technical Staff, Sandia National Laboratories, 1982–1991; joined PNNL November 1991. Research interests: chemical dynamics and kinetics of molecular processes occurring at the gas-surface interface; dissociative chemisorption of halogenated hydrocarbons on model oxide surfaces; quantum-resolved H-atom reactive scattering from halogenated surfaces;

trapping and "solvation" of ions and molecules on multilayer ice surfaces.
(509) 375-6484 bd_kay@pnl.gov

Thomas M. Orlando
B.S. Southampton College 1982; Ph.D. State University of New York at Stony Brook 1988; Postdoctoral Fellow, Universität Basel 1988–1989, Sandia National Laboratory 1990–1991; joined PNNL September 1991. Research interests: nonthermal interfacial reaction dynamics; electron- and photon-induced surface chemistry; liquid interfaces; low-temperature plasmas; dissociative electron attachment; laser spectroscopy.
(509) 375-6404 tm_orlando@pnl.gov

Douglas Ray
B.A. Kalamazoo College 1979; Ph.D. University of California, Berkeley, 1985; Postdoctoral Fellow, Joint Institute for Laboratory Astrophysics 1985–1990; joined PNNL June 1990. Research interests: the experimental study of dynamical processes in clusters and at liquid interfaces using techniques of laser spectroscopy and mass spectrometry.
(509) 375-2104 d_ray@pnl.gov

Steven W. Sharpe
B.S. University of Bridgeport 1979; Ph.D. State University of New York at Stony Brook 1986; Postdoctoral Fellow, University of Southern California 1987–1990; joined PNNL May 1990. Research interests: high-resolution molecular spectroscopy.
(509) 375-5942 sw_sharpe@pnl.gov

Lai-Sheng Wang
B.S. Wuhan University 1982; Ph.D. University of California, Berkeley, 1989; Postdoctoral Fellow, Rice University 1990–1992; joint Washington State University/PNNL appointment January 1993. Research interests: clusters of metals, semiconductors, and insulators important as model systems for catalysis, interfaces, and surface chemistry; photoelectron spectroscopy and pulsed laser-vaporization techniques; novel gas-phase molecules involving metal atoms with oxygen, carbon, and nitrogen and the nature of M–O, M–C, and M–N chemical bonding; electrospray and solvation of singly and multiply charged anions.
(509) 375-5976 ls_wang@pnl.gov

Xiaoliang (Sunney) Xie
B.S. Peking University 1984; Ph.D. University of California at San Diego 1990; Postdoctoral Fellow, University of Chicago 1990–1991; joined PNNL January 1992. Research interests: single-molecule and ultrafast spectroscopy, near-field microscopy, chemical physics in biological systems.
(509) 375-6372 xs_xie@pnl.gov

Research Scientists

Kenneth M. Beck
B.A. Northwestern University 1972; M.S. University of Chicago 1985, Ph.D. 1988; Postdoctoral Fellow University of Pennsylvania 1988–1990, PNNL 1990–1991; University of Central Florida 1991–1995; PNNL 1996; joined PNNL staff September 1996.
(509) 375-4533 km_beck@pnl.gov

Thomas A. Blake
B.S. University of Bridgeport 1981; Ph.D. Wesleyan University 1989; Postdoctoral Fellow, University of Washington 1988–1991; NRC Research Associate, NASA Ames Research Center 1991–1994; joined PNNL September 1994.
(509) 375-4341 ta_blake@pnl.gov

Martin J. Iedema
B.S. University of Southern California 1988; Technician, Mt. Wilson Observatory 1987–1990; joined PNNL September 1990.
(509) 375-2354 mj_iedema@pnl.gov

Alan G. Joly
B.S. University of Rochester 1985; Ph.D. M.I.T. 1990; Postdoctoral Fellow, PNNL 1990–1993; joined PNNL staff June 1993.
(509) 375-2729 ag_joly@pnl.gov

Gregory A. Kimmel
B.S. Cornell University 1984, Ph.D. 1992; Postdoctoral Fellow PNNL, 1992–1995; joined PNNL staff September 1995.
(509) 375-6611 ga_kimmel@pnl.gov

Hong (Peter) Lu
B.A. Beijing University 1982, M.Sc. 1984; M. Phil. Columbia 1987, Ph.D. 1991; Postdoctoral Fellow, Northwestern 1991–1995; Postdoctoral Fellow, PNNL 1995–1996; joined PNNL staff November 1996.
(509) 375-2743 h_lu@pnl.gov

R. Scott Smith
B.S. Northern Arizona University 1983; Ph.D. University of Utah 1988; Postdoctoral Fellow, University of Arizona 1988–1989, PNNL 1990–1992; joined PNNL staff October 1992.
(509) 375-2697 rs_smith@pnl.gov

Russell G. Tonkyn
B.A. Reed College 1978; Ph.D. University of Wisconsin 1988; Postdoctoral Fellow, Brookhaven National Laboratory 1988–1991, PNNL 1991–1992; joined PNNL staff November 1992.
(509) 375-6481 rg_tonkyn@pnl.gov

Visiting Scientists

Carey K. Johnson
B.S., B.A. Tabor College 1973; Ph.D. Iowa State University 1981; Postdoctoral Fellow, University of Pennsylvania 1982–1984; Associate Professor of Chemistry, University of Kansas; AWU Visiting Scientist Fellowship at PNNL with Sunney Xie, June–July 1996.

Nicolai G. Petrick
M.S. Technical University of Leningrad 1977, Ph.D. 1980; D.Sc. Research Institute of Complex Power Technology (VNIPIET), Leningrad, 1984; Senior Scientist with VNIPIET, St. Petersburg; SABIT (Special American Business Internship Training Program) appointment at PNNL with Thom Orlando, April–Sept. 1996.
(509) 375-6887

Bobbi J. Roop
B.S. Tulane University 1979; Ph.D. M.I.T. 1985; Postdoctoral Fellow, University of Texas at Austin 1985–1988; Chemist, National Institute of Standards and Technology 1988–1989; Research Chemist/Consultant Argonne National Laboratory 1989–1991; Roop Scientific Research 1992–1994; AWU Visiting Scientist Fellowship at PNNL with Jim Cowin from April 1996.
(509) 375-5903

Robert L. Sams
B.A. Western Washington University 1962; M.S. University of Washington 1967; National Bureau of Standards/National Institute of Standards and Technology 1967–1995; AWU Visiting Scientist Fellowship at PNNL with Steve Sharpe from December 1995.
(509) 375-6456 rl_sams@pnl.gov

Athanassios A. Tsekouras
B.S. National University of Athens 1987; Ph.D. Stanford University 1992; Postdoctoral Fellow M.I.T. 1992–1996; AWU Visiting Scientist at PNNL with Jim Cowin from July 1996.
(509) 372-4537

Operations Administrator

Denise A. Motsenbocker
B.A. University of Washington 1975.

Office Support

Debra M. Hinton
Cynthia A. Irwin

Postdoctoral Fellows

Albert H. Bahnmaier
Ph.D. University of Ulm 1993; Postdoctoral Fellow, CS&D, with Doug Ray, 1993–1996.

James Chesko
B.Sc. University of British Columbia 1987; Ph.D. University of California, Berkeley, 1995, Postdoctral Fellow 1995–1996; Postdoctoral Fellow, CS&D, with Sunney Xie, 1996– .

Chuan-Fan Ding
B.S. University of Science and Technology of China 1984; Ph.D. Fudan University, Shanghai; Research Fellow, Institute of Chemistry, Chinese Academy of Sciences 1991–1995; Postdoctoral Fellow with Lai-Sheng Wang, 1996– .

Robert Doolen
B.S. University of New Mexico 1989; Ph.D. University of California, San Diego, 1994; Postdoctoral Fellow, CS&D, with Doug Ray, 1994–1996; now Postdoctoral Fellow at Colorado State University, Fort Collins.

David S. Karpovich
B.S. Saginaw Valley (Mich.) State University 1992; Ph.D. Michigan State University 1996; Postdoctoral Fellow, CS&D, with Doug Ray, 1996– .

Karen Knutsen
B.A. Linfield College 1981; Ph.D. University of Colorado 1992; Postdoctoral Fellow, CS&D, with Thom Orlando, 1994– .

San (Sam) Li
B.S. Nankai University, Tianjin, 1983; Ph.D. Memphis State University 1991; Postdoctoral Fellow, University of Florida, 1991–1996; Postdoctoral Fellow with Lai-Sheng Wang, 1996– .

Lukas Novotny
Dipl.El.-Eng. Swiss Federal Institute of Technology (ETH) 1992, Dr.Sc.Nat. 1996; Postdoctoral Fellow, CS&D, with Sunney Xie, 1996– .

James Bradley Rowland
B.S. Southeastern Oklahoma State University 1990; Ph.D. Oklahoma State University 1995; Postdoctoral Fellow, CS&D, with Wayne Hess, 1996– .

Matthew T. Sieger
B.S. University of Missouri at Rolla 1990; M.S. University of Illinois 1991, Ph.D. 1995; Postdoctoral Fellow, CS&D, with Thom Orlando, 1996–.

William C. Simpson
B.S. Willamette University 1990; Ohio State University 1990–1991; M.S. University of California, Riverside, 1992, Ph.D. 1995; Postdoctoral Fellow, CS&D, with Thom Orlando, 1996– .

Michael J. Stirniman
B.S. University of Illinois 1988; Ph.D. University of Chicago 1995; Postdoctoral Fellow, CS&D, with Bruce Kay, 1995–1996; now Staff Development Engineer with Seagate Recording Media Group, Fremont, Cal.

David P. Taylor
B.A. Concordia College 1979; Analytical Chemist, Wyeth Laboratories 1980–1982; Merck and Co. 1982–1985; Smith Kline and French Laboratories 1985–1987; M.S. Drexel University 1987; Ph.D. SUNY Stony Brook 1993; Postdoctoral Fellow, Colorado State University 1993–1996; Postdoctoral Fellow, CS&D, with Thom Orlando, 1996– .

Mark D. Tinkle
B.S. California Institute of Technology 1984; M.S. California State University, Fullerton 1987; M.S. University of California, San Diego 1989, Ph.D. 1994; Postdoctoral Fellow, CS&D, with Steve Barlow, 1996– .

Vincent A. Venturo
B.S. Rutgers University 1985; M.S. University of California, Berkeley, 1988; Ph.D. University of California at Los Angeles 1993; Postdoctoral Fellow, CS&D, with Doug Ray, 1994–1996; now Postdoctoral Fellow at Colorado State University, Fort Collins.

Graduate Students

Margaret S. Fyfield
Portland State University, working with Jim Cowin.

Jennifer M. Gaudioso
B.A. Bard College 1995; Science and Engineering Research Semester (SERS) student with Doug Ray 1995–1996.

Erik D. Sanchez
Portland State University, working with Sunney Xie.

Richard Webb
Washington State University, working with Wayne Hess.

Paul R. Winter
University of Colorado, working with Wayne Hess.

Hongbin Wu
Washington State University, working with Lai-Sheng Wang.

Undergraduate Student

Li Li
Washington State University, working with Lai-Sheng Wang.

Technical Assistant

Xi Li
B.S. Northwest University, Lanzhou, China, 1986; M.S. Institute of Applied Physics, Chengdu University of Science and Technology, 1991; Researcher and Lecturer, Gansu United University, Lanzhou, 1992–1995; working with Lai-Sheng Wang, 1996– .

Publications and Presentations

Publications

K. M. Beck, K. A. H. German, and W. P. Hess, "Thermal State Distributions Deduced from (2+1) Resonance Enhanced Multiphoton Ionization of CO," *Chem. Phys. Lett.* **256**, 298–304 (1996).

T. A. Blake, C. Chackerian, Jr., and J. R. Podolske, "Prognosis for a Mid-Infrared Magnetic Rotation Spectrometer for the *in situ* Detection of Atmospheric Free Radicals," *Appl. Opt.* **35**, 973–985 (1996).

T. A. Blake, S. Xu, and S. W. Sharpe, "High-Resolution Infrared Spectroscopy of the ν_4 Fundamental Band of Chlorine Nitrate," *J. Mol. Spectrosc.* **175**, 303–314 (1996).

D. E. Brown, S. M. George, C. Huang, E. K. L. Wong, K. B. Rider, R. S. Smith, and B. D. Kay, "H_2O Condensation Coefficient and Refractive Index for Vapor-Deposited Ice From Molecular Beam and Optical Interference Measurements," *J. Phys. Chem.* **100**, 4988–4993 (1996).

H. S. Cheng and L. S. Wang, "Dimer Growth, Structure Transition and Antiferromagnetic Ordering in Small Chromium Clusters," *Phys. Rev. Lett.* **77**, 51–54 (1996).

S. R. Desai, H. Wu, C. M. Rohlfing, and L.-S. Wang, "A Study of the Structure and Bonding of Small Aluminum Oxide Clusters by Photoelectron Spectroscopy: $Al_xO_y^-$ (x = 1–2, y = 1–5)," *J. Chem. Phys.* **106**, 1309–1317 (1997).

G. S. Herman, M. C. Gallagher, S. A. Joyce, and C. H. F. Peden, "Structure of Epitaxial Thin TiO_x Films on W(110) as Studied by Low Energy Electron Diffraction and Scanning Tunneling Microscopy," *J. Vac. Sci. Technol. B* **14**, 1126–1130 (1996).

W. P. Hess, K. A. H. German, R. A. Bradley, and M. I. McCarthy, "Laser Ablation of Sodium Nitrate: NO Desorption Following Excitation of the π–π^* Band of the Nitrate Anion," *Appl. Surf. Sci.* **96–98**, 321–325 (1996).

M. C. Hsiao, B. T. Merritt, B. M. Penetrante, G. E. Vogtlin, P. H. Wallman, R. G. Tonkyn, R. Shah, and T. M. Orlando, "Plasma Assisted Oxidation of Propene," *J. Adv. Oxid. Technol.* **1**, 79–84 (1996).

J. Kelly, B. Cannon, and S. Sharpe, "FM Laser Techniques and Technology Developments," *CALIOPE Program Third Interim Technical Review* [Livermore, Cal., 13–15 Feb. 1996], *Proceedings* (U.S. Dept. of Energy, Office of Nonproliferation and National Security, Office of Research and Development, 1996) **1**, 199–208.

G. A. Kimmel and T. M. Orlando, "Observation of Negative Ion Resonances in Amorphous Ice via Low-Energy (5–40 eV) Electron-Stimulated Production of Molecular Hydrogen," *Phys. Rev. Lett.* **77**, 3983–3986 (1996).

K. Knutsen and T. M. Orlando, "Low-Energy (5–80 eV) Electron-Stimulated Desorption of H^+ (D^+), OH^+ (OD^+), O^+, and NO^+ from Solution-Grown $NaNO_3$ Crystals," *Surf. Sci.* **348**, 143–152 (1996).

K. Knutsen, Y. Su, K. D. Keefer, and T. M. Orlando, "Mechanisms of Radiolytic Decomposition of Complex Nuclear Waste Forms," *Proc. Amer. Nucl. Soc.: Progress in Hazardous Waste Cleanup* **1**, 616 (1996).

H. P. Lu and X. S. Xie, "Single-Molecule Spectral Fluctuations at Room Temperature," *Nature* **385**, 143–146 (1997).

H. B. Lueck, T. C. Swinney, B. S. Hudson, and D. M. Friedrich, "Resonance Raman Studies of Benzene Derivatives with Strong Conjugation: Nitrile Substitution," *Chem. Phys. Lett.* **258**, 80–86 (1996).

B. L. Maschhoff, M. J. Iedema, M. Kwini, and J. P. Cowin, "Long-Range Electrostatic Forces in the Coadsorption of CH_3Cl and Water," *Surf. Sci.* **359**, 253–268 (1996).

M. I. McCarthy, K. A Peterson, and W. P. Hess, "Electronic Structure of Sodium Nitrate: Investigations of Laser Desorption Mechanisms," *J. Phys. Chem.* **100**, 6708–6714 (1996).

R. S. McDowell, S. W. Sharpe, and J. F. Kelly, "Overview of CALIOPE Research at Pacific Northwest National Laboratory," *CALIOPE Program Third Interim Technical Review* [Livermore, Cal., 13–15 Feb. 1996], *Proceedings* (U.S. Dept. of Energy, Office of Nonproliferation and National Security, Office of Research and Development, 1996) **1**, 19-22 (1996).

M. B. More, E. D. Glendening, D. Ray, D. Feller, and P. B. Armentrout, "Cation–Ether Complexes in the Gas Phase: Bond Dissociation Energies and Equilibrium Structures of $Li^+(O(CH_3)_2)_x$ (x = 1–4)," *J. Phys. Chem.* **100**, 1605–1614 (1996).

M. B. More, D. Ray, and P. B. Armentrout, "Cation–Ether Complexes in the Gas Phase: Bond Dissociation Energies of Na^+(dimethyl ether)$_x$ (x = 1–4), Na^+(dimethoxyethane)$_x$ (x = 1 and 2) and Na^+(12-crown-4)," *J. Phys. Chem. A* **101**, 831–839 (1997).

L. Novotny, "Single Molecule Fluorescence in Inhomogeneous Environments," *Appl. Phys. Lett.* **69**, 3806–3808 (1996).

A. J. Peurrung and S. E. Barlow, "Characteristics of a Weakly Ionized Nonneutral Plasma," *Phys. Plasmas* **3**, 2859–2863 (1996).

A. J. Peurrung, R. T. Kouzes, and S. E. Barlow, "The Non-Neutral Plasma: an Introduction to Physics with Relevance to Cyclotron Resonance Mass Spectrometry," *Int. J. Mass Spectrom. Ion Processes* **157/158**, 39–83 (1996).

J. M. Price, M. V. Gorshkov, S. E. Barlow, and D. Ray, "Frequency Sweep Ion Trap Mass Spectrometry," *Proceedings, 44th ASMS Conference on Mass Spectrometry and Allied Topics* (Portland, Ore., May 12–16, 1996), p. 122 (1996).

D. Ray, D. Feller, M. B. More, E. D. Glendening, and P. B. Armentrout, "Cation–Ether Complexes in the Gas Phase: Bond Dissociation Energies and Equilibrium Structures of Li^+[1,2-dimethoxyethane]$_x$, x = 1 and 2, and Li^+[12-crown-4]," *J. Phys. Chem.* **100**, 16116–16125 (1996).

J. B. Rowland and W. P. Hess, "The Ultraviolet Photochemistry of Condensed-Phase Acetyl Chloride," *Chem. Phys. Lett.* **263**, 574–580 (1996).

S. W. Sharpe, J. F. Kelly, and R. S. McDowell, "Continuing Spectroscopic Efforts at PNNL," *CALIOPE Program Third Interim Technical Review* [Livermore, Cal., 13–15 Feb. 1996], *Proceedings* (U.S. Dept. of Energy, Office of Nonproliferation and National Security, Office of Research and Development, 1996), **2**, 59–67 (classified SECRET/NSI/NOFORN).

S. W. Sharpe, S. Xu, R. S. McDowell, and T. A. Blake, "Tunable Diode Lasers and Their Application in Cold Molecular Beam Spectroscopy," *Proc. SPIE* **2834**, 91–101 (1996) (*Application of Tunable Diode and Other Infrared Sources for Atmospheric Studies and Industrial Process Monitoring*, A. Fried, ed.).

R. S. Smith, C. Huang, E. K. L. Wong, and B. D. Kay, "Desorption and Crystallization Kinetics in Nanoscale Thin Films of Amorphous Water Ice," *Surf. Sci. Lett*, **367**, L13–L18 (1996).

R. J. Speedy, P. G. Debenedetti, R. S. Smith, C. Huang, and B. D. Kay, "The Evaporation Rate, Free Energy, and Entropy of Amorphous Water at 150 K," *J. Chem. Phys.* **105**, 240–244 (1996).

M. J. Stirniman, C. Huang, R. S. Smith, S. A. Joyce, and B. D. Kay, "The Adsorption and Desorption of Water on Single Crystal MgO(100): The Role of Surface Defects," *J. Chem. Phys.* **105**, 1295–1298 (1996).

K. D. Thrall, J. J. Toth, and S. W. Sharpe, "Analysis of Exhaled Breath by Laser Detection," *Proc. SPIE* **2676**, 136–146 (1996) (*Biomedical Sensing, Imaging, and Tracking Technologies I*).

R. G. Tonkyn, S. E. Barlow, and T. M. Orlando, "Destruction of Carbon Tetrachloride in a Dielectric Barrier/Packed-Bed Corona Reactor," *J. Appl. Phys.* **80**, 4877–4886 (1996).

L.-S. Wang, "Study of Iron–Carbon Mixed Clusters, FeC_n (n = 2–5): A Possible Linear to Cyclic Transition from FeC_3 to FeC_4," *Surf. Rev. Lett.* **3**, 423–427 (1996).

L.-S. Wang, J. Fan, and L. Lou, "Iron Clusters and Oxygen-Chemisorbed Iron Clusters," *Surf. Rev. Lett.* **3**, 695–699 (1996).

L.-S. Wang, S. Li, and H. Wu, "Photoelectron Spectroscopy and Electronic Structure of Met-Car Ti_8C_{12}," *J. Phys. Chem.* **100**, 19211–19214 (1996).

L.-S. Wang and H. Wu, "A Comparative Study of the Electronic Structure of the First Row Transition Metal Clusters," *Proc. Int. Symp. on the Science and Technology of Atomically Engineered Materials* (Oct. 30 – Nov. 4, 1995, Richmond, Va.), ed. by P. Jena, S. N. Khanna, and B. K. Rao (World Scientific, New Jersey, 1996), pp. 245–250.

L.-S. Wang, H. Wu, and S. R. Desai, "Sequential Oxygen Atom Chemisorption on Surfaces of Small Iron Clusters," *Phys. Rev. Lett.* **76**, 4853–4856 (1996).

L.-S. Wang, H. Wu, S. R. Desai, J. Fan, and S. D. Colson, "A Photoelectron Spectroscopic Study of Small Silicon Oxide Clusters: SiO_2, Si_2O_3, and Si_2O_4," *J. Phys. Chem.* **100**, 8697–8700 (1996).

L.-S. Wang, H. Wu, S. R. Desai, and L. Lou, "Electronic Structure of Small Copper Oxide Clusters: From Cu_2O to Cu_2O_4," *Phys. Rev. B* **53**, 8028–8031 (1996).

H. Wu, S. R. Desai, and L.-S. Wang, "Electronic Structure of Small Titanium Clusters: Emergence and Evolution of the 3*d* Band," *Phys. Rev. Lett.* **76**, 212–215 (1996).

H. Wu, S. R. Desai, and L.-S. Wang, "Evolution of the Electronic Structure of Small Vanadium Clusters From Molecular to Bulk-Like," *Phys. Rev. Lett.* **77**, 2436–2439 (1996).

H. Wu, S. R. Desai, and L.-S. Wang, "Observation and Photoelectron Spectroscopic Study of Novel Mono- and Di-Iron Oxide Molecules: FeO_y^- (y = 1–4) and $Fe_2O_y^-$ (y = 1–5)," *J. Am. Chem. Soc.* **118**, 5296–5301 (1996).

H. Wu, S. R. Desai, and L.-S. Wang, "Chemical Bonding Between Cu and Oxygen–Copper Oxides vs. O_2 Complexes: A Study of CuO_x (x = 0–6) Species by Anion Photoelectron Spectroscopy," *J. Phys. Chem.* **101**, xxx–xxx (1997).

X. S. Xie, "Single-Molecule Spectroscopy and Dynamics at Room Temperature," *Acc. Chem. Res.* **29**, 598–606 (1996).

X.-L. Zhou and J. P. Cowin, "Photodestruction of CCl_4 on MgO Films with/without Water," *J. Phys. Chem.* **100**, 1055–1065 (1996).

In Press and Submitted

A. H. Bahnmaier, A. G. Joly, J. M. Price, and D. Ray, "Rotational Coherence Spectroscopy of Mass-Selected Fluorene–Ar Heterodimers by Time-Resolved Ionization Depletion," *Chem. Phys. Lett.*, submitted.

K. M. Beck, M. I. McCarthy, and W. P. Hess, "Atomic and Molecular Photostimulated Desorption from Complex Ionic Crystals," *J. Electronic Materials*, submitted.

K. M. Beck, D. P. Taylor, and W. P. Hess, "Photostimulated Desorption of CO from Geologic Calcite Following 193-nm Irradiation," *Phys. Rev. B*, in press.

J. Biesecker, H. Wang, M. J. Iedema, B. G. Ellison, and J. P. Cowin, "Very Low-Energy (1–5 eV) Ion Source for Molecular Ion Deposition at Surfaces," *Rev. Sci. Instr.*, submitted.

R. G. Clemmer, J. F. Kelly, S. W. Martin, G. M. Mong, and S. W. Sharpe, "Laser-Based Detection of Chemical Contraband," *Proc. SPIE* **2937** (*Facilitating Technologies for Law Enforcement*), in press.

S. R. Desai, H. Wu, and L.-S. Wang, "Vibrationally Resolved Photoelectron Spectroscopy of AlO^- and AlO_2^-," *Int. J. Mass Spectrom. Ion Processes*, in press.

S. C. Goheen, K. L. Wahl, W. P. Hess, and J. A. Campbell, "Mass Spectrometry of Low Molecular Weight Solids by Matrix Assisted Laser Desorption Ionization," *J. Mass. Spectrom.*, submitted.

M. V. Gorshkov, J. A. Mack, S. E. Barlow, D. Ray, and J. M. Price, "Frequency-Sweep Radiofrequency Ion Trap Mass Spectrometry," *J. Amer. Soc. Mass. Spectrom.*, submitted.

G. A. Kimmel, P. Clouthier, L. Sanche, and T. M. Orlando, "Low-Energy (5–50 eV) Electron-Stimulated Desorption of Atomic Hydrogen and Metastable Emission from Amorphous Ice," *J. Phys. Chem.*, submitted.

N. Kizhakevariam, M. J. Iedema, and J. P. Cowin, "Mixed Alkaline Earth Metal Oxides Surfaces: Ultrathin Films of $Ca_xMg_{1-x}O$ (001)," *J. Phys. Chem.*, submitted.

K. Knutsen and T. M. Orlando, "Photon-Stimulated Desorption of $O(^3P_J)$ and $NO(^2\Pi)$ from $NaNO_3$ Single Crystals," *Phys. Rev. B*, in press.

O. Kornienko, S. Brynjelsen, L. Hanley, and T. M. Orlando, "Analysis of Ethylenediaminetetraacetic acid (EDTA) by Laser Desorption Ion Trap Mass Spectrometry," *Proc. 42nd ASMS Conf. Mass Spectrom. Allied Topics*, in press.

S. Li and L.-S. Wang, "Probing the Electronic Structure of Metallocarbohedrenes: M_8C_{12} (M = Ti, V, Cr, Zr, Nb)," *Phys. Rev. Lett.*, submitted.

H. P. Lu and X. S. Xie, "Single-Molecule Kinetics of Interfacial Electron Transfer," *J. Phys. Chem.*, in press.

R. S. McDowell, "Infrared Spectroscopy" and (in part) "Molecular Structure and Spectra," *McGraw-Hill Encyclopedia of Science & Technology*, 8th ed. (McGraw Hill Book Co., 1997), in press.

R. McDowell, "Spectroscopy and Detection Techniques for Remote Sensing by Laser," *Arms Control and Nonproliferation Technologies*, in press.

R. S. McDowell and J. F. Kelly, "Spectroscopy, Optical," *Kirk-Othmer Encyclopedia of Chemical Technology*, 4th ed. (John Wiley & Sons, New York, 1997), in press.

L. Novotny, R. X. Bian, and X. S. Xie, "Nanometric Optical Tweezers," *Phys. Rev. Lett.*, submitted.

M. T. Sieger, W. C. Simpson, and T. M. Orlando, "The Electron-Stimulated Desorption of D^+ from D_2O Ice: Surface Structure and Electronic Excitations," *Phys. Rev. B*, submitted.

R. S. Smith, C. Huang, and B. D. Kay, "Evidence for Molecular Translational Diffusion During the Crystallization of Amorphous Solid Water," *J. Phys. Chem.*, submitted.

R. S. Smith, C. Huang, E. K. L. Wong, and B. D. Kay, "The Molecular Volcano: Abrupt CCl_4 Desorption Driven by the Crystallization of Amorphous Solid Water," *Phys. Rev. Lett.*, submitted.

S. C. Stone, L. A. Philips, G. T. Fraser, F. J. Lovas, L.-H. Xu, and S. W. Sharpe, "High-Resolution Microwave and Infrared Molecular Beam Studies of the Conformers of 1,1,2,2-Tetrafluoroethane," *J. Mol. Spectrosc.*, submitted.

R. Tonkyn, S. Barlow, M. L. Balmer, T. Orlando, J. Hoard, and D. Goullette, "Vehicle Exhaust Treatment Using Electrical Discharge Methods," SAE *Conference Proceedings*, in press.

S. H. Tseng, D. F. Eggers, T. A. Blake, R. D. Beck, R. O. Watts, F. J. Lovas, and N. Zobov, "Infrared and Microwave Spectra of the N_2–Propyne van der Waals Cluster," *J. Mol. Spectrosc.*, in press.

V. A. Venturo, A. G. Joly, and D. Ray, "Pulse Compression with a High-Energy Nd:YAG Regenerative Amplifier System," *Appl. Opt.*, submitted.

L.-S. Wang and H. Cheng, "On the Growth Pathways of Metallocarbohedrenes: Cage-Like or Cubic?" *Phys. Rev. Lett.*, submitted.

L.-S. Wang, S. R. Desai, H. Wu, and J. B. Nicholas, "Silicon Oxide Clusters: Chains and Rings," *Z. Phys. D: Atoms, Mols., Clusters*, in press.

L.-S. Wang and S. Li, "New Magic Numbers in $Ti_xC_y^-$ and $V_xC_y^-$ Anion Clusters: Implications for Met-Car Growth Pathways," *J. Amer. Chem. Soc.*, submitted.

L.-S. Wang, J. B. Nicholas, H. Wu, and S. D. Colson, "Si_3O_x (x = 1–6): Models for Oxidation of Silicon Surfaces and Defect Sites in Bulk Oxide Materials," *Phys. Rev. Lett.*, submitted.

L.-S. Wang and H. Wu, "Photoelectron Spectroscopy of Transition Metal Clusters," *Z. Phys. Chem.*, in press.

L.-S. Wang, H. Wu, and H. Cheng, "Photoelectron Spectroscopy of Small Chromium Clusters: Observation of Even–Odd Alternations and Theoretical Interpretation," *Phys. Rev. B*, submitted.

Z. Wang, D. M. Friedrich, and A. G. Joly, "Solvent Effects on the Fluorescence of Sodium Salicylate and its Derivatives," *J. Phys. Chem.*, submitted.

H. Wong, J. P. Biesecker, M. J. Iedema, G. B. Ellison, and J. P. Cowin, "Low-Energy Deposition and Collision-Induced Dissociation of Water Ion on Pt(111)," *Surf. Sci.*, in press.

H. Wu and L.-S. Wang, "A Study of Nickel Monooxide (NiO), Nickel Dioxide (ONiO), and Ni–O_2 Complex by Anion Photoelectron Spectroscopy," *J. Chem. Phys.*, submitted.

X. S. Xie, R. X. Bian, and R. C. Dunn, "Near-Field Microscopy and Spectroscopy of Single Molecules, Single Proteins, and Biological Membranes," in *Focus on Multidimensional Microscopy*, P. C. Cheng, P. P. Hwang, J. L. Wu, G. Wang, and H. Kim, eds. (World Scientific Publ. Co.), in press.

Patents

S. E. Barlow, M. L. Alexander, and J. C. Follansbee, "Asymmetric Ion Trap," patent pending.

S. E. Barlow, R. G. Tonkyn, and T. M Orlando, "Method and Apparatus for Processing Exhaust Gas with Corona Discharge," patent pending.

K. M. Beck, "Photoacoustic Touch-Off Probe," patent pending.

A. J. Peurrung and S. E. Barlow, "Confinement of Weakly Ionized Gas in the Presence of a Neutral Gas," patent pending.

Presentations *(Presenter underlined)*

A. H. Bahnmaier, A. G. Joly, J. M. Price, and D. Ray, "Ionization-Detected Rotational Coherence Spectroscopy of Mass-Selected Clusters," 211th American Chemical Society National Meeting, New Orleans, March 24–28, 1996.

K. M. Beck, "CO Desorption from Geologic Calcite Following 193-nm Excitation," Department of Physical Organic Chemistry, Utrecht University, Netherlands, May 15, 1996.

K. M. Beck, "CO Desorption from Geologic Calcite by Excitation of the CO_3^{2-} π–π^* Transition," Department of Chemistry, University of Nottingham, U.K., May 16, 1996.

R. X. Bian, P. Leung, and X. S. Xie, "Near-Field Single Molecule Spectroscopy at Room Temperature," SPIE International Symposium on Biomedical Optics, San Jose, Cal., Feb. 8–14, 1996.

R. X. Bian, L. Novotny, and X. S. Xie, "Finite Difference Time Domain Simulation of Near-Field Optical Phenomena," Optical Society of America Annual Meeting, Rochester, N.Y., Oct. 20–24, 1996.

T. A. Blake, "The Infrared Spectroscopy of Chlorine Nitrate and Hexafluoroethane: Examples of the Facilities and Capabilities of the Environmental Molecular Science Laboratory's High-Resolution Infrared Spectroscopy Laboratory," NASA/Ames Research Center, Moffett Field, Cal., Aug. 5, 1996.

T. A. Blake, S. W. Sharpe, S. C. Stone, and L. A. Philips, "High Resolution Infrared Spectroscopy of the ν_5 and ν_7 Bands of Hexafluoroethane," 51st Ohio State University International Symposium on Molecular Spectroscopy, Columbus, June 8–14, 1996.

T. J. Cleij, J. K. King, and K. M. Beck, "Spectroscopy of Perylene Clusters Involving Small Atmospheric Species," Gordon Research Conference on Molecular and Ionic Clusters, Tuscany, Italy, May 5–10, 1996.

R. G. Clemmer, J. F. Kelly, S. W. Martin, G. M. Mong, and S. W. Sharpe, "Laser-Based Detection of Chemical Contraband," SPIE Symposium on Facilitating Technologies for Law Enforcement, Boston, Nov. 18–22, 1996.

S. D. Colson, "Strategy for Characterization and Risk Evaluation of Military Waste," Gordon Research Conference on Nuclear Waste and Energy, Pruhonice near Prague, Czech Republic, Sept. 8–12, 1996.

J. P. Cowin, H. Wang, M. J. Iedema, J. Biesecker, and G. B. Ellison, "Aqueous-Like Studies via Low-Energy Ion Deposition on Surfaces," Gordon Research Conference on Interaction of Water with Surfaces, Plymouth, N.H., July 28 – Aug. 3, 1996.

J. P. Cowin, H. Wang, M. J. Iedema, and G. B. Ellison, "Low Energy Water Ion Deposition and Collision-Induced Dissociation on Pt(111)," American Chemical Society 212th National Meeting, Orlando, Fla., Aug. 25–29, 1996.

R. Doolen, J. M. Gaudioso, and D. Ray, "Transport of Molecules across the Liquid Water–Vapor Interface Probed by Surface Nonlinear Optical Spectroscopy," American Physical Society Annual Meeting, St. Louis, March 18–22, 1996.

D. M. Friedrich, Z. Wang, C. C. Ainsworth, P. L. Gassman, and A. G. Joly, "Speciation of Salicylate Surface Complexes in Aqueous Alumina Suspensions by Polarized Fluorescence Excitation Spectroscopy," Environmental Heterogeneous Interfaces Symposium, 211th American Chemical Society National Meeting, New Orleans, March 24–28, 1996.

M. C. Gallagher, M. S. Fyfield, J. P. Cowin, G. S. Herman, C. H. F. Peden, and S. A. Joyce, "Scanning Tunneling Microscopy Studies of Thin-Film Oxide Surfaces," 211th American Chemical Society National Meeting, New Orleans, March 24–28, 1996.

M. C. Gallagher, M. S. Fyfield, J. P. Cowin, G. S. Herman, C. H. F. Peden, and S. A. Joyce, "Scanning Tunneling Microscopy Studies of Thin-Film Oxide Surfaces," Workshop on X-Ray Techniques in the Environment, Richland, Wash., Sept. 8–12, 1996.

M. C. Gallagher, M. S. Fyfield, J. P. Cowin, G. S. Herman, C. H. F. Peden, and S. A. Joyce, "Scanning Tunneling Microscopy Studies of Thin-Film Oxide Surfaces," 23rd Annual Conference, Federation of Analytical Chemistry and Spectroscopy Societies (FACSS), Kansas City, Mo., Sept. 29 – Oct. 4, 1996.

M. C. Gallagher, M. S. Fyfield, J. P. Cowin, G. S. Herman, C. H. F. Peden, and S. A. Joyce, "Scanning Tunneling Microscopy Studies of Thin-Film Oxide Surfaces," American Vacuum Society

National Meeting, Philadelphia, Oct. 12–18, 1996.

M. C. Gallagher and S. A. Joyce, "A Model for Scanning Tunneling Microscopy of Ultrathin Film Insulators," American Vacuum Society Pacific Northwest Symposium, Troutdale, Ore., Sept. 16–20, 1996.

M. V. Gorshkov, J. A. Mack, S. E. Barlow, D. Ray, and J. M. Price, "Frequency-Sweep Radiofrequency Ion Trap Mass Spectrometry," 44th Annual American Society for Mass Spectrometry Conference, Portland, Ore., May 12–16, 1996.

W. P. Hess, "Laser Desorption of NO and CO from Sodium Nitrate and Calcium Carbonate Crystals," Workshop on X-Ray Techniques in the Environment, Richland, Wash., Sept. 8–12, 1996.

W. P. Hess, "Laser Ablation/Ionization Characterization of Solids," SERDP Symposium, Tysons Corner, Va., Nov. 20–22, 1996.

W. P. Hess, K. A. German, R. A. Bradley, and M. I. McCarthy, "Molecular Desorption from Ionic Molecular Crystals Following Resonant UV Excitation," 211th American Chemical Society National Meeting, New Orleans, March 24–28, 1996.

W. P. Hess, K. A. H. German, R. A. Bradley, D. P. Taylor, and K. M. Beck, "Laser Desorption of NO and CO from Sodium Nitrate and Calcium Carbonate Crystals," 1996 IEEE/LEOS Summer Topical Meeting, Keystone, Col., Aug. 5–9, 1996.

M. J. Iedema, H. Wong, J. P. Cowin, J. Biesecker, and G. B. Ellison, "Aqueous-Like Studies via Low-Energy Deposition on Surfaces," American Vacuum Society Pacific Northwest Symposium, Troutdale, Ore., Sept. 16–20, 1996.

S. A. Joyce, "Scanning Tunneling Microscopy of Ultrathin Film Insulators," University of Washington, Seattle, March 1, 1996.

S. A. Joyce, "Structural Studies of Thin Film Oxide Surfaces by STM and LEED," University of Kansas, Lawrence, Sept. 30, 1996.

B. D. Kay, "Adsorption, Desorption, Phase Transformation and Diffusion Kinetics in Nanoscale Ice Films," Physical Chemistry Seminar, University of Wisconsin, Madison, April 9, 1996.

B. D. Kay, "Adsorption, Desorption, Phase Transformation and Diffusion Kinetics in Nanoscale Ice Films," Physical Chemistry Seminar, University of Texas, Austin, April 11, 1996.

B. D. Kay, "Adsorption, Desorption, Phase Transformation and Diffusion Kinetics in Nanoscale Ice Films," Physical Chemistry Seminar, University of California at San Diego, La Jolla, April 22, 1996.

B. D. Kay, "Adsorption, Desorption, Phase Transformation and Diffusion Kinetics in Nanoscale Ice Films," Physical Chemistry Seminar, University of California at Irvine, April 23, 1996.

B. D. Kay, "Molecular Beam Studies of Kinetic Processes in Nanoscale Ice Films," Hong Kong Workshop on Surface Science: Critical Review and Outlook, Hong Kong, June 10–14, 1996.

B. D. Kay, Overview of Recent Advances in Gas–Surface Dynamics," Gordon Research Conference on Atomic and Molecular Interactions, New London, N.H., July 1–5, 1996.

B. D. Kay, "Molecular Beam Studies of Kinetic Processes in Nanoscale Ice Films," FOM Institute for Atomic and Molecular Physics, Amsterdam, Netherlands, Sept. 2, 1996.

B. D. Kay, "Molecular Beam Studies of Kinetic Processes in Nanoscale Ice Films," Geophysics Directorate Seminar, United States Air Force Phillips Laboratory, Hanscom Air Force Base, Mass., Oct. 10, 1996.

B. D. Kay, "Molecular Beam Studies of Kinetic Processes in Nanoscale Ice Films," Physical Chemistry Seminar, Brown University, Providence, R.I., Oct. 11, 1996.

B. D. Kay and K. R. Lykke, "Molecular Beam Studies of Atomic Hydrogen with Clean and Adsorbate-Covered Surfaces," Hyperthermal Energy Molecule–Surface Reactions Symposium, American Chemical Society 212th National Meeting, Orlando, Fla., Aug. 25–29, 1996.

J. Kelly, B. Cannon, S. Sharpe, and R. McDowell, "FM Laser Techniques and Technology Developments," Third Annual Interim Technical Review, CALIOPE Program (Chemical Analysis by Laser Interrogation of Proliferant Effluents), Sandia National Laboratory, Livermore, Cal., Feb. 13–15, 1996.

G. A. Kimmel, "A REMPI Study of Low-Energy (5–120 eV) Electron-Stimulated Interactions in Amorphous D_2O Ice," 42nd National Symposium,

American Vacuum Society, Minneapolis, Oct. 16–20, 1996.

G. A. Kimmel and T. M. Orlando, "Quantum Resolved Studies of Low-Energy (5–150 eV) Electron-Stimulated Interfacial Reactions," 44th Annual Meeting, Radiation Research Society, Chicago, April 16, 1996.

G. A. Kimmel and T. M. Orlando, "The Role of Dissociative Electron Attachment Resonances in Low-Energy Electron-Stimulated Production of Molecular Hydrogen from Amorphous D_2O Ice," 1996 International Symposium on the Physics and Chemistry of Ice, Hanover, N.H., Aug. 26–30, 1996.

N. Kizhakevariam, J. P. Cowin, S. A. Joyce, and X. L. Zhou, "Chemical Reactivity of Alkaline Earth Oxide Thin Films," 211th American Chemical Society National Meeting, New Orleans, March 24–28, 1996.

K. Knutsen and T. M. Orlando, "The Role of $NaNO_3$ Interfacial Radiolysis in the Production of Tank Waste Gases," 211th American Chemical Society National Meeting, New Orleans, March 24–28, 1996.

K. Knutsen and T. M. Orlando, "Photon- and Electron-Stimulated Desorption of $O(^3P_J)$ and NO ($^2\Pi$) from $NaNO_3$ Single Crystals," American Vacuum Society Pacific Northwest Symposium, Troutdale, Ore., Sept. 16–20, 1996.

K. Knutsen, Y. Su, K. D. Keefer, and T. M. Orlando, "Mechanisms of Radiolytic Decomposition of Complex Nuclear Waste Forms," American Nuclear Society Spectrum '96, Seattle, Aug. 18–23, 1996.

H. P. Lu and X. S. Xie, "Far-Field Scanning Optical Microscopy Studies on Spectroscopy and Dynamics of Single Molecules at Room Temperature," 43rd Annual Western Spectroscopy Association Conference, Asilomar, Cal., Jan. 31 – Feb. 5, 1996.

H. P. Lu and X. S. Xie, "Dynamics of Single Molecules at Room Temperature," Laser Applications to Chemical and Environmental Analysis (Optical Society of America), Orlando, Fla., March 18–22, 1996.

H. P. Lu and X. S. Xie, "Dynamics of Single Molecules at Room Temperature," 211th American Chemical Society National Meeting, New Orleans, March 24–28, 1996.

H. P. Lu and X. S. Xie, "Near-Field and Far-Field Single Molecule Spectroscopy at Room Temperature," Conference on Lasers and Electro-Optics (CLEO/QELS '96), Los Angeles, June 2–7, 1996.

H. P. Lu and X. S. Xie, "Room-Temperature Studies on Single-Molecule Spectroscopy and Chemical Dynamics," Gordon Research Conference on Atomic and Molecular Interactions, Plymouth, N.H., June 30 – July 5, 1996.

R. S. McDowell, "Overview of CALIOPE Research at Pacific Northwest National Laboratory," Third Annual Interim Technical Review, CALIOPE Program (Chemical Analysis by Laser Interrogation of Proliferant Effluents), Sandia National Laboratory, Livermore, Cal., Feb. 13–15, 1996.

M. B. More, E. Glendening, S. Hill, D. Ray, D. Feller, and P. B. Armentrout, "Cation–Ether Complexes in the Gas Phase: Bond Dissociation Energies and Equilibrium Structures," 44th Annual American Society for Mass Spectrometry Conference, Portland, Ore., May 12–16, 1996.

L. Novotny, "Theory of Near-Field Optical Spectroscopic Scanning Probes," Workshop on Optical Properties of Mesoscopic Semiconductor Structures, Snowbird, Utah, May 7–10, 1996.

T. M. Orlando, "Electron- and Photon-Stimulated Interactions in Amorphous D_2O Ice: Neutral Desorption Thresholds, Yields, and Velocity Distributions," 211th American Chemical Society National Meeting, New Orleans, March 24–28, 1996.

T. M. Orlando, "Quantum Resolved Studies of Low-Energy (5–150 eV) Electron-Stimulated Interfacial Reactions," Argonne National Laboratory, Argonne, Ill., April 17, 1996.

T. M. Orlando, "The Role of $NaNO_3$ Interfacial Radiolysis in the Production of Tank Waste Gases," NSF/REU Program on Science, Ethics, and the Environment, Los Angeles, July 16–17, 1996.

T. M. Orlando, "Photon- and Electron-Stimulated Desorption from Surfaces," Gaseous Electronics Conference, Chicago, Oct. 20–24, 1996.

T. M. Orlando and G. A Kimmel, "State-Resolved Studies of Low-Energy (5–50 eV) Electron- and Vacuum Ultraviolet Photon-Stimulated Reactions in Amorphous Ice," American Chemical Society 212th National Meeting, Orlando, Fla., Aug. 25–29, 1996.

T. M. Orlando, R. G. Tonkyn, S. E. Barlow, and W. O. Heath, "Probing Material Effects in Dielectric Barrier/Packed-Bed Corona Reactors," 3rd Conference on Advanced Oxidation Technologies, Cincinnati, Oct. 26–29, 1996.

N. G. Petrick, W. C. Simpson, and T. M. Orlando, "Laser-Stimulated and Cathodoluminescence Studies of ZrO_2(100) and (110) Single Crystals," American Vacuum Society Pacific Northwest Symposium, Troutdale, Ore., Sept. 16–20, 1996.

A. J. Peurrung and S. E. Barlow, "Characteristics of a Weakly Ionized Non-Neutral Plasma," 38th Annual Meeting of the Division of Plasma Physics, Denver, Nov. 1996.

D. Ray, "Transport of Molecules across the Liquid Water–Vapor Interface Probed by Surface Nonlinear Optical Spectroscopy," Colorado State University, Fort Collins, March 14, 1996.

D. Ray, "Transport of Molecules across the Liquid Water–Vapor Interface Probed by Surface Nonlinear Optical Spectroscopy," University of Colorado, Boulder, March 15, 1996.

D. Ray, "Rotational Coherence Spectroscopy of Clusters," University of Colorado, Boulder, March 18, 1996.

D. Ray, "Transport of Molecules across the Liquid Water–Vapor Interface Probed by Surface Nonlinear Optical Spectroscopy," 211th American Chemical Society National Meeting, New Orleans, March 24–28, 1996.

D. Ray, "Transport of Molecules across the Liquid Water–Vapor Interface Probed by Surface Nonlinear Optical Spectroscopy," University of Washington, Seattle, April 3, 1996.

D. Ray, M. B. More, P. B. Armentrout, E. D. Glendening, and D. Feller, "Bond Dissociation Energies and Equilibrium Structures of Alkali Metal Cation–Ether Complexes in the Gas Phase," 8th Sanibel Conference on Mass Spectrometry: Metal-Containing Ions and their Applications in Mass Spectrometry, Sanibel, Fla., Jan. 20–23, 1996.

E. Sanchez, L. Mets, and X. S. Xie, "Near-Field Fluorescence Microscopy and Spectroscopy of Photosynthetic Membranes," Western Spectroscopy Association 43rd Annual Conference, Asilomar, Cal., Jan. 31 – Feb. 2, 1996.

E. Sanchez, L. Mets, and X. S. Xie, "Near-Field Fluorescence Microscopy and Spectroscopy of Photosynthetic Membranes," Biophysical Society 40th Annual Meeting, Baltimore, Md., Feb. 17–21, 1996.

S. W. Sharpe, R. S. McDowell, and T. A. Blake, "Simplification of FTIR Spectra by Rotational Cooling of Molecules Entrained in a Supersonic Molecular Beam Expansion," 38th Rocky Mountain Conference on Analytical Chemistry, Denver, July 21–26, 1996.

S. Sharpe, R. McDowell, and J. Kelly, "Continuing Spectroscopic Efforts for CALIOPE" (Poster), Third Annual Interim Technical Review, CALIOPE Program (Chemical Analysis by Laser Interrogation of Proliferant Effluents), Sandia National Laboratory, Livermore, Cal., Feb. 13–15, 1996.

S. W. Sharpe, R. L. Sams, K. D. Thrall, and J. J. Toth, "Applications of Near-Infrared Spectroscopy to Breath Analysis: Potential Use in the Diagnosis of Disease," 38th Rocky Mountain Conference on Analytical Chemistry, Denver, July 21–26, 1996.

S. W. Sharpe, S. Xu, R. S. McDowell, and T. A. Blake, "Tunable Diode Lasers and Their Application in Cold Molecular Beam Spectroscopy," Application of Tunable Diode and Other Infrared Sources for Atmospheric Studies and Industrial Process Monitoring, SPIE Annual Meeting, Denver, Aug. 7–9, 1996.

M. T. Sieger, G. A. Kimmel, and T. M. Orlando, "Low-Energy (5–100 eV) Electron-Stimulated Interactions in Ice Films: Temperature-Dependent Proton Yields and Observation of Negative Ion Resonances," Gordon Research Conference on Interaction of Water with Surfaces, Plymouth, N.H., July 28 – Aug. 2, 1996.

M. T. Sieger and T. M. Orlando, "Electron-Stimulated Desorption of D^+ from Vapor-Deposited D_2O Ice Surfaces: Temperature Dependence of the Yield," American Vacuum Society Pacific Northwest Symposium, Troutdale, Ore., Sept. 16–20, 1996.

W. C. Simpson, G. A. Kimmel, M. T. Sieger, and T. M. Orlando, "Temperature, Thickness, and Morphology Dependence of Dissociative Electron Attachment in Condensed Water Films," Ameri-

can Vacuum Society Pacific Northwest Symposium, Troutdale, Ore., Sept. 16–20, 1996.

R. S. Smith, C. Huang, and B. D. Kay, "Molecular Beam Studies of Kinetic Processes in Nanoscale Ice Films," 3rd European Conference on Gas-Surface Dynamics and 2nd European Conference on Lasers in Surface Science, Kerkrade, Netherlands, Sept. 3–6, 1996.

R. S. Smith, C. Huang, M. J. Stirniman, E. K. L. Wong, and B. D. Kay, "Molecular Beam Studies of Adsorption, Desorption, and Diffusion Kinetics in Nanoscale Ice Films," Environmental Heterogeneous Processes Symposium, 211th American Chemical Society National Meeting, New Orleans, March 24–28, 1996.

R. S. Smith, C. Huang, E. K. L. Wong, and B. D. Kay, "Adsorption, Desorption, Phase Transformation, and Diffusion Kinetics in Nanoscale Ice Films," Gordon Research Conference on Atomic and Molecular Interactions, New London, N.H., July 1–5, 1996.

R. S. Smith, C. Huang, E. K. L. Wong, and B. D. Kay, "Adsorption, Desorption, Phase Transformation, and Diffusion Kinetics in Nanoscale Ice Films," Gordon Research Conference on Interaction of Water with Surfaces, Plymouth, N.H., July 28 – Aug. 2, 1996.

R. S. Smith, C. Huang, E. K. L. Wong, and B. D. Kay, "Adsorption, Desorption, Phase Transformation, and Diffusion Kinetics in Nanoscale Ice Films," Gordon Research Conference on Water and Aqueous Solutions, Plymouth, N.H., Aug. 4–9, 1996.

R. S. Smith, C. Huang, E. K. L. Wong, and B. D. Kay, "Adsorption, Desorption, Phase Transformation, and Diffusion Kinetics in Nanoscale Ice Films," 1996 International Symposium on the Physics and Chemistry of Ice, Hanover, N.H., Aug. 26–30, 1996.

R. S. Smith, C. Huang, E. K. L. Wong, and B. D. Kay, "Adsorption, Desorption, Phase Transformation, and Diffusion Kinetics in Nanoscale Ice Films," American Vacuum Society Pacific Northwest Symposium, Troutdale, Ore., Sept. 16–20, 1996.

M. J. Stirniman, C. Huang, R. S. Smith, S. A. Joyce, and B. D. Kay, "Water Adsorption and Desorption Kinetics on Single-Crystal and Thin-Film MgO(100) Surfaces," Environmental Heterogeneous Processes Symposium, 211th American Chemical Society National Meeting, New Orleans, March 24–28, 1996.

M. A. Tinkle and S. E. Barlow, "Physics of ICR Mass Spectrometers," 38th Annual Meeting of the Division of Plasma Physics, Denver, Nov. 1996.

R. G. Tonkyn, S. E. Barlow, and T. M. Orlando, "Destruction of Carbon Tetrachloride and Trichloroethylene in a Packed-Bed Corona Reactor," Gordon Research Conference on Plasma Processing Science, New Hampton, N.H., Aug. 1996.

V. A. Venturo, A. G. Joly, J. M. Price, and D. Ray, "Rotational Coherence Spectroscopy of Mass-Selected Ionic Clusters," 211th American Chemical Society National Meeting, New Orleans, March 24–28, 1996.

L.-S. Wang, "Probing the Electronic Structure of Transition Metal Clusters by Size-Selected Anion Photoelectron Spectroscopy," Research Center of Disorder on Mesoscopic Scales, University of Marburg, Germany, March 18, 1996.

L.-S. Wang, "Cluster Models Studies of the Structure and Bonding of Environmentally Important Materials," Research Center of Disorder on Mesoscopic Scales, University of Marburg, Germany, March 18, 1996.

L.-S. Wang, "Photoelectron Spectroscopy of Transition Metal Clusters," American Physical Society, St. Louis, March 18–22, 1996.

L.-S. Wang, "Oxide Clusters Studied by Anion Photoelectron Spectroscopy," American Physical Society, St. Louis, March 18–22, 1996.

L.-S. Wang, "Studies of Silicon Oxide Clusters: Models for Oxidation of Silicon Surfaces and Defect Sites in Bulk Silicon Oxides," Eighth International Symposium on Small Particles and Inorganic Clusters, Copenhagen, July 1–6, 1996.

L.-S. Wang, "Evolution of the Electronic Structures of Transition Metal Clusters by Photoelectron Spectroscopy," Eighth International Symposium on Small Particles and Inorganic Clusters, Copenhagen, July 1–6, 1996.

L.-S. Wang, "Probing the Electronic Structure Evolution of Transition Metal Clusters from Atoms to Bulk," Second International Symposium on Theory of Atomic and Molecular Clusters, Fontana, Wis., Sept. 15–20, 1996.

L.-S. Wang, "Photoelectron Spectroscopy of Silicon Oxide Clusters," Department of Chemistry, Virginia Commonwealth University, Richmond, Va., Sept. 23, 1996.

L.-S. Wang, "Probing the Electronic Structure of Transition Metal Clusters: V_n, Ni_n, Co_n, and Fe_n," Department of Physics, University of Virginia, Charlottesville, Sept. 24, 1996.

L.-S. Wang, "Probing the Electronic Structure of Transition Metal Clusters: Molecular to Bulk Transition," Department of Chemistry, University of Maryland, College Park, Sept. 25, 1996.

L.-S. Wang, "Electronic Structure of Transition Metal Clusters: Photoelectron Studies," Department of Chemistry, Johns Hopkins University, Baltimore, Sept. 26, 1996.

L.-S. Wang, "Cluster Model Studies of Environmentally Important Oxide Materials," Air Products and Chemicals, Inc., Allentown, Pa., Sept. 27, 1996.

L.-S. Wang, "Chromium Clusters: Dimer Growth and Electronic Structure Evolution," Department of Chemistry, Lehigh University, Bethlehem, Pa., Sept. 27, 1996.

L.-S. Wang, "Cluster Model Studies of Environmentally Important Oxide Materials," Department of Chemistry, Oregon State University, Corvallis, Oct. 23, 1996.

L.-S. Wang, "Small Silicon Oxide Clusters: Models for Oxidation of Silicon Surfaces and Defect Sites for Bulk Oxide Materials," Department of Physics, Washington State University, Pullman, Nov. 12, 1996.

Z. Wang, A. G. Joly, D. M. Friedrich, C. C. Ainsworth, and P. L. Gassman, "Probing Metal Ion Complexation with Salicylic Acid and Its Derivatives with Excited-State Proton Transfer and Luminescence Anisotropy," Environmental Heterogeneous Interfaces Symposium, 211th American Chemical Society National Meeting, New Orleans, March 24–28, 1996.

X. S. Xie, "Near-Field Fluorescence Microscopy and Spectroscopy of Photosynthetic Membranes," 40th Annual Meeting, Biophysical Society, Baltimore, Md., Feb. 17–22, 1996.

X. S. Xie, "Single-Molecule Spectroscopy at Interfaces," 211th American Chemical Society National Meeting, New Orleans, March 24–28, 1996.

X. S. Xie, "Single-Molecule Spectroscopy at Interfaces," University of California, Los Angeles, April 1, 1996.

X. S. Xie, "Single Molecule Spectroscopy and Chemical Dynamics," Department of Chemistry, California Institute of Technology, Pasadena, April 2, 1996.

X. S. Xie, "Single Molecule Spectroscopy and Dynamics at Room Temperature," Royal Microscopical Society Meeting: 3D Imaging Sciences in Microscopy, Oxford University, England, April 14–17, 1996.

X. S. Xie, "Single Molecule Spectroscopy and Chemical Dynamics at Room Temperature," 51st Ohio State University International Symposium on Molecular Spectroscopy, Columbus, June 8–14, 1996 (Coblentz Award address).

X. S. Xie, "Near-Field Single Molecule Spectroscopy," International Workshop on Photons and Local Probes III, Stuttgart, Germany, July 15–18, 1996.

X. S. Xie, "Single Molecule Spectroscopy at Room Temperature," Gordon Research Conference on Electronic Processes in Organic Materials, Proctor Academy, Andover, N.H., July 21–26, 1996.

X. S. Xie, "Biological Applications of Single-Molecule Spectroscopy," Molecular Biotechnology Symposium, American Chemical Society 212th National Meeting, Orlando, Fla., Aug. 25–29, 1996.

X. S. Xie, "Imaging, Spectroscopy, and Dynamics of Single Molecules, Single Proteins, and Biological Membranes," Department of Chemistry, University of Washington, Seattle, Oct. 9, 1996.

X. S. Xie, "Near-Field Microscopy and Spectroscopy of Single Molecules, Single Proteins, and Biological Membranes," Optical Society of America Annual Meeting/ILS XII, Optics and Imaging in the Information Age, Rochester, N.Y., Oct. 20–24, 1996.

X. S. Xie, "Single-Molecule Spectroscopy and Chemical Dynamics," National Institutes of Health, Bethesda, Md., Nov. 20, 1996.

X. S. Xie, "Near-Field and Far-Field Spectroscopy of Biological Systems," 35th Eastern Ana-

lytical Symposium, Murray Hill, N.J., Nov. 21–23, 1996.

X. S. Xie, "Imaging, Spectroscopy, and Dynamics of Single Molecules, Single Proteins, and Biological Membranes," Department of Chemistry, University of Pennsylvania, Philadelphia, Nov. 22, 1996.

X. S. Xie, H. P. Lu, X. Bian, and P. Leung, "Single-Molecule Spectroscopy and Dynamics at Room Temperature," '96 Spectral Hole Burning and Related Spectroscopies: Science and Applications, Brainerd, Minn., Sept. 13-17, 1996.

Awards and Recognition

Cindy Irwin was appointed to Senior Administrative Secretary, January 1996.

Steve Joyce served as vice-chair of the Pacific Northwest Section, American Vacuum Society, and will assume the chair in January 1997.

Lukas Novotny was awarded the 1996 Swiss Federal Institute of Technology (ETH) Medal for his thesis on "Light Propagation and Light Confinement in Near-Field Optics."

Thom Orlando was promoted to Chief Scientist IV, July 1996.

Scott Smith was promoted to Research Scientist III, January 1996.

Russ Tonkyn was promoted to Research Scientist III, January 1996.

Lai-Sheng Wang received a CAREER program award in 1996 from the National Science Foundation. The NSF CAREER program (Faculty Early Career Development Program) replaces the former NSF Young Investigator Awards program, and supports junior faculty for quality research and education. Lai-Sheng was recognized for his research project on "Study of Transition Metal–Carbon Mixed Clusters: From Gas Phase to Condensed Phase," and for his teaching at Washington State University at Tri-Cities.

Sunney Xie was the 1996 winner of the Coblentz Award, presented annually since 1964 to an outstanding spectroscopist under the age of 36 by The Coblentz Society, a professional organization that fosters the understanding and application of vibrational spectroscopy in the academic and industrial communities. Sunney was named for his work in near-field fluorescence spectroscopy on individual molecules in their natural biochemical environment. He received the award at the 51st Ohio State University International Symposium on Molecular Spectroscopy, June 10–14, 1996, giving an address entitled, "Single-Molecule Spectroscopy and Chemical Dynamics at Room Temperature."

Collaborations

External Collaborations

J. P. Cowin
University of Colorado (G. B. Ellison)
Molecular Dynamics at Water/Solid Interfaces

J. P. Cowin
University of Washington (E. Struve)
Hydronium in Ice Films

W. P. Hess
Vanderbilt University (R. F. Haglund, Jr.)
Studies of Laser/Solids Interactions

W. P. Hess
University of Colorado (G. B. Ellison)
Photochemistry of Thin Molecular Films

W. P. Hess
Washington State University (J. T. Dickinson, R. Webb, and K. A. Peterson)
Laser Ablation Characterization of Solids

S. A. Joyce
Lakehead University, Thunder Bay, Ont. (M. C. Gallagher)
Oxidation of NiAl Alloys

S. A. Joyce
Tulane University (U. Diebold)
Structure and Chemistry of Metal Oxides

B. D. Kay
Chalmers University, Göteborg, Sweden (B. Kasemo)
Desorption and Phase Transformation Kinetics in Amorphous Ice

B. D. Kay
University of Colorado (S. M. George)
Optical Properties and Porosity of Vapor Deposited Ice Films

B. D. Kay
University of Wellington, N.Z. (R. J. Speedy) and Princeton University (P. G. Debenedetti)
Metastability of Glassy Water and its Relation to Liquid Water

R. S. McDowell and S. W. Sharpe
Los Alamos National Laboratory (B. J. Krohn)
Rovibrational Analysis of High-Symmetry Molecules

T. M. Orlando
University of Illinois (L. Hanley)
Laser Ablation Mass Spectrometry

T. M. Orlando
Argonne National Laboratory (D. Meisel)
Radiation Chemistry

T. M. Orlando
Lawrence Livermore National Laboratory (J. N. Bardsley and B. M. Penetrante)
Development of Plasma Processing Techniques

T. M. Orlando
University of Sherbrooke (L. Sanche)
Low-Energy Electron-Stimulated Processes in Water Overlayers

D. Ray
University of Utah (P. B. Armentrout)
Gas-Phase Cation–Ether Complexes

S. W. Sharpe
National Institute for Standards and Technology (G. T. Fraser, W. J. Lafferty, and A. S. Pine)
Rovibrational Spectral Analysis of Molecules and Molecular Clusters

S. W. Sharpe
Oregon State University (J. W. Nibler)
Jet Spectroscopy of Metal Borohydrides

S. W. Sharpe
State University of New York at Stony Brook (P. Varanasi)
High-Resolution Infrared Spectroscopy of Atmospheric Interest

S. W. Sharpe
California Air Resource Board (P. Rieger)
Reactivity Meter for Automotive Emissions Analysis

S. W. Sharpe
Wesleyan University (S. E. Novick)
High-Resolution Spectroscopy of Hydrogen-Bonded Dimers

R. G. Tonkyn
Delphi Energy and Engine Management Systems, Flint, Mich. (D. Goulette)
Vehicle Exhaust Treatment

L. S. Wang
Air Products and Chemicals, Inc., Allentown, Pa. (H. S. Chen)
Theoretical Studies of Atomic Clusters

L. S. Wang
Sandia National Laboratory, Livermore, Cal. (C. M. Rohlfing)
Theoretical Study of Small Aluminum Oxide Clusters

L. S. Wang
Rice University (L. Lou)
Density Functional Theory Study of Metal Clusters

L. S. Wang
Washington State University (C.-F. Ding)
Study of Solvated Clusters

L. S. Wang
Washington State University (S. Li)
Photoelectron Spectroscopy of Met-Cars

L. S. Wang
Washington State University (H. Wu)
Electronic Structure of Transition-Metal Clusters

X. S. Xie
WSU Tri-Cities (L. Xun)
Single Protein Enzymatic Reactions of Dehalogenase

Collaborations within PNNL

S. E. Barlow
EHSD Materials and Chemical Sciences Department, Nuclear Chemistry Section (A. J. Peurrung)
Stabilization of Nonneutral Plasmas

S. D. Colson
Staff throughout PNNL (L. G. Morgan, J. Janata, J. G. Hill, M. S. Hanson, and R. E. Gephart)
Hanford Tank Characterization and Safety Issue Resolution Project

S. D. Colson and R. S. McDowell
Energy Division, Engineering and Analytical Sciences Department, Sensors and Measurement Systems Section (J. S. Hartman); and EHSD Materials and Chemical Sciences Department, Atomic and Molecular Chemistry Section (M. L. Alexander)
Waste Tank Speciation Methods

W. P. Hess
EHSD Materials and Chemical Sciences Department, Atomic and Molecular Chemistry Section (J. A. Campbell)
Laser Ablation Characterization of Solids

W. P. Hess
EMSL Theory, Modeling, and Simulation (M. I. McCarthy, S. S. Xantheas, and J. D. Myers)
Studies of Laser/Solid Interactions

S. A. Joyce
EMSL Interfacial and Processing Science (B. C. Bunker)
Physics and Chemistry of Ceramic Surfaces

S. A. Joyce
EMSL Interfacial and Processing Science (M. A. Henderson); and EHSD Earth Systems Sciences Department, Thermodynamic and Molecular Geochemistry Group (J. R. Rustad)
Surface Chemistry of Iron Oxides

B. D. Kay
EMSL Interfacial and Processing Science (B. C. Bunker)
Physics and Chemistry of Ceramic Surfaces

T. M. Orlando
EHSD Materials and Chemical Sciences Department, Atomic and Molecular Chemistry Section (D. M. Camaioni)
Tank Waste Chemistry

T. M. Orlando
Environmental Technology Division, Process Technology Department, Electrical and Chemical Processes Group (W. O. Heath and T. M. Bergsman)
Low-Temperature Plasma Destruction Techniques

T. M. Orlando and W. Hess
EMSL Interfacial and Processing Science (K. D. Keefer)
Radiation Damage of Waste Forms

D. Ray
EMSL Computing and Information Sciences (J. M. Price)
Spectroscopy and Dynamics of Molecular Clusters

D. Ray
EMSL Theory, Modeling, and Simulation (D. F. Feller)
Gas-Phase Cation–Ether Complexes

S. W. Sharpe
National Security Division (R. G. Clemmer and S. W. Martin)
Standoff Infrared Sensors for Detection of Clandestine Methamphetamine Production

S. W. Sharpe
Energy Division, Engineering and Analytical Sciences Department, Sensors and Measurement Systems Section (J. S. Hartman)
Development of Infrared Sniffer System

S. W. Sharpe
Energy Division, Engineering and Analytical Sciences Department, Sensors and Measurement Systems Section (J. W. Griffin)
Infrared Analysis in Head-Space Sampling for Paper and Pulp Digesters

S. W. Sharpe
Energy Division, Engineering and Analytical Sciences Department, Sensors and Measurement Systems Section (J. S. Hartman and M. A. Khaleel)
Sensors and Modeling for Auto Glass Production

S. W. Sharpe and R. S. McDowell
Energy Division, Engineering and Analytical Sciences Department, Sensors and Measurement Systems Group (J. F. Kelly)
Spectroscopic Techniques for Atmospheric Monitoring

R. G. Tonkyn
Environmental Technology Division, Process Technology Department (W. O. Heath)
C_2F_6 Destruction in a Packed-Bed Corona Reactor

L. S. Wang and S. D. Colson
EMSL Theory, Modeling, and Simulation (J. B. Nicholas)
Cluster Model Studies of Environmentally-Important Oxide Clusters

X. S. Xie
Earth Systems Sciences Department, Atmospheric Sciences section (R. X. Bian)
Near-Field Optical Tweezers Manipulation of Enzymatic Reactions on Biological Membranes.

Acronyms and Abbreviations

2D	two-dimensional
AES	Auger electron spectrometer
ANL	Argonne National Laboratory
ASMS	American Society for Mass Spectrometry
ASW	amorphous solid water
AWU	Associated Western Universities
BET	Brunauer-Emmett-Teller
BSK	Beam Surface Kinetics instrument
CALIOPE	Chemical Analysis by Laser Interrogation of Proliferant Effluents
CCD	charge-coupled device
CID	collision-induced dissociation
CL	cathodoluminescence
CRADA	Cooperative Research and Development Agreement
CS&D	Chemical Structure and Dynamics
DC	direct current
DEA	dissociative electron attachment
DHB	2,5-dihydroxybenzoic acid
DMSO	dimethyl sulfoxide
DOE	Department of Energy
EA	electron affinity
EDTA	ethylenediaminetetraacetic acid
EHSD	Environmental and Health Sciences Division
EMSL	William R. Wiley Environmental Molecular Sciences Laboratory
EMSP	DOE Environmental Management Science Program
ESD	electron-stimulated desorption/dissociation
FAB	fast atom bombardment
FACSS	Federation of Analytical Chemistry and Spectroscopy Societies
FAD	flavin adenine dinucleotide
FDA	Food and Drug Administration
FM	frequency modulation/modulated
FMN	flavin mononucleotide
FTIR	Fourier-transform infrared
FTIRS	Fourier-transform infrared spectrometer
FTMS	Fourier-transform mass spectrometry
fwhm	full width at half-maximum
HEDTA	N-(2-hydroxyethyl) ethylenediaminetriacetic acid
HMW	high molecular weight
HOMO	highest occupied molecular orbital
ICR	ion cyclotron resonance
ICS	Instrumentation for Clusters and Surfaces instruments
IEEE	Institute of Electrical and Electronics Engineers
IR	infrared
ITO	indium tin oxide
LAMS	laser ablation mass spectrometry
LDRD	Laboratory Directed Research and Development
LEED	low-energy electron diffraction
LMW	low molecular weight
LSL	laser-stimulated luminescence
LUMO	lowest unoccupied molecular orbital
MALDI	matrix-assisted laser desorption/ionization
met-car	metallo-carbohedrene
MGR	Menzel-Gomer-Redhead
ML	monolayer(s)
MMP	multiple multipole method
MS	mass spectrometer/spectrometry
NASA	National Aeronautics and Space Administration
NIR	near infrared
NRC	National Research Council
NSF	National Science Foundation
NTA	nitrilotriacetic acid
PES	photoelectron spectroscopy
PHF	periodic Hartree-Fock
PMMA	polymethyl methacrylate
PNL	Pacific Northwest Laboratory (to Sept. 1995)
PNNL	Pacific Northwest National Laboratory (from Oct. 1995)
PSD	photon-stimulated desorption/degradation
QMS	quadrupole mass spectrometer
RCS	rotational coherence spectroscopy
REMPI	resonance-enhanced multiphoton ionization
RF	radio-frequency
RRKM	Rice-Ramsberger-Kossel-Marcus
SABIT	Special American Business Internship Training Program for Business Executives and Scientists from the Independent States of the Former Soviet Union
SAE	Society of Automotive Engineers
SERDP	Strategic Environmental Research and Development Program
SERS	Science and Engineering Research Semester
sf	surface
SIMS	secondary ion mass spectrometer
SPIE	Society of Photo-Optical Instrumentation Engineers
STM	scanning tunneling microscopy

TOF	time of flight	UV	ultraviolet
TPD	temperature-programmed desorption	VFT	Vogel-Fulcher-Tamann
UHV	ultrahigh vacuum	WSU	Washington State University
UPS	ultraviolet photoelectron spectroscopy	XPS	X-ray photoelectron spectroscopy
USCAR	U.S. Council for Automotive Research	YAG	yttrium aluminum garnet

Where CS&D Fits in PNNL

Pacific Northwest National Laboratory (W. J. Madia, *Director*)
- Energy Division (G. L. Work)
- **Environmental and Health Sciences Division (EHSD)** (M. L. Knotek)*
  - Earth Systems Sciences Department (*vacant*)
  - **Environmental Molecular Sciences Laboratory (EMSL)** (T. H. Dunning)
    - EMSL Construction Project (J. W. Bixler)
    - **Chemical Structure and Dynamics (CS&D)** (S. D. Colson)
    - Materials and Interfaces (M&I) (J. Janata)†
    - Macromolecular Structure and Dynamics (MS&D) (P. D. Ellis)
    - Theory, Modeling, and Simulation (TM&S) (D. A. Dixon)
    - Environmental Dynamics and Simulation (ED&S) (J. M. Zachara)
    - Computing and Information Sciences (C&IS) (R. A. Bair)
    - Processing Science (B. C. Bunker)†
  - Materials and Chemical Sciences Department (G. L. McVay)
  - Molecular Biosciences Department (J. D. Saffer)
- Environmental Technology Division (B. D. Shipp)
- National Security Division (T. R. Fox)
- Economic Development (J. T. A. Roberts)

*Effective Jan. 1997, (G. M. Stokes).
†Effective early 1997, to be combined into Interfacial and Processing Science (B. C. Bunker).